FINAL REPORT

Discovering Blind Geothermal Systems in the Great Basin Region: An Integrated Geologic and Geophysical Approach for Establishing Geothermal Play Fairways

Recipient: Board of Regents on behalf of the University of Nevada, Reno

Award Number: DE-EE0006731

Principal Investigator: James Faulds, Nevada Bureau of Mines and Geology, University of Nevada, Reno

Team Members:

- Nevada Bureau of Mines and Geology, University of Nevada, Reno (Drs. James Faulds-PI, Nick Hinz, Craig dePolo, William Hammond, and Corné Kreemer)
- ATLAS Geosciences, Inc. (Drs. Lisa Shevenell and Mark Coolbaugh)
- Hi-Q Geophysical, Inc. (Dr. John Queen)
- Lawrence Berkeley National Laboratory (Dr. Drew Siler)
- National Renewable Energy Laboratory (Dr. Charles Visser)
- University of Utah (Dr. Phil Wannamaker)

DOE Project Team: DOE Contracting Officer – Laura Merrick
DOE Project Officer – Holly Thomas
Project Monitor – N/A

McGinness Hills Geothermal Power Plant (72 MWe), Central Nevada:
A Recently Developed Blind Geothermal System

TABLE OF CONTENTS

Appendices

Note: Abbreviations for geothermal systems or areas in multiple figures in this report: Br, Bradys; Bw, Beowawe; DP, Desert Peak; DV, Dixie Valley; LA, Lee-Allen; MH, McGinness Hills; RV, Ruby Valley; SE, San Emidio; SL, Soda Lake; St, Stillwater; SW, Salt Wells; TM, Tungsten Mountain; WR, Wild Rose (Don Campbell).

EXECUTIVE SUMMARY

This project focused on defining geothermal play fairways and development of a detailed geothermal potential map of a large transect across the Great Basin region (96,000 km^2), with the primary objective of facilitating discovery of commercial-grade, blind geothermal fields (i.e. systems with no surface hot springs or fumaroles) and thereby accelerating geothermal development in this promising region. The Great Basin currently hosts ~24 geothermal power plants with more than 550 MW of capacity, but estimates suggest that the region may be capable of producing ~30,000 MW. Recent studies indicate that a combination of geological, geochemical, and geophysical features characterize the most robust geothermal systems. Considering that most of the geothermal resources in this region are blind, it is imperative that the favorable characteristics for geothermal activity be synthesized and techniques perfected for the discovery of new viable systems.

We therefore utilized a multi-disciplinary approach and synthesized ~10 geologic, geochemical, and geophysical parameters to produce new detailed geothermal fairway and favorability maps that can guide exploration efforts in identifying previously undiscovered geothermal systems. Our analysis included: 1) structural settings (i.e., patterns of faulting), 2) age of recent faulting, 3) slip rates on recent faults, 4) regional-scale strain rates, 5) the tendency of faults to slip or dilate based on their orientation in the regional stress field, 6) earthquake density, 7) gravity data, 8) electrical conductivity data (where available), 9) temperature at 3 km depth, and 10) geochemistry from springs and wells. These parameters were grouped into subsets to delineate rankings for local permeability, regional permeability, and heat, which collectively defined the geothermal play fairways (i.e., most likely locations for significant geothermal fluid flow). A major challenge was appropriate weighting of individual data types to best predict permeability and overall geothermal potential. Rigorous statistical methods, utilizing 34 benchmarks of known relatively high-temperature (>130^oC) geothermal systems within the region, were employed to determine the hierarchal weights of each parameter. Analyses of these parameters were also coupled with a thorough review of the degree of previous exploration, thus permitting identification of under-explored regions that are potentially ripe for development. Major deliverables from this project include: 1) digital databases for each geologic, geophysical, geochemical, and geodetic parameter; 2) detailed statistically-based geothermal potential maps (fairway and favorability maps) of a 400 x 240-km-wide transect across the Great Basin region of Nevada; and 3) identification of the most promising areas for future geothermal development based on analysis of the results from our predictive modeling. This project marks the first successful attempt to combine ~10 parameters into detailed geothermal potential maps for this region. To facilitate economic assessments for exploration and development, the final favorability map also includes layers showing land use status and critical infrastructure, such as electrical transmission and transportation corridors.

The new geothermal potential map will help to reduce the risks in prospecting for new geothermal systems throughout the region, which may stimulate a resurgence in green-field exploration and geothermal development. Additionally, because this geothermal map incorporates more parameters than previous efforts, it may serve as a prototype for producing detailed geothermal potential maps for the entire Great Basin, as well as other geothermal provinces throughout the world. Furthermore, 3D models produced for two large basins within the project area provide a template for producing even more detailed geothermal potential maps, further reducing the risks of exploration and development in particularly promising areas. A logical continuation of this project is a Phase II study focused on detailed analysis of several of the most promising areas identified on the detailed geothermal potential maps and selection of drilling targets at these sites. A successful Phase II would then progress to Phase III drilling of the best targets to confirm new geothermal resources and stimulate development of new geothermal power plants by industry. Ultimately, this study may facilitate development of the vast untapped geothermal resources in the Great Basin region and thus greatly enhance the contribution from geothermal to the nation's overall energy budget.

INTRODUCTION

Although significant progress has been made in characterizing favorable settings for geothermal activity, barriers remain that inhibit the ability to assess potential resources, prioritize sites, confidently identify geothermal play fairways, and minimize risk ahead of expensive drilling. Resolution of these barriers requires multi-disciplinary approaches that integrate multiple data sets and utilize geostatistical techniques. Major challenges include defining logical relative rankings of each geological, geochemical, and geophysical parameter and combining multiple data sets into a comprehensive geothermal potential/permeability map.

Due to its high geothermal gradient (Blackwell et al., 2010) and relatively high extensional to transtensional strain rates (Fig. I-1; Blewitt et al., 2003; Faulds et al., 2012), the Great Basin is one of the largest geothermal provinces on Earth, significantly larger than geothermal provinces in Iceland, New Zealand, and Turkey combined. With the exception of a few geothermal systems along its margins (e.g., Coso and Long Valley), geothermal systems in the Great Basin region are amagmatic and thus lack a mid to upper crustal magmatic heat source. Instead, regional tectonism has significantly thinned the crust and lithosphere and induced a high geothermal gradient throughout the Great Basin. Published estimates suggest that the region is capable of producing ~30,000 MW electricity (Williams et al., 2007, 2009). Some relationships imply that the geothermal potential of the region may exceed 30,000 MW (Faulds et al., 2010). However, nameplate capacity of existing power plants in the region is currently less than 600 MW.

Major factors that have inhibited more widespread geothermal development in the Great Basin include finding sufficient permeability and the blind nature of the bulk of the geothermal resources. Permeability is particularly difficult to predict and can vary significantly over distances of 100-200 m. Adequate permeability generally poses a far greater challenge than locating high temperatures in this region. Locating sufficient permeability is compounded by the blind nature of many geothermal systems. Similar to most hydrocarbon deposits, the bulk of geothermal resources in the Great Basin region are blind and lack surface expressions, such as hot springs and fumaroles. For example, ~39% of the known systems are blind (Faulds and Hinz, 2015; Fig. I-2), and estimates suggest that ~75% of all geothermal resources in the region are blind (Coolbaugh et al., 2007). Some blind systems in this region (e.g. Desert Peak and Stillwater) are high enthalpy and host geothermal power plants. Most of the known blind systems were discovered through regional gradient drilling programs (e.g., Desert Peak; Benoit et al., 1982) or by accident during the drilling of agricultural wells (e.g., Stillwater) or mineral exploration holes (e.g., McGinness Hills, Tungsten Mountain, Blue Mountain). Due primarily to these challenges, the Great Basin has yet to live up to its geothermal potential.

Considering the enormous, but minimally developed geothermal potential of this region and the probable extent of blind geothermal systems, it is imperative that exploration strategies, utilizing the most innovative technologies, be developed and tested to both identify the geological and geophysical signatures of known robust, high enthalpy systems and identify favorable geothermal play fairways as proxies for heretofore undiscovered blind systems. To date, the most detailed geothermal potential map of the Great Basin incorporated: 1) gravity gradient data, 2) dilational GPS strain rates, 3) upper-crustal temperature gradient, 4) frequency and magnitude of earthquakes, and 5) presence of Quaternary faults (Coolbaugh et al., 2005). Considering the abundance of blind geothermal resources and the significant advancements in recent years in understanding the structural, geophysical, and geochemical signatures of geothermal systems, it is timely to produce a more comprehensive geothermal potential map that can better serve the geothermal industry in identifying the most highly prospective areas for development and facilitate erosion of some of the technical barriers facing the industry.

Objectives and Approach

The primary objectives of this project were therefore aimed at developing a comprehensive play fairway analysis and detailed geothermal potential map to identify new prospects with high potential for hosting commercial-grade geothermal systems in the Great Basin region (Fig. I-2). Recent research indicates that geothermal upwellings in this region are typically focused in certain structural settings characterized by fault intersection/interaction areas, high fault density, and faults favorably oriented for slip and/dilation in the regional stress field (Faulds et al., 2006, 2011, 2013; Hinz et al., 2008, 2011, 2014b; Siler et al., 2013). Recent compilations further suggest that nearly 90% of the known geothermal systems in the region are hosted by only four major structural settings, namely horse-tailing fault terminations, step-overs or relay ramps, fault intersections, and accommodation zones (Fig. I-3). Such areas are also commonly characterized by other features, including Quaternary faults (Bell and Ramelli, 2007, 2009), gravity gradients, and resistivity anomalies (Wannamaker et al., 2013). These findings indicate that a combination of geologic and geophysical features can be used to identify the most promising areas for geothermal development, including blind systems with no surface hot springs or fumaroles as well as more conventional but undeveloped systems that have surface manifestations indicative of geothermal activity. Thus, the permeability problem is partially resolved, but existing geothermal potential maps do not adequately incorporate these recent findings into sophisticated rankings of geothermal play fairways.

This project was therefore focused on a multi-disciplinary geologic and geophysical analysis aimed at better defining geothermal play fairways and producing a detailed geothermal potential map across a large transect (400 km by 240 km) through the heart of the Great Basin geothermal province (Fig. I-2). We incorporated 10 major parameters into our analysis, including: 1) structural settings (Fig. I-3), 2) recency (i.e., age) of Quaternary faulting, 3) Quaternary fault slip rates, 4) regional geodetic strain rates, 5) slip and dilation tendency of Quaternary faults, 6) earthquake density, 7) gravity data, 8) MT data (where available), 9) temperature gradient data, and 10) geochemistry from springs and wells. These parameters were grouped into key subsets to define regional permeability, local permeability, and heat, which were then combined to define favorability for the fairway (Fig. I-4). Results were compared against a group of 34 benchmarks, representing 34 systems in the region with temperatures ≥130°C. We also coupled analyses of the main components of the fairway with a thorough review of the degree of previous exploration, thus permitting identification of under-explored green-field regions that are potentially ripe for development. This project focused on fault-controlled geothermal play fairways, because faults are the primary control for geothermal systems in the tectonically active Great Basin region (Curewitz and Karson, 1997; Blackwell et al., 1999; Richards and Blackwell, 2002; Faulds et al., 2006, 2010, 2011, 2013; Hinz et al., 2011, 2014b).

The study area is representative of the Great Basin, because it spans a progressive westward increase in strain from tenths of millimeters per year of crustal extension in the Basin and Range province of eastern Nevada to ~1 cm/yr of transtensional dextral motion in the Walker Lane belt of western Nevada and eastern California (Figs. I-1 and I-2). This belt of dextral shear accommodates ~20% of the right-lateral motion between the Pacific and North American plates (Hammond et al., 2009; Kreemer et al., 2012). The high geothermal potential of the western part of the study area has long been recognized, but this region likely contains many undiscovered blind systems, especially in large basins, such as the Carson Sink (Fig. I-2). Conversely, although both eastern and central Nevada have lower strain rates (Fig. I-1), they are probably underappreciated in terms of geothermal potential, as evidenced by robust high enthalpy systems at Beowawe and McGinness Hills (Fig. I-2).

Notably, McGinness Hills is a recently discovered blind system, with no surface hot springs or fumaroles, but now hosts two binary power plants that collectively produce 72 MWe (Nordquist and Delwiche, 2013). The recent discovery and successful development of McGinness Hills was a major motivation for this project, as it 1) epitomizes the enormous potential of this region, 2) demonstrates that relatively large geothermal systems can still be found and exist farther east than previous developments would suggest, and 3) shows that exploration for blind geothermal systems can provide substantial dividends. Many other undiscovered blind systems likely lie hidden beneath or along the margins of basins in central and eastern Nevada, as well as elsewhere in the Great Basin.

Considering that more than 50% of the Great Basin region consists of Neogene basins, with relatively thick basin fill obscuring underlying structural and stratigraphic relations that may favor geothermal activity, we incorporated 3D modeling of two representative basins on the western and eastern ends of the transect, the Carson Sink and Steptoe basin, respectively. Detailed study of the Carson Sink is warranted by the preponderance of developed geothermal systems in west-central Nevada, a recently completed detailed gravity study, and available seismic reflection data. The detailed gravity and seismic reflection data facilitate identification of favorable settings for geothermal activity in the subsurface of the basin. In contrast, the Steptoe basin lies in a green-field region with no previous development. However, preliminary thermal modeling of the area indicates high potential for sedimentary hosted geothermal systems (Allis et al., 2013). Further, available seismic reflection data permit analysis of the overall architecture of the basin, including fault geometries and thickness of basin-fill, which are critical to understanding both sedimentary hosted and fault-controlled geothermal systems and the potential relationships between them.

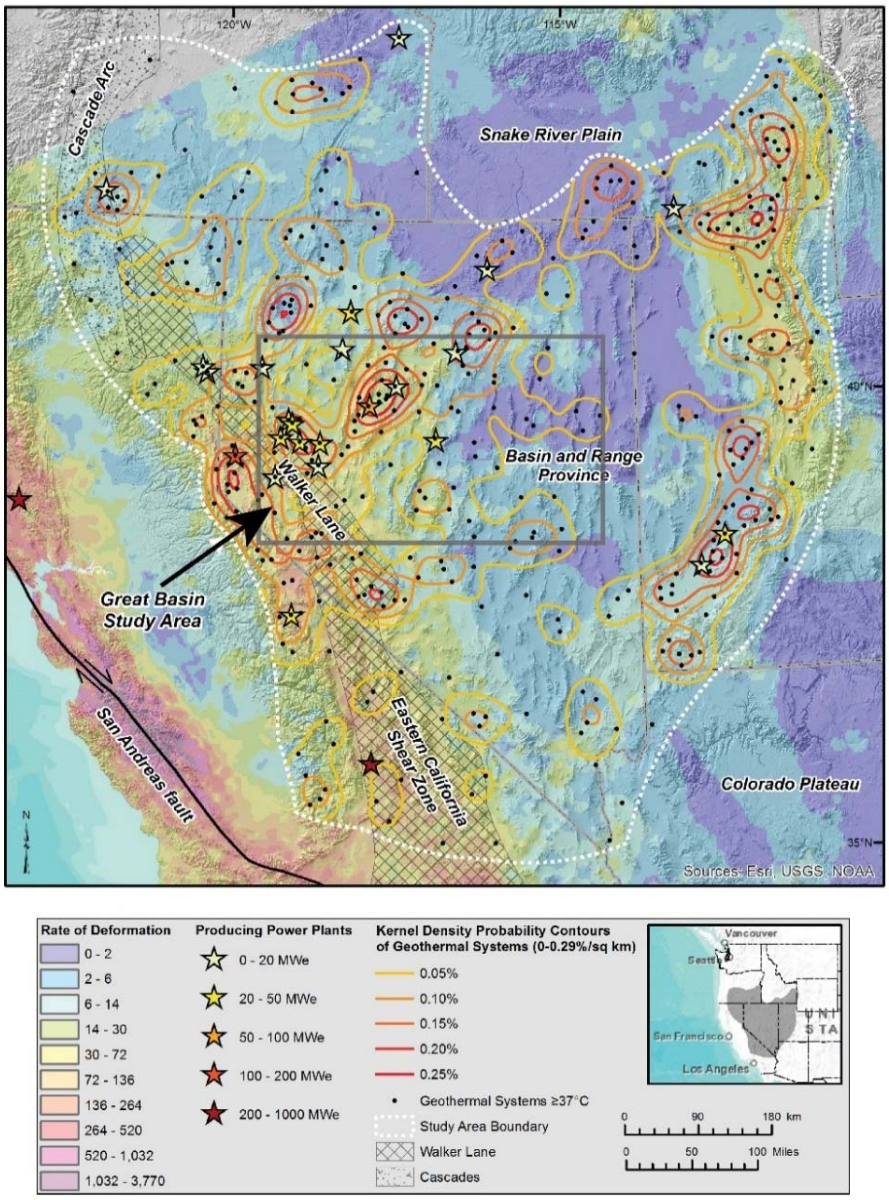

Figure I-1. Density of known geothermal systems (≥37°C) in the Great Basin region plotted on a map showing strain rates (from Faulds and Hinz, 2015). Density contours were derived from a kernel probability estimate in which the distribution of geothermal systems was evaluated within a 50 km radius from a 5x5 km cell size within the Great Basin study area (white outline in figure). This yielded a 0.00 to 0.29% probability range of a geothermal system per km^2 in the study area. Contours in this figure are at 0.05% intervals. Strain rates reflect the second invariant strain rate tensor (10-9/yr; from Kreemer et al., 2012). Power plants and relative capacities are shown by stars. Gray box outlines the study area for this project.

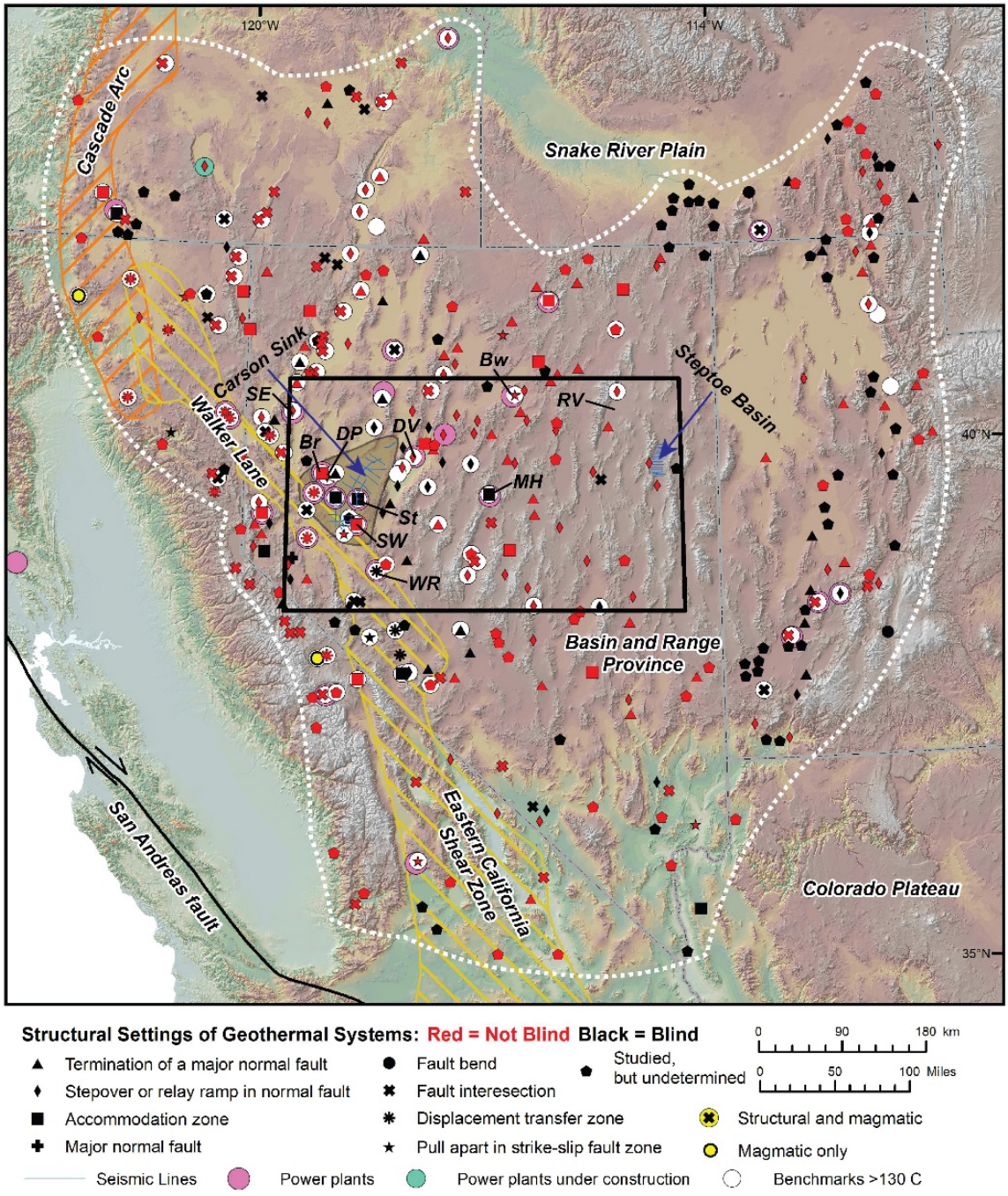

Figure I-2. Structural settings of known geothermal systems (blind and not blind) in the Great Basin region. Black box outlines the study area, which form a continuous transect across the Great Basin region from west-central to eastern Nevada. Brown shaded area outlines the Carson Sink area. Thin blue lines show the available seismic reflection profiles in the Carson Sink and Steptoe basins. White circles delineate systems with temperatures >130ºC, 34 of which were used as benchmarks within the study area. Abbreviations for geothermal systems or areas: Br, Bradys; Bw, Beowawe; DP, Desert Peak; DV, Dixie Valley; MH, McGinness Hills; RV, Ruby Valley; SE, San Emidio; St, Stillwater; SW, Salt Wells; WR, Wild Rose (Don Campbell).

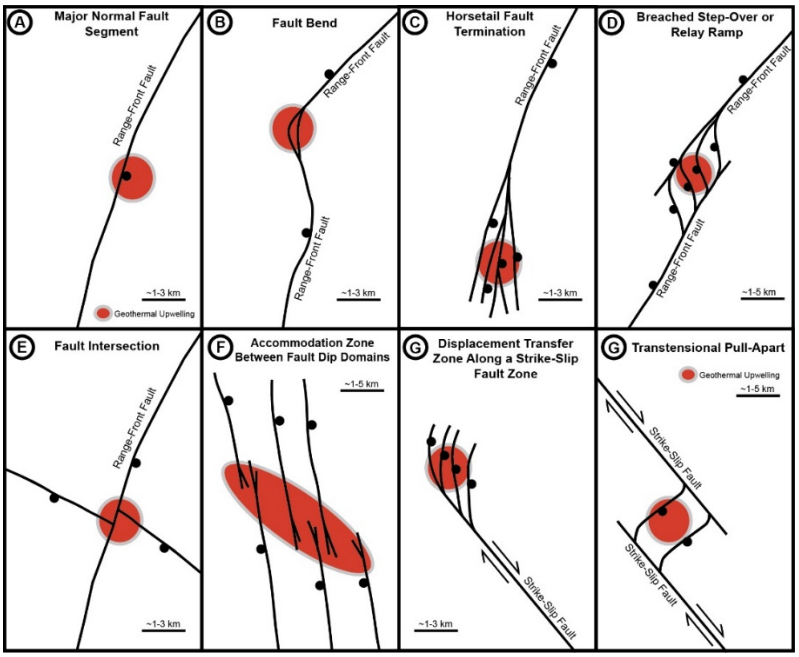

Figure I-3: Characteristic structural settings for geothermal systems in the Great Basin region. A. Major normal fault. B. Bend in major normal fault. C. Fault tip or termination with main fault breaking into multiple strands or horse-tailing. D. Fault step-over or relay ramp breached by minor connecting faults. E. Fault intersection. F. Accommodation zone, consisting of belt of intermeshing oppositely dipping normal faults. G. Displacement transfer zone, whereby major strike fault terminates in array of normal faults. G. Transtensional pull-apart in major strike-slip fault zone. C, D, E, and F host nearly 90% of the known geothermal systems in the Great Basin region (Faulds and Hinz, 2015).

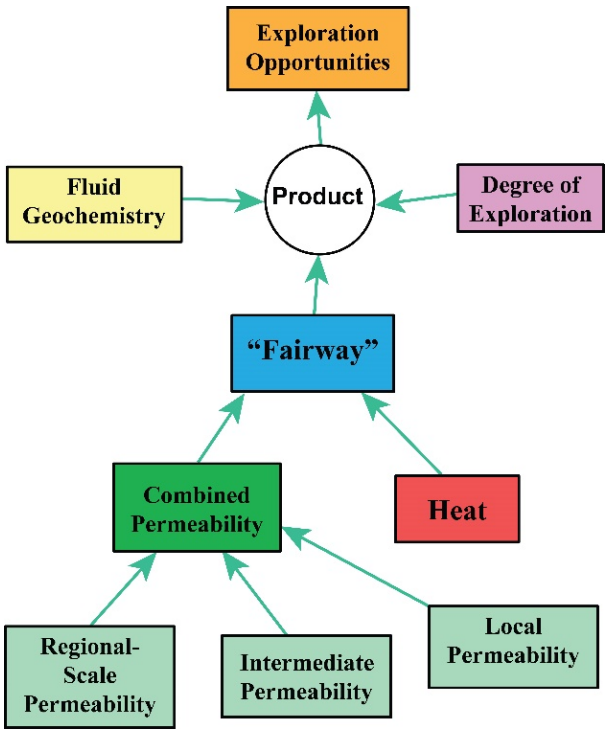

Figure I-4. Schematic flow chart indicating critical components of the play fairway. In addition, exploration opportunities are defined by the fairway, direct evidence from fluid geochemistry, and degree of exploration estimates.

Organization of Report

This report aims to 1) describe project activities according to individual tasks; 2) develop a methodology for distinguishing geothermal play fairways in the extensional to transtensional Great Basin region, which can serve as a model for play fairway analysis in other regions; 3) assess the major implications of the fairway model for elucidating the characteristic *signature* of viable geothermal systems; 4) identify the most highly prospective areas for heretofore undiscovered commercial-grade geothermal systems (both blind and non-blind); 5) provide a comprehensive work plan for Phase II activities, which would focus on the detailed studies of the most highly prospective areas. To accomplish these goals, the report is laid out in the following sections:

- Project Activities.
- Methodology.
- Results and Discussion.
- Phase II Recommendations.

In the Project Activities section, >15 tasks and subtasks are described with reference to explanations of any variances, major deliverables, and accomplished milestones. The raw vector data for each data set are described, illustrated, and broadly interpreted in the Project Activities section. The Methodology section then addresses the data sets according to their groupings in the play fairway model (Fig. I-4). For each individual data set (e.g., Quaternary fault slip rates, gravity, etc.), descriptions of the data input, layer construction, statistics, play fairway weights, and errors are provided in the Methodology section, with emphasis on assigning statistically based relative weightings within and between each major parameter. In addition, the Methodology section contains descriptions of the construction, statistics, and relative weightings of local permeability, intermediate permeability, regional permeability, heat, the fairway, fluid geochemistry, and degree of exploration. Major outcomes from this project are then described in the Results/Discussion section. Phase II Recommendations present a comprehensive review of the work plan, scope, and projected outcomes for a potential Phase II of this project.

PROJECT ACTIVITIES

Fault-controlled geothermal systems are associated with specific structural settings, as well as geochemical and geophysical anomalies. Successful development of these systems relies on accurately defining permeable zones in 3D space. However, no single tool can define the detailed structural framework of a geothermal area and fault segments that host fluids. Conventional and innovative techniques were therefore combined to characterize the signatures of geothermal systems and to provide detailed geothermal potential maps that can guide future exploration efforts. Conventional techniques included interpretation of geologic and geophysical data, whereas innovative methods involved slip and dilation tendency analysis, 3D modeling, and quantitative geostatistical analyses that integrated multiple parameters into a single geothermal potential map. This project marks the first attempt to combine ~10 parameters into a detailed geothermal potential map and robust play fairway analysis.

This one-year project progressed systematically through data compilation, data interpretation, and data synthesis, with discrete quarterly performance periods. The major expected end results for each quarter include the following:

- Quarter 1 – Compilation of available geologic maps, as well as geochemical and geophysical (seismologic, gravity, MT, and seismic reflection) data.
- Quarter 2 – Compilation and analysis of geodetic data; characterize geochemical signatures; delineate locations of favorable structural settings; initiate compilation of ArcGIS databases; and review all databases for adequacy of moving forward and defining any data gaps.
- Quarter 3 – Complete interpretation of geophysical data; characterize geophysical signatures of geothermal activity and/or favorable structural settings for such activity from seismic

reflection, geodetic, gravity, seismologic, and MT data; initiate 3D modeling of select basins; initiation of geostatistical modeling; and slip-dilation tendency analysis of entire study area.

- Quarter 4 – Complete map showing slip and dilation analysis of faults in the study area; complete 3D modeling; complete ArcGIS databases; complete geothermal potential maps; complete predictive analysis of locations for blind geothermal systems; upload all data in specified formats to the NGDS in accordance with the Data Management Plan, and submit the final report and other documents in accordance with the Reporting Requirements document.

Project activities as related to individual tasks are described below. For each task, explanations of any variances, major deliverables, and milestones are also provided. The list of tasks, milestones, and anticipated and actual timing of completion of milestones are shown in Table P-1.

Table P-1. Milestone Summary

Recipient Name: Nevada Bureau of Mines and Geology, University of Nevada, Reno

Project Title: Discovering Blind Geothermal Systems in the Great Basin Region: An Integrated Geologic and Geophysical Approach for Establishing Geothermal Play Fairways

Task #	Task Title or Subtask Title	Milestone or Go/No Go Pt	Milestone # or Go/No-Go Pt #	Milestone Description and Decision Criteria	Milestone Verification Process	Ant. Mo.	Anticipated Completion Qtr	Actual Completion Qtr
1	Review and Interpretation of Geologic Data	Milestone	M1.1	Compilation of geologic maps	Maps will include lithologic data and structural data including faults and folds	3	Q1	Q3
2.1	Review and Interpretation of Seismic Reflection Data	Milestone	M2.1.1	Obtain reflection profiles from Seismic Exchange, Inc.	Purchased profiles will be submitted to NGDS	3	Q1	Q2
2.1	"	Milestone	M2.1.2	Analysis of seismic reflection profiles	Interpretation of seismic reflection profiles for 3D modeling in Task 8 and general characterization of seismic indicators of favorable structural settings	9	Q3	Q4
2.1	"	Milestone	M2.1.3	Characterization of seismic reflection indicators of favorable structural settings	List of characteristics of seismic reflection indicators of favorable structural settings	9	Q3	Q4
2.2	Review and Interpretation of Gravity Data	Milestone	M2.2.1	Compilation and analysis gravity of anomaly maps	Maps showing gravity data for Great Basin study area	3	Q1	Q2
2.2	"	Milestone	M2.2.2	Analysis of gravity data	Maps showing interpreted gravity data with inferred faults	9	Q3	Q3
2.2	"	Milestone	M2.2.3	Identify gravity signatures for favorable structural settings	List of gravity anomaly indicators of favorable structural settings	9	Q3	Q3
2.3	Review & Interpretation of Magnetotelluric Data	Milestone	M2.3.1	Compilation of MT data	MT data maps for select parts of the Great Basin study area	3	Q1	Q2
2.3	"	Milestone	M2.3.2	Analysis of MT data	Interpreted MT data and list of characteristics of MT signatures for known systems	9	Q3	Q3
2.4	Review & Interpretation of Seismologic Data	Milestone	M2.4.1	Analysis of spatial distribution of earthquakes	Maps showing earthquake distribution relative to structural setting and known geothermal systems	3	Q1	Q2
2.4	"	Milestone	M2.4.2	Characterization of seismologic character of known geothermal areas	Establish seismologic signature of known geothermal systems	6	Q2	Q3
3	Review and Interpretation of Geochemical Data	Milestone	M3.1	Compilation of geochemical data	Maps showing geochemical data for Great Basin study area	3	Q1	Q1
3	"	Milestone	M3.2	Analysis of geochemical data	Characterization of geochemical signatures of known geothermal systems and evaluate against the rest of the data for additional anomalies	6	Q2	Q2
4	Review and Interpretation of Geodetic Data	Milestone	M4.1	Compilation of geodetic data	Maps showing geodetic strain for Great Basin study area	3	Q1	Q1
4	"	Milestone	M4.2	Analysis of geodetic data	Produce list of geodetic indicators of known geothermal systems	6	Q2	Q3
4	"	Milestone	M4.3	Produce strain maps	Produce velocity gradient and strain rate maps with estimates of slip rates and styles for active faults	10	Q4	Q4
5.1	GIS Database Compilation	Milestone	M5.1	Compilation of all data into ArcGIS	Produce well organized ArcGIS data sets for study area	6	Q2	Q2/Q4
5.2	Preliminary Modeling	Milestone	M5.2	Prepare preliminary predictive model of geothermal potential	Map showing preliminary geothermal potential and data gaps	6	Q2	Q3
5.3	Database Management	Milestone	M5.3	Finalize assembled data sets at end of each quarter	Submit assembled data sets to DOE-GDR and NGDS	3, 6, 9, 12	Q1, 2, 3, 4	Q4
6	Identify and Characterize Structural Settings	Milestone	M6.1	Complete analysis of structural framework	Maps showing structures that may host blind geothermal systems	8	Q3	Q3
7	Slip and Dilation Tendency Analysis	Milestone	M7.1	Complete slip and dilation tendency analyses	Map showing slip-dilation tendency of faults for Great Basin study area	8	Q3	Q3
7	"	Milestone	M7.2	Conduct 3D slip and dilation tendency analysis for Carson Sink and Steptoe basins	Model showing slip and dilation tendency in 3D for Carson Sink and Steptoe basins	11	Q4	Q4
8	3D Geologic Modeling of Selected Basins	Milestone	M8.1	Construct 3D models of two basins	3D models constructed from geologic map data, seismic reflection profiles, and gravity data	12	Q4	Q4
9	Quantitative Ranking of Blind Geothermal Potential	Milestone	M9.1	Final rankings table and predictive maps	Database containing rankings and preliminary maps contouring geothermal potential	12	Q4	Q4
10	Complete Geothermal Potential Maps of Study Areas	Milestone	M10.1	Final geothermal potential maps	Final prediction of known and potential blind geothermal systems	12	Q4	Q4
11	Identify Data Needs for Phase II	Milestone	M11.1	Robust data sets indicating high potential, comparison with developed areas	Selection of most prospective areas for undiscovered blind geothermal systems for further study	12	Q4	Q4
12	Final Reporting and Project Review	Milestone	M12.1	Synthesis of project	Submittal of report and databases	12	Q4	Q4

Task 1.0 – Review and Interpretation of Geologic Data

The approach of this task was to compile various forms of geologic data to characterize known geothermal systems and facilitate identifying blind systems across the study area. Geologic data are critical for evaluating the stratigraphic and structural framework conducive for geothermal activity, as the lithologies and pattern, age, and orientation of faulting are directly related to permeability, fluid flow, and reservoir mechanics. Major efforts for this task focused on compiling 1) available geologic maps for the study area, 2) Quaternary fault data, 3) well data, and 4) a regional temperature model at 3 km depth.

Because Quaternary faults are associated with most known high enthalpy geothermal systems (Bell and Ramelli, 2007, 2009), a vastly updated Quaternary fault layer was prepared with new attribute fields for slip rate and recency (i.e., age) of faulting for each fault (Figs. P-1, P-2, and P-3). Thorough and time-intensive Qa/Qc of the USGS Quaternary fault database (USGS, 2010) was completed, including nearly 7,773 individual fault segments in the study area. Published and unpublished fault investigations and observations using Google Earth were used to update the data set. The attributes were updated and the Qa/Qc methods were employed to filter out most input errors. The new Quaternary fault database was then loaded into our ArcGIS platform for integration with the other data sets. In essence, this effort focused on summarizing the past 2.6 Ma of faulting history in the region and relating that history to known geothermal activity, thus complementing the seismologic and geodetic analyses with a longer term view of tectonism.

Fault activity was evaluated using datum, such as lacustrine and alluvial fan features, and the geomorphic expression of faults. Fault activity was judged as one of five categories: historic, ≤15 ka, ≤130 ka, ≤750 ka, and ≤2.6 Ma. When uncertainties arose and the exact activity category was unclear, the older category was usually deferred to because it is inclusive of the younger categories.

Fault slip rates were determined using published rates and apparent offsets in surfaces with estimated ages. Five slip rate categories were considered: 0.0001 m/ka, 0.001 m/ka, 0.01 m/ka, 0.1 m/ka and rates greater than 0.1 m/ka, which are reported as the best estimates obtainable (usually from published literature). For normal dip-slip faults, vertical fault slip rates were determined. As an example of the strategy used, considering a 2 Ma old datum and the 0.1, 0.01, 0.001, and 0.0001 m/ka categories, nominal vertical fault offsets of 200 m, 20 m, 2 m, and 0.2 m would be expected, respectively. For a 500,000 year old unit, the offsets would be 50 m, 5 m, 0.5 m, and a possible lineament, respectively. Similar offsets were determined for other age units, and collectively these were used as a guide for estimating the vertical fault slip rate. The faster fault slip rates were adopted from published literature, if available, or determined using an empirical relationship between vertical fault slip rate and basal fault facet height developed by dePolo and Anderson (2000). Quaternary strike-slip faults can be poorly expressed at the surface, making some faults difficult to characterize. Fortunately, many strike-slip faults had published slip rates. For some faults, lateral offsets were observed, and the age of the offset sediments was estimated to obtain a rate. For the remaining faults, relative fault expression, such as fault continuity, the nature of the geomorphic expression, and the width of a fault zone (narrow versus widely distributed) were considered in the estimation of the slip rate.

Uncertainties were incorporated into our analysis of Quaternary faults. Fault locations are generally accurate within ~100-200 m in the worst cases. This uncertainty arises from digitization and map projection errors. The estimations for age of the most recent rupture event are inclusive of younger ages, because erosion and burial can make a young rupture appear indistinct. Most fault slip rates are grouped into categories with an order-of-magnitude difference between them. Most fault slip rates are probably no more precise than plus-or-minus half-an-order-of-magnitude in value. For slip rates >0.1 m/ka, uncertainties generally decrease an order of magnitude by a factor of 2 to 3, and we used 2 to be conservative and capture the upper end range of error.

An update of a well database that includes all types of wells drilled in the study area was made to facilitate an analysis of the degree-of-exploration. This database includes geothermal wells, oil and gas wells, mineral exploration wells, water wells, and environmental monitoring wells. Information on the depth of the wells, temperatures, date, and type of well was compiled and is described in detail in Task 3 results. In addition, available cuttings from deep wells in the Carson Sink and Steptoe basin were logged

to provide critical constraints for interpreting seismic reflection profiles and developing the 3D models of these areas.

A digital map of temperatures at 3 km depth was used to model heat input for this project (Fig. P-4). This map was created by Southern Methodist University as part of a project to model geothermal potential in the Great Basin (Coolbaugh et al., 2005). The map was created by first modeling heat flux across the Great Basin using available well temperature data excluding geothermal wells. The composition of near-surface rocks (taken from regional geologic maps) was then used to estimate near-surface thermal conductivities in order to convert the regional heat flux values into local temperature gradients. This made it possible to distinguish low-thermal-conductivity basin-fill deposits from higher thermal conductivity bedrock lithologies within mountain ranges. The thermal conductivities were then used to interpolate temperatures between wells to a depth of 3 km. [grid = T3K_20b]

The model used in this work provided adjustments for gradients and heat flow based on the location of wells within alluvial (or other unconsolidated) sediments versus coherent rock. Thermal conductivities in unconsolidated fill can be on the order of 2 times lower than those in rock (e.g., Robertson, 1988) indicating that for the same gradient, the heat flow associated with a well completed in rock could be up to twice that for a well in unconsolidated sediments (e.g., Blackwell and Chapman, 1977).

Our review of the available geologic and geophysical data led to some changes in the project. First, the boundaries of the study area (Fig. I-2) were redefined slightly in Q1 to a discrete E-W transect across Nevada, which allowed for inclusion of more robust geologic and geophysical data sets (e.g., northwestern part of area where new MT data was recently collected by Dr. Wannamaker on another DOE project—see task 2.3). In addition, we initially underestimated the amounts of available data. Although largely completed by Q2, incorporation of additional data continued into the early part of Q4.

We also note that based on feedback on the Q1 report from the technical monitoring team (TMT), we incorporated multiple layers on land use status/ownership from several sources (e.g., BLM and NREL) into our data platform. These layers are critical for selecting the most promising geothermal prospects for detailed study in Phase II, as the selections depend on both the geothermal ranking, as determined on our new geothermal potential map, as well as the land status. Public vs. private land, wilderness lands, wildlife refuges, and transmission corridors were delineated and are discussed in greater detail in the section describing results.

Explanation of Variance: None. However, this task took longer than expected due to large amounts of available data for the region and the need for quality control efforts on the Quaternary fault databases.

Deliverables: 1) Quaternary fault maps with 500 m buffers around each fault ; 2) Quaternary fault map showing age of Quaternary faults; 3) Quaternary fault map showing slip rates on normal and strike-slip faults; and 4) map showing well and spring temperatures and geothermometry.

Milestones: M1.1 largely completed in Q2 but finalized in latter part of Q3 (Table P-1).

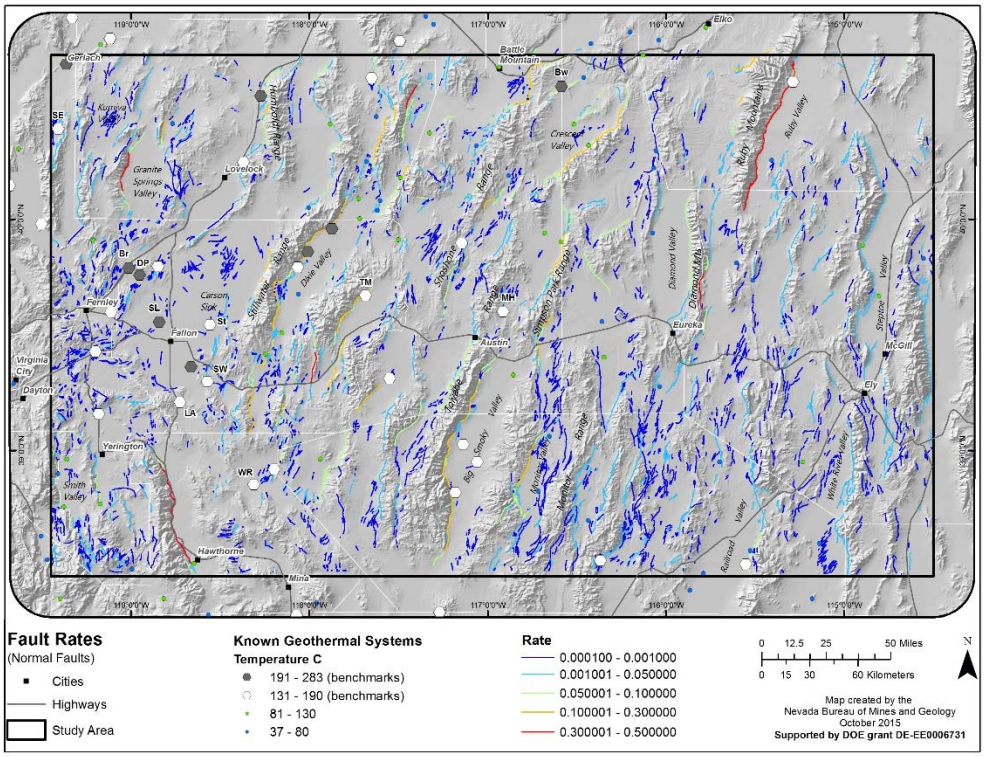

Figure P-1. Slip rates of Quaternary normal faults within the study area.

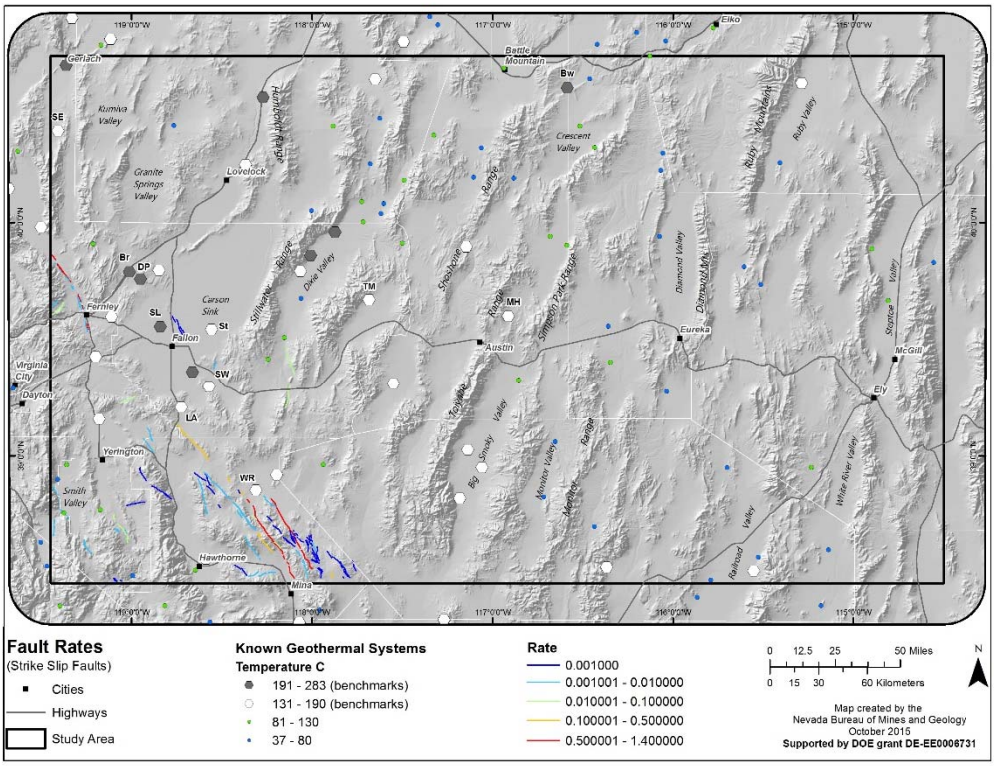

Figure P-2. Slip rates of Quaternary strike-slip faults within the study area.

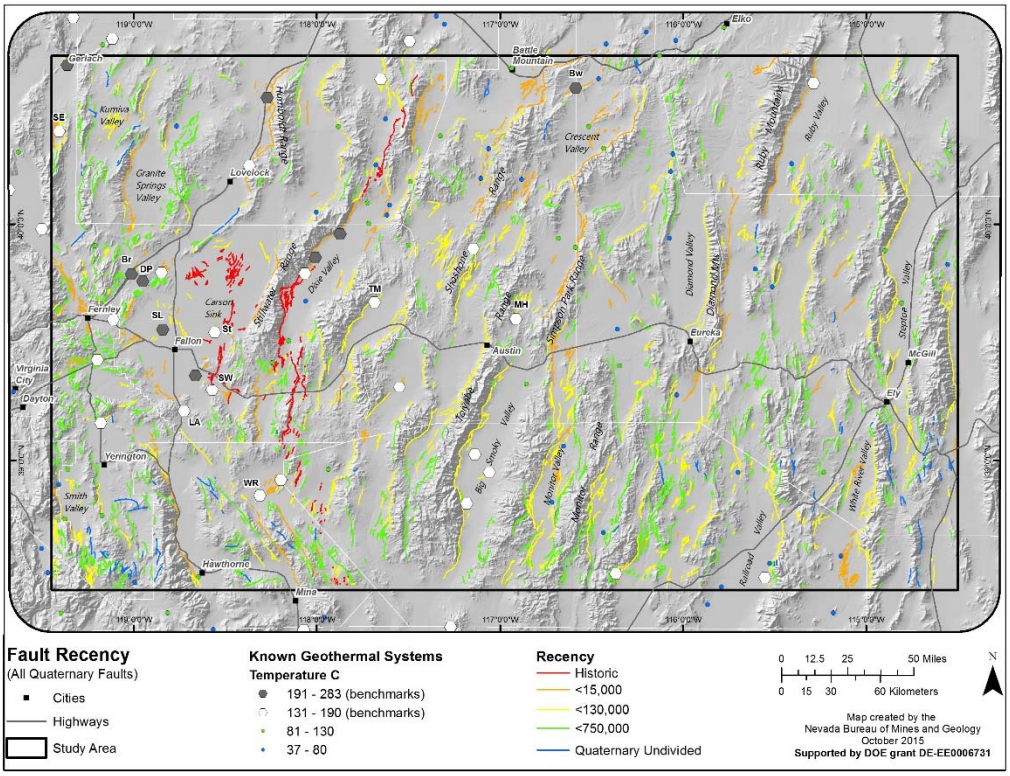

Figure P-3. Recency or age of Quaternary faults within the study area.

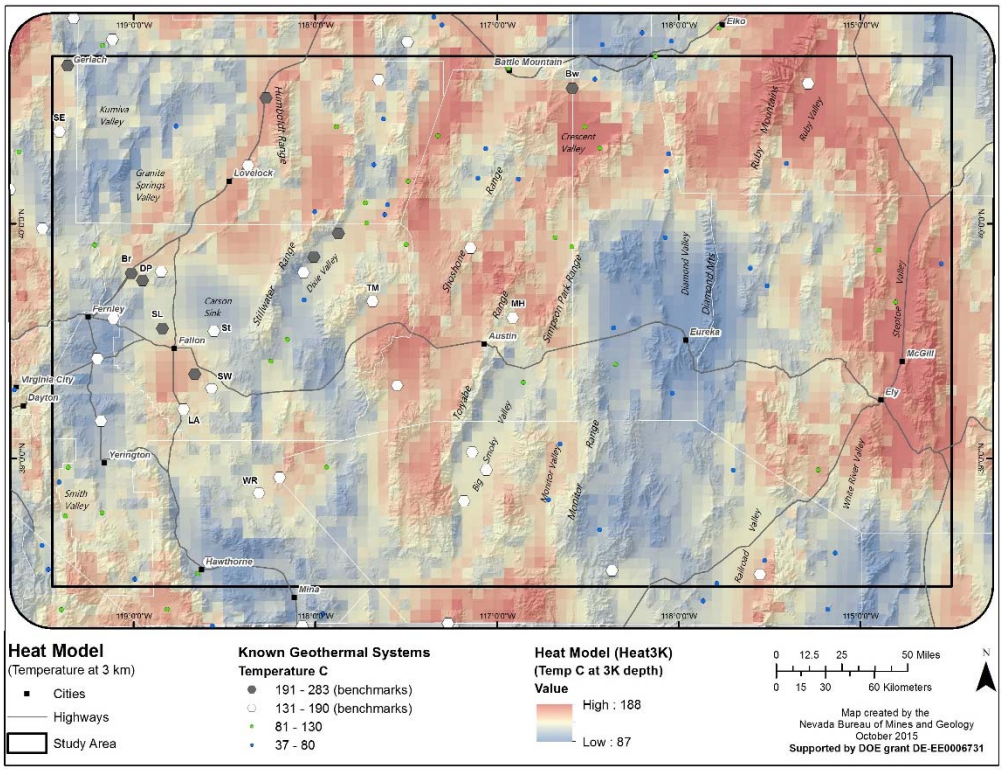

Figure P-4. Heat model showing temperatures at 3 km depth.

Task 2.0 – Review and Interpretation of Geophysical Data

The approach of this task was to compile various types of geophysical data to characterize known geothermal systems and facilitate identification of blind systems (paralleling the structure of Task 1). This was achieved in accordance with the following subtasks.

Subtask 2.1 – Review and Interpretation of Seismic Reflection Data: This task was focused on interpreting ~400 miles of seismic reflection profiles for the Carson Sink and Steptoe basin areas, which respectively anchor the western and eastern ends of the study area (Fig. I-2). The profiles were used as the basis for constructing cross sections of these two basins, which in turn were used as the primary building blocks of the 3D models (Task 8).

When properly processed, the peaks and troughs in a surface seismic reflection profile represent abrupt changes in seismic impedance. Seismic impedance is the product of seismic propagation velocity and density. Accordingly, these peaks and troughs, also called reflection events, indicate marked changes in velocity and/or density. A major assumption in the surface seismic reflection method is that these changes in velocity and density (the peaks and troughs) correspond to changes in rock properties (e.g. lithology).

Surface seismic reflection methods have found widespread success in the oil and gas industry, and are beginning to be used in the geothermal arena. In oil and gas environments, sedimentary rocks are laid down in long nearly horizontal layers. These layers are locally cut by faults which lead to vertical offsets of these beds. Seismic reflection profiles over such areas show a series of reflection events which are coherent over long lateral distances. These reflection events commonly correspond to changes in lithology, and show vertical offsets when cut by faults. As part of the interpretation process, their lateral positions and arrival time on the profile can be picked. With the wealth of velocity data available in these areas, time picks can be converted to depth, leading to maps of fault locations, bed thickness, and depth.

In contrast, areas with high geothermal potential are commonly in environments dominated by volcanic and metamorphosed rocks, with a high degree of structural complexity. With the exception of valley fill, the long coherent reflection events seen in sedimentary basins are lacking. One further complication in applying reflection seismic methods in geothermal areas is the dearth of velocity information. In most cases the only available velocity information needed to convert from time to depth are the highly unreliable move out velocities generated during processing. Nonetheless, when integrated with well data and gravity derived depth estimates, arrival times of a limited number of formations can be picked and converted to depth. Surface mapping and gravity data are also useful in constraining fault locations. Although not nearly as detailed and reliable as maps produced in sedimentary basins, these results can be integrated into a geological model to identify structural style elements.

About 400 miles of existing 2D seismic reflection profiles were obtained from Seismic Exchange, Inc. (SEI), for the Carson Sink and Steptoe basins. The most geologically critical and data-rich profiles were obtained. The acquisition vintage of these profiles ranged from early 1970's to mid-1980's.

Most of the profiles from the Carson Sink basin were only available as scanned images of paper plots of processed data. A few Carson Sink lines were also available as digital data (SEGY files). For all Carson Sink lines, we used the original processing applied by the companies that acquired the data. For the most part, this did not include migration. If available, digital files were used to produce time to depth converted seismic profile images, which were then used in interpretation. Otherwise, the time domain scanned paper plots were used in the interpretation. Figure P-5 below shows a base map for the Carson Sink basin seismic lines, and interpreted profiles are shown in Appendix A.

Two different processing vintages of reflection profiles from the Steptoe basin were delivered by SEI. The first was the original processing applied by the companies which acquired the data. The second was processing performed by SEI and its subcontractors over the last two years. Profiles with original processing were only available as scanned images of paper plots. SEI processing results were supplied both as scanned images and digital data (SEGY files). Unfortunately, about half of the SEI processing efforts included the application of a very strong lateral coherency filter. This filter obliterated much of the geology, and rendered those digital files useless. Both processing vintages included migration results. When useful migrated profiles were available in digital form, they were utilized to generate time to depth converted

images used in interpretation. For other lines, migrated scanned images were passed on for interpretation. Figure P-6 below shows a base map for the Steptoe basin seismic lines, and interpreted profiles are shown in Appendix B.

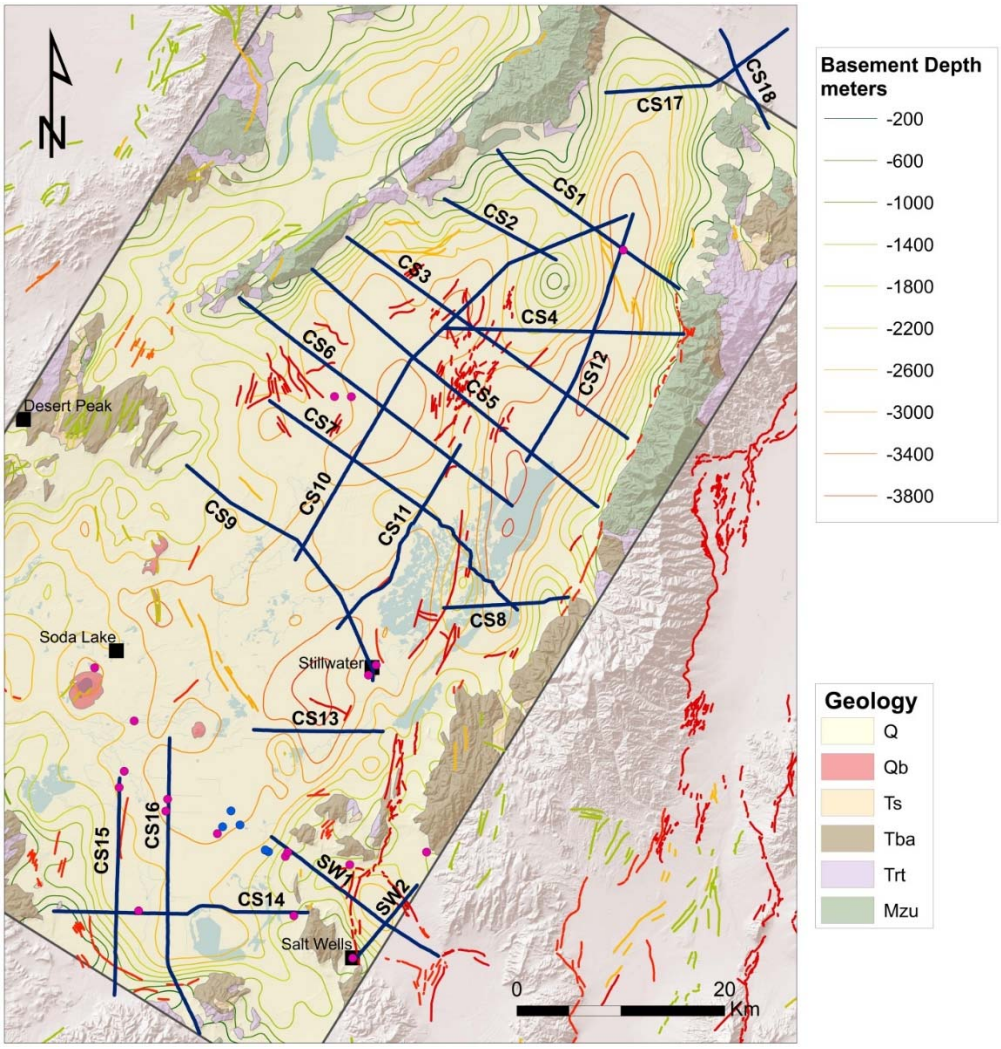

Figure P-5. Base map showing seismic reflection profiles from the Carson Sink overlain on sedimentary basin-fill depths and generalized geologic map. Red and blue dots are wells with available data from cuttings or core. Quaternary faults are shown by red, yellow, and olive green lines. The 3D model (Task 8) incorporates the northern part of the basin.

Two different work flows were used for interpretation of these data. If only a scanned paper image was available for a particular line, a time domain flow was pursued. If usable SEGY files were available, a depth domain flow was implemented. For the time domain flow, if gravity derived depths to formation boundaries were available, they were converted from depth to time. Similarly, if nearby well data were available, formation tops from these wells were converted from depth to time. These were then plotted on top of the scanned seismic profile. These profiles were then interpreted for a limited number of faults and lithologies by drawing lines on the time domain images. Those lines were then hand digitized. These digitized points were then converted from time to depth. The result of this process was a table of NAD83 UTM coordinates for each picked horizon or fault. These tables were then incorporated into the 3D geological models.

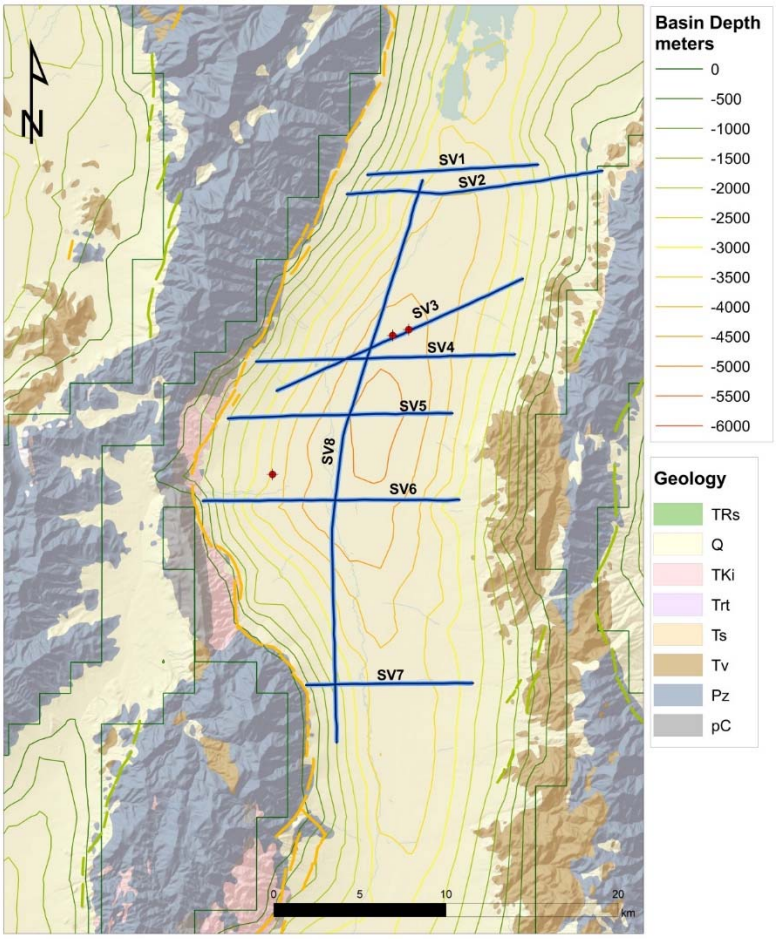

Figure P-6. Base map showing Steptoe basin seismic reflection profiles and depth of Neogene sedimentary basin-fill. Analyzed profiles for 3D model are shown in blue lines. Red dots are wells with available data from cuttings. Yellow and light green lines denote Quaternary faults.

If usable digital seismic data in the form of a SEGY file were available for a particular line, a depth domain approach was followed. The seismic traces were first converted from time to depth. If gravity or well information was available, plots of the depth domain traces were produced overlain by the gravity and well depth data. These plots were then used for interpretation. Since these interpretations were already in depth, they were passed on directly for incorporation into the geological model.

Time to depth and depth to time conversion are at the root of both of these flows. Before these conversions can be performed, a detailed and reliable interval velocity model covering the area of the seismic profile must be in hand. The quality of the time/depth conversion is directly related to the quality of the interval velocity model.

In oil and gas areas, interval velocity models are typically developed using a combination of well log sonic logs and vertical seismic profile (VSP) velocity data, also called check-shot data. Well log sonic velocities are derived from very high frequency measurements. They are commonly known to differ from low frequency seismic velocities by as much as 10%. For this reason, well log sonic velocities are usually "check-shot corrected" before being incorporated into interval velocity models for time/depth conversion. In modern times, interval velocity estimates can be supplemented by the very expensive process of pre-stack depth migration velocity analysis. With the wealth of velocity data available in many sedimentary basins, very reliable interval velocity models can be produced.

The situation in geothermal areas is markedly different. Very few sonic logs are available, and VSP or check-shot data are virtually nonexistent. An alternative is to use interval velocities derived from stacking velocities, also called normal moveout (NMO) velocities. Interval velocities inferred from NMO velocities

was the method used in this project.

NMO velocities are derived during processing. In unstacked seismic data, reflection events from a single reflector will arrive at later and later times with increasing offset between the source and the receiving geophone. NMO velocities are corrections which flatten reflection events in unstacked seismic data. They compensate for the additional time it takes a seismic wave to go from source to reflecting boundary to geophone associated with offset.

NMO velocities can be closely approximated as a root mean square (RMS) average of the interval velocities along the seismic ray path. Dix (1955) developed an algorithm for inverting interval velocities from NMO velocities. This inversion process is notoriously unstable. Very small changes in NMO velocities can lead to very large changes in interval velocity. This instability grows with increasing time or depth. In spite of this instability, NMO derived interval velocities are often the only path open for performing time/depth conversions.

Fortunately, the NMO velocities derived in processing the seismic profiles used in this project were either listed on the scanned images or supplied as separate digital files. For each profile, an interval velocity model was obtained from the NMO velocities using a program included in the Seismic Un*x (SU) processing package (Cohen and Stockwell, 2008). In particular, SU program velconv implements the Dix (1955) algorithm. It has options for converting NMO velocities to interval velocities in time or depth, as well as producing tables of depth as a function of time or time as a function of depth. For each scanned image profile, an interval velocity model was developed using the posted NMO velocities and SU program velconv. If gravity and well log formation tops were available for that particular profile, their depths were converted to time using the depth to time tables produced by this same program.

Figure P-7 below shows one such profile. This is for Carson Sink basin line CS1. Analysis of this line was previously published by Hastings (1979), but we reinterpreted the profile. The magenta line in the figure shows the top of the Mesozoic basement inferred from gravity data after depth to time conversion. The figure also shows the well track for the Standard – Amoco S.P. Land Co. No. 1 well, with density units color coded according to the key. Depths to the top of each unit were converted from depth to time. Profile CS1 passed very close to this well.

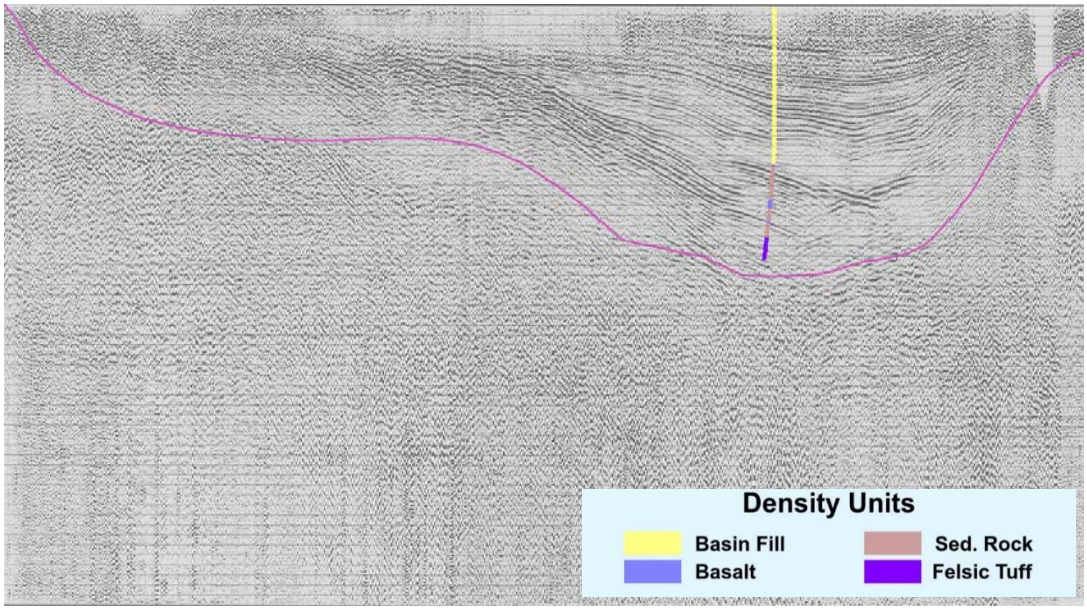

Figure P-7. Seismic profile of Carson Sink basin line CS1 (looking northeast). The magenta line shows the gravity inferred top of Mesozoic basement after depth to time conversion. The well track of the Standard – Amoco S.P. Land Co. No. 1 well is also shown, with density units color coded, as shown in lower right. Seismic data owned or controlled by Seismic Exchange, Inc.; interpretation is that of the University of Nevada, Reno.

Guided by the well and gravity data, these profiles were then interpreted. Tops of a limited number of lithologies and fault locations were drawn on the profiles. These were then hand digitized and converted from time to depth. Figure P-8 shows an interpreted profile for Carson Sink basin profile CS1.

Figure P-9 displays the interpretation picks shown in Figure P-8 after conversion from time to depth using the NMO derived interval velocity model. The color coded velocities in this figure are averages of velocities over each formation obtained from a sonic log run in the Standard – Amoco S.P. Land Co. No. 1 well. They are not the NMO derived interval velocities used to perform the time to depth conversion. Their primary purpose is to highlight the various formations.

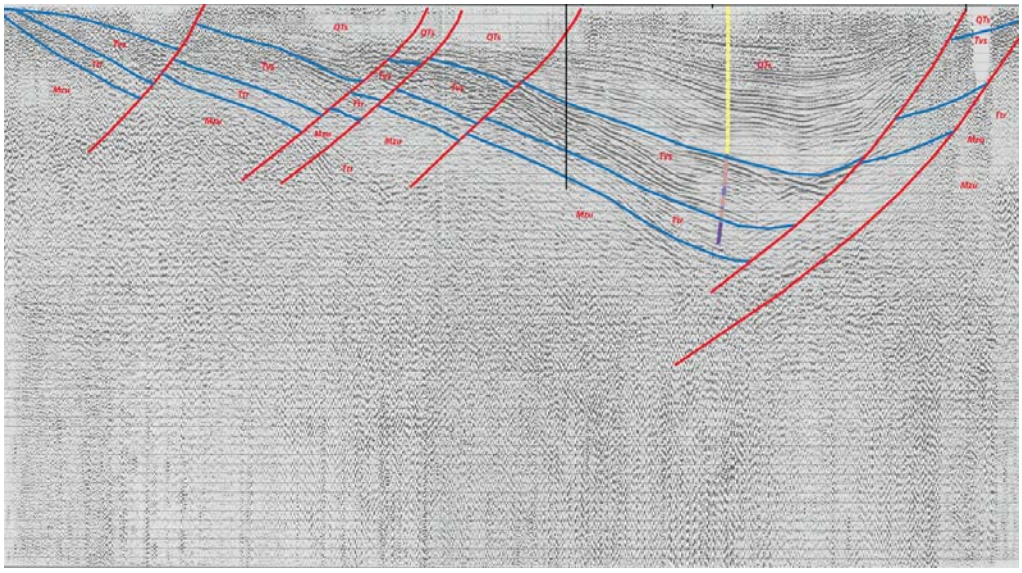

Figure P-8. Interpreted Carson Sink basin profile CS1. Normal faults are shown in red, and lithologic contacts are blue. See Figure P-7 for the legend. Mzu, Mesozoic basement undivided. Seismic data owned or controlled by Seismic Exchange, Inc.; interpretation is that of the University of Nevada, Reno.

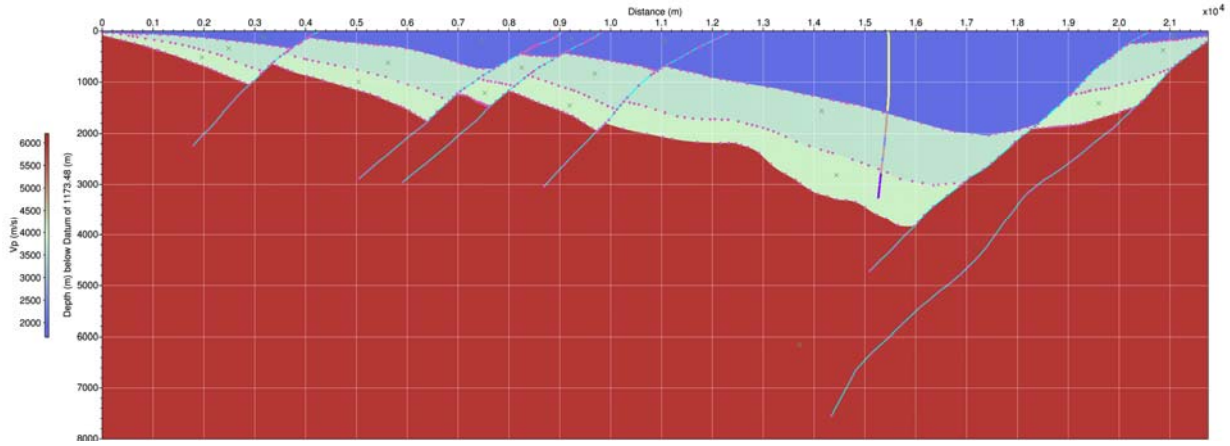

Figure P-9. Time to depth converted picks of interpreted horizons and faults from Figure P-8.

If digital SEGY files were available for a profile, an interval velocity model was created using the NMO velocities and SU program velconv. Digital traces were then directly converted from time to depth using SU program suttoz with NMO derived interval velocities as input. Since the gravity and well data were already in depth, there was no need to convert these to time.

Figure P-10 shows one such profile: CS12. This profile intersects profile CS1 very near the Standard – Amoco well. Again, the magenta line shows the top of the Mesozoic inferred from gravity data. The well track of the Standard – Amoco well is also shown with density units color coded following Figure

P-7.

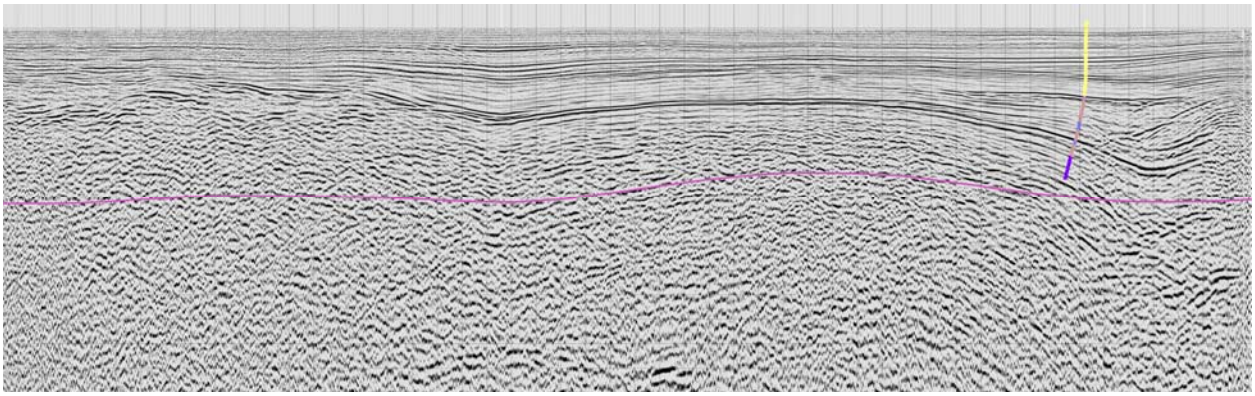

Figure P-10. Profile CS12 after depth conversion. Magenta line shows gravity-inferred top of Mesozoic. The well track of Standard – Amoco S.P. Land Co. No. 1 well is shown, with density units color coded following Figure P-7. Seismic data owned or controlled by Seismic Exchange, Inc.; interpretation that of University of Nevada, Reno.

Through integration with available geologic maps, well data, and gravity surveys, the seismic reflection profiles constrained the structural and stratigraphic framework of the Carson Sink and Steptoe basin, as well the overall basin architectures. This included important findings directly relevant to the geothermal potential of these basins, particularly for identifying favorable structural settings that may host heretofore undiscovered blind geothermal systems. For example, in the Carson Sink, at least two major fault terminations and a major accommodation zone were identified in the northern part of the basin. In the Steptoe basin, a major step-over in the range-front fault that bounds the western side of the basin was confirmed with the seismic reflection data, which enhances the geothermal potential of the area. However, the seismic reflection data also suggest that the basin may not be as deep as sparse gravity data would imply, which may limit the potential for sedimentary hosted geothermal systems.

Our analysis of the seismic reflection profiles did not reveal any unusual signatures associated with the favorable structural settings and any known geothermal activity. It is important to note, however, that the available data did not include a known geothermal system. Further, the quality of the data are limited due to their vintage and lack of SEGY files for most profiles. Thus, comparison of the favorable structural settings along profiles with various seismic indicators, such as reflector coherence, frequency content, and amplitude, did not reveal any correlations with geothermal activity. We therefore conclude that the available seismic reflection profiles in this region are generally best incorporated as an additional constraint on defining the structural and stratigraphic setting, but probably cannot be used an independent parameter for constraining geothermal potential.

Explanation of Variance: Purchase of the profiles from SEI was delayed slightly due to finalizing a license that allowed for publication of interpretations but honored SEI's ownership and control of the profiles. Images of the interpreted profiles, without original digital or shot-point data and without original industry names of the profiles, will be allowed for publication and submittal to the NGDS. Once the license was completed, purchase of the profiles and analysis and interpretations proceeded on schedule. SEI has been very responsive to reviewing interpretations and approving release of the interpretations.

Deliverables: Interpretations of 14 profiles from the Carson Sink (Appendix A) and 8 profiles from the Steptoe basin (Appendix B). Digital versions of the interpreted profiles were also incorporated into the 3D models.

Milestones: M2.1.2 and 2.1.3 were completed in Q4 (Table P-1).

Subtask 2.2 – Review and Interpretation of Gravity Data: Gravity data are available for the entire study area, including gravity gradients, complete Bouguer anomalies, and depth to basement maps. In addition, a new detailed gravity survey was completed in the Carson Sink in 2013. Results of this detailed survey

suggest that terminations in gravity gradients, as well as broad saddles between gravity lows, can be correlated with fault step overs, terminations, intersections, and accommodation zones. Coarser gravity surveys can also provide information on the locations of major faults zones, furnishing important constraints on the geological model and aiding in time to depth conversions. Gravity data can also provide bounds on reflector depths for velocity estimation in seismic reflection data. All these data were compiled and evaluated. Suitable data were analyzed for indicators of structural style and interpreted for depth to basement.

Available gravity data sets were collected and integrated and edited for consistency by Dr. Gary Oppliger. Approximately 44,400 gravity stations were utilized for the extended study area (Fig. P-11). In order to uniformly integrate the very diverse vintage of data and identify inconsistent stations for rejection, a new direct earth physics model and gravity reduction protocol were implemented. Forward topographic and isostatic compensation crustal models were constructed for the study area. The model predicts theoretical on-surface gravity acceleration at each cell of the 200 m terrain model. The model has separate terrain above mean sea level (complete Bouguer response), isostatic 30 km depth compensation, and normal gravity field components.

The horizontal gradient magnitude (HGM) of the gravity anomaly was calculated using the USGS formula HGM = SQRT (dx*dx + dy*dy) * 1000 (with units of microGals per meter), where dx is the eastward gravity anomaly change over one meter and dy is the northward gravity change over one meter.

Station spacing affects the capture of gravity signal from geologic structure. A station spacing of 2 km to 4 km in a grid pattern is considered top quality coverage for this region. However, 3/4 of the basins had significantly wider spaced stations. Typically, stations were along roads at 1 to 2 km intervals, but the roads might be spaced 10 km to 15 km apart. A compensating factor for the HGM grids is that major basin defining structures produce 5 to 15 km wide gravity gradient anomalies, so even a few roads across a large basin can capture these. As much as 5% of the older source data was rejected based on elevation comparison tests against a USGS NED 30 m elevation model. Typically, elevation deviation of more than 15 m were considered for rejection based on CBA anomaly spatial consistency.

Resulting gravity anomaly grids were compared to USGS and Geonet data sources. SBA fields were identical to 0.1 mgal source data truncation level. The CBA calculation included a full terrain correction for all stations, which typically differed from the original terrain corrections by less than 1 mgal in low relief areas and 3 mgals in high relief areas. The computed gravity anomaly horizontal gradient values are presumed to be reproducible to better than 15%.

Explanation of Variance: None**.** However, Dr. Gary Oppliger, an expert in gravity work, was added in Q1 to the UNR team to assist in compiling and interpreting the gravity data.

Deliverables: The following gravity products were produced for this project:

- A complete set of gravity results as 400 m grids in csv format was compiled. These files contained all project gravity results and computation fields in a 400 m grid tabular format.
- Isostatic anomaly reduced at 2.40 and 2.67 g/cc (complete Bouguer with isostatic correction; Fig. 12).
- Vertical derivative isostatic anomaly reduced at 2.40 g/cc.
- Horizontal gradient magnitude isostatic anomaly reduced at 2.40 g/cc.
- Horizontal gradient magnitude of the first vertical derivative reduced at 2.40 g/cc.
- Density equivalent basin depths. On the basis of the gravity data, the depth to Mesozoic basement was constructed for the Carson Sink 3D model with 1600 m cells.
- Several iterations and refinements for a set of extracted gravity traverses (xyz tables) at 400 m sample spacing were provided for all the Carson Sink purchased seismic lines with added length extensions for the purpose of GYMSYS density modeling.
- Extracted gravity traverses (xyz tables) for all seismic reflection-geologic cross sections.

Milestones: M2.2.1 was completed in Q2; M2.2.2 and 2.2.3 were completed in Q3 (Table P-1).

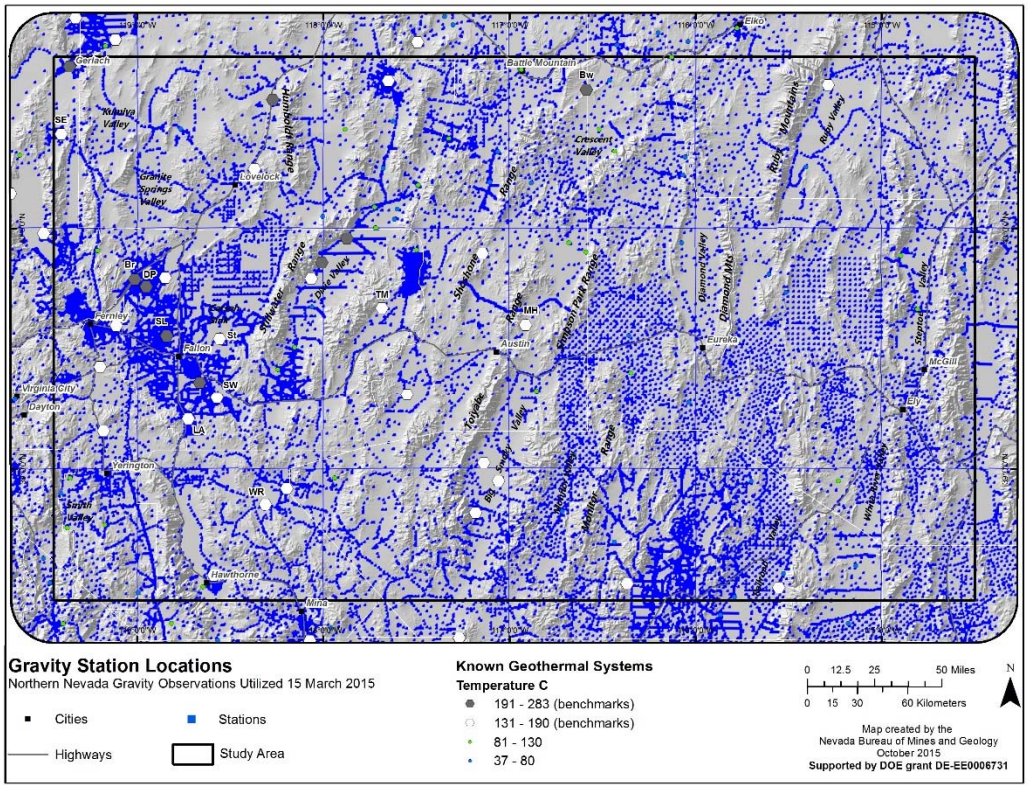

Figure P-11. Location of gravity stations in the study area.

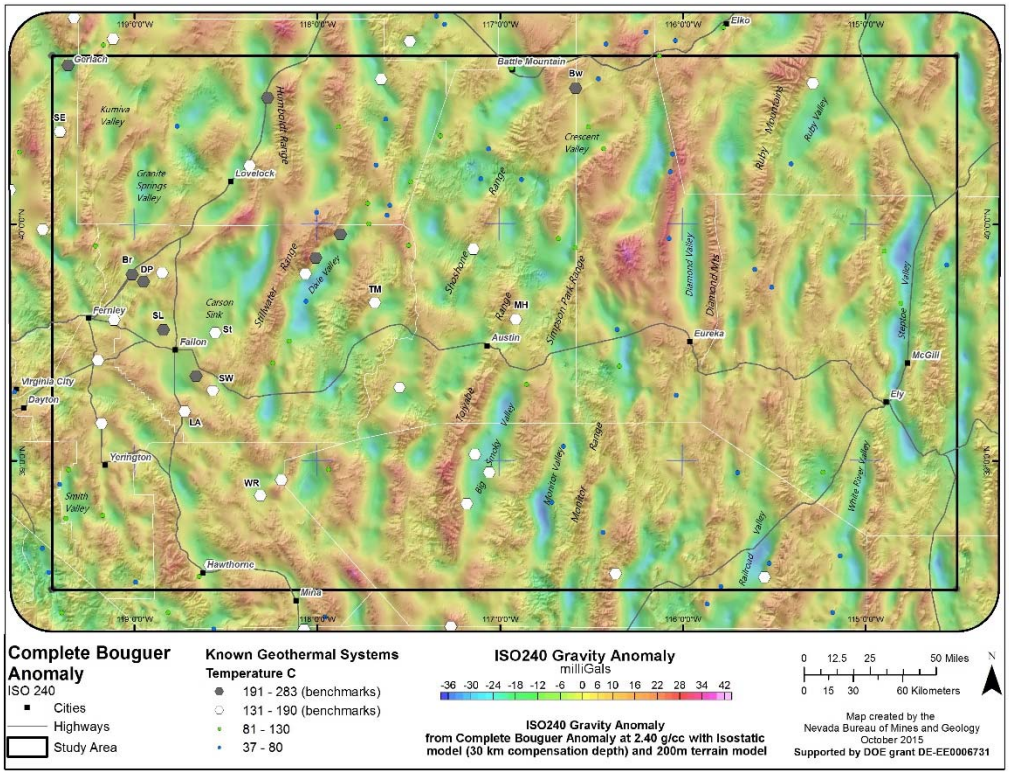

Figure P-12. Complete Bouguer anomaly map for the study area computed at 2.40g/cc.

Subtask 2.3 – Review and Interpretation of Magnetotelluric Data: The purpose of the 3D MT data coverage (Fig. P-13) is to search for existence of low-resistivity upwellings that could signify shallowing heat sources and large-scale permeability. This follows reconnaissance MT surveying in the Great Basin that suggested such features were diagnostic of high-temperature geothermal systems and thus could be used as subregional indicators of geothermal prospectivity (Wannamaker et al., 2007, 2011; Siler et al., 2014).

Co-Investigator Dr. Phil Wannamaker together with post-doctoral researcher Dr. Virginia Maris from the University of Utah/EGI undertook reinversion of large 3D MT data sets over the Dixie Valley and McGinness Hills producing geothermal fields (Fig. 14). They also provided a 3D inversion of a new MT data set over Kumiva Valley to San Emidio in the northwest part of the study area, supported by a separate DOE/GTP contract. The reinversion was performed using a new edge finite element algorithm also developed under DOE/GTP support that can include topography with deformed hexahedral elements and reduces all requisite system matrices using direct solvers (Kordy et al., 2015a, b).

For data sets in the Dixie Valley, McGinness Hills, and Kumiva Valley areas, prominent low-resistivity upwellings that appeared to be rooted to the lower crust were identified. These were cross correlated with zones of possible fault-related permeability identified by the UNR group as part of Task 6. For Dixie Valley and McGinness, producing areas corresponding to MT upwellings and favorable structural settings also appeared to possess soil gas flux and isotopic anomalies indicative of high temperatures and possible magmatic input at depth.

Explanation of Variance: None. However, it was decided in Q1 to de-emphasize data from the Ruby Mountains, as these data lie outside priority subregions of the project area. Also, the limited coverage of MT data across the region (Fig. P-13) restricted applications of the data set in the final modeling.

Deliverables: Files of x-y-z-Rho values in UTM format with WGS84 datum corresponding to the inversion models of the three geothermal systems (Fig. P-14).

Milestones: M2.3.1 was completed in Q2 and 2.3.2 in Q3 (Table P-1).

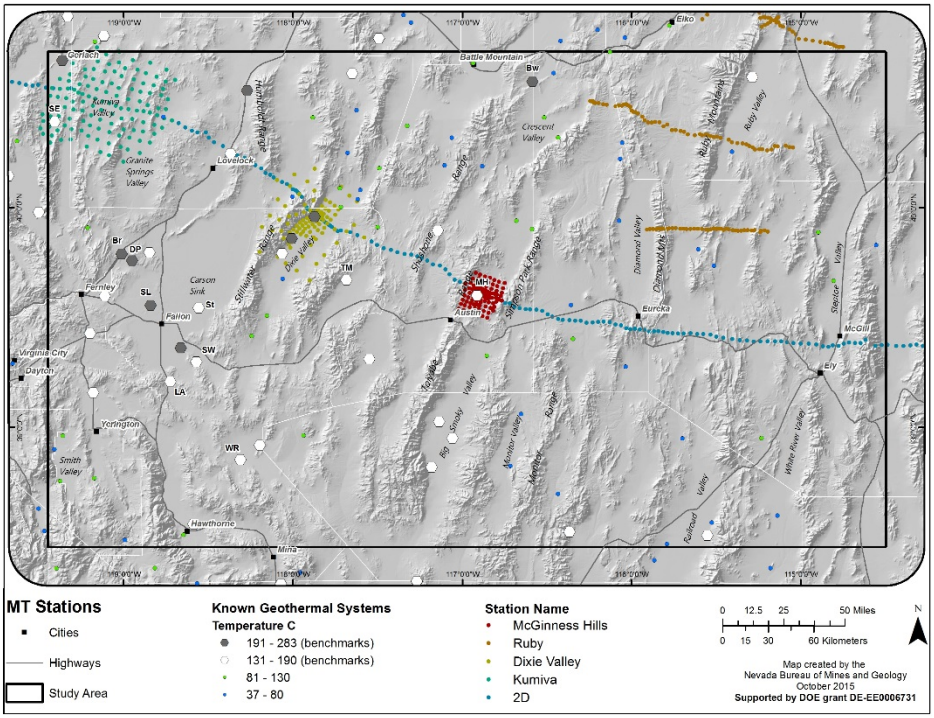

Figure P-13. MT stations within the study area.

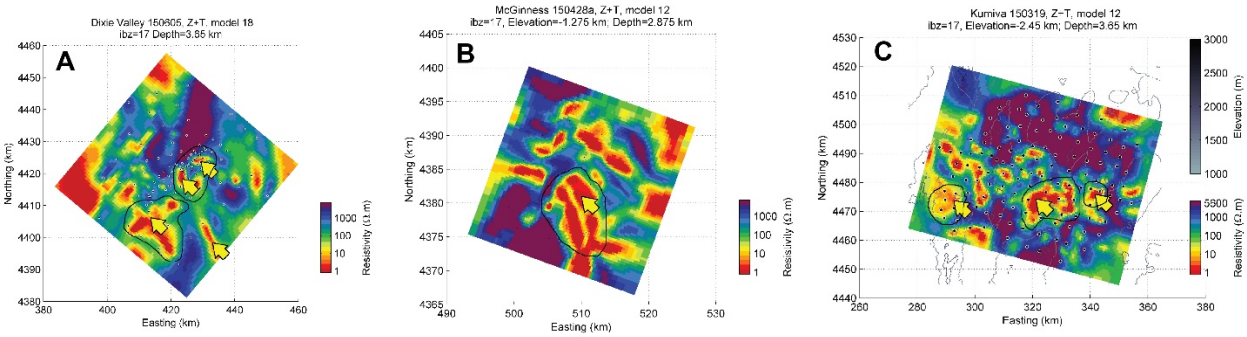

Figure P-14. Resistivity values at various depths for Dixie Valley (A), McGinness Hills (B), and the Kumiva Valley area (C). Kumiva lies in the northwestern part of the study area.

Subtask 2.4 – Review and Interpretation of Seismologic Data: Because regional strain rates are directly related to both seismic and geothermal activity, we inferred that seismic activity can be utilized as a general regional proxy for locating geothermal systems. In addition, favorable structural settings for geothermal systems generally correspond to fault interaction areas, which are critically stressed regions characterized by numerous small to moderate earthquakes in contrast to periodic large earthquakes along the main segments of faults, which tend to periodically relieve stress. Because stress is not relieved by major earthquakes, abundant microseismicity characterizes fault interaction areas, which precludes pervasive healing of fractures and thus facilitates fluid flow. Increased pore-pressure in such areas may also provide a positive feedback mechanism that reduces effective stress and promotes more frequent but lesser magnitude earthquakes (Faulds et al., 2014). These relations suggest that earthquake density may be greater over long intervals in the fault interaction areas and thus could broadly correlate with geothermal activity.

Available seismological data for the study area was compiled using the Nevada earthquake catalogue of Slemmons et al. (1965) for earlier events and the Nevada Seismological Laboratory's catalogue for instrumental events over the past several decades. This was supplemented with additional events from the U.C. Berkeley Seismograph Stations catalogue, University of Utah seismograph stations catalogue, published investigations of individual earthquakes, and historical accounts. One goal of the compilation was to include as many aftershocks and swarm events as possible that were missing from the earlier part of the catalogue.

Seismic networks have expanded through time, and the ability to record and accurately locate lower-magnitude earthquakes has improved dramatically. Thus, the threshold of earthquake magnitudes was established for different time intervals (Table P-2) based on the density and quality of the seismic network for that period. In Q3, a magnitude completeness estimation analysis was thus completed for the recorded earthquakes. Plots were made of earthquakes that occurred during seven different time periods. These time periods were determined by how the earthquakes were recorded, such as from historical accounts versus using local instrumental data. The plots show the number of earthquakes versus their magnitudes and tend to form a linear relationship, whereby the earthquakes of a given magnitude range are "completely" recorded (this is the classic b-value relationship or magnitude-frequency relationship for earthquakes in an area). A minimum magnitude estimate for each time period was then made based on the level at which the number of events falls off of the linear relationship, and events below that magnitude were not used in further analyses of these data. Once the lower earthquake threshold was established for different time intervals, the distribution of earthquakes across the study area was then established (Fig. P-15). In essence, the seismological database summarizes the faulting history in the study area over the past ~150 years, with relatively comprehensive data from only the past several decades.

Even on modern networks, not all earthquakes are recorded, which leads to some uncertainties in earthquake completeness. Earthquake magnitudes are likely estimated within a few tenths of a magnitude outside the seismic network, and more precisely within the network. For instrumental recordings, earthquake locations are likely within 10 km in eastern Nevada and within a few kilometers in western Nevada, where the network is located.

Table P-2. Time Periods and Earthquake Magnitude Completeness Values

Time Period	Lower Threshold Magnitude	Notes
1860s - 1930	M5.5	Historical records
1931 - 1969	M4.5	Regional seismic networks
1970 - 1979	M2.75	Early UNR seismic network
1980 - 1992	M2.25	Increase of instruments in UNR seismic network
1993 – May 9, 2006	M2.0	Addition of southern Nevada network
May 10, 2006 - March 21, 2008	M1.2	EarthScope Bigfoot Array Deployed
March 22, 2008 - Oct. 2014	M1.5	Contemporary NSL network

Explanation of Variance: None.
Deliverables: Map showing contoured density of earthquakes with point data.
Milestones: M 2.4.1 and 2.4.2 were completed in Q2 and Q3, respectively (Table P-1).

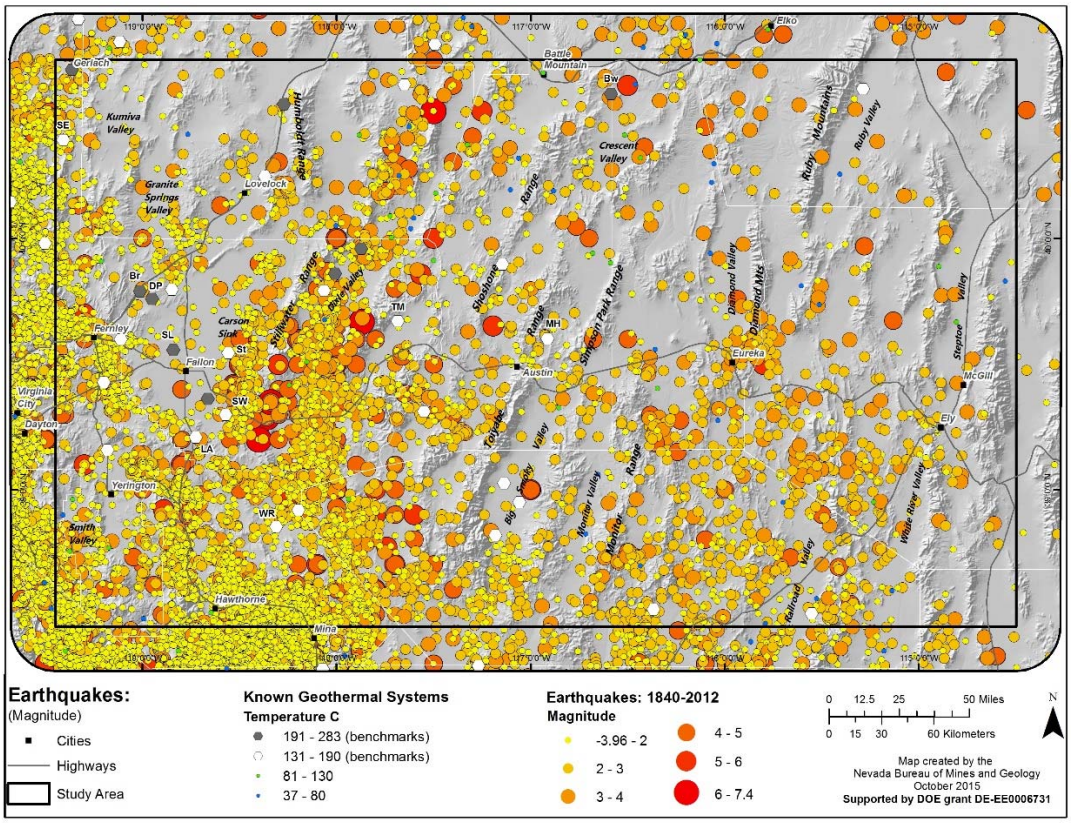

Figure P-15. Earthquake epicenters and magnitude within the study area. See Table P-2 for lower thresholds of earthquakes shown for different time periods

Task 3 – Review and Interpretation of Geochemical Data

The purpose of this task was to compile relevant geochemical data for the study area to help develop favorability rankings based on the constructed play fairway models. Two types of geochemical data were originally slated for compilation to contribute to the assessment of relative productivity of specific structural configurations:

- ***Regional data***: Geochemical data were compiled for the study area from the NV NGDS dataset maintained at NBMG (>40,000 records) and the USGS NWIS database. The compilation included major and trace element and stable isotope fluid data from springs and wells with measured temperatures (Figs. P-16 and P-17).
- ***Site specific data*:** Temporal geochemical, pressure, pumping and temperature data from production, injection, and monitoring wells were to be obtained for the Ormat properties in the study area, such as McGinnis Hills, although Ormat would not provide any non-proprietary data, thus severely limiting our ability to use and present results of any of the data evaluation. Thus, this task could not be completed, as is noted in the project variance section.

Geothermometry: Geochemical data were compiled for spring and well locations within the study area (Figs. P-16 and P-17) and formatted to calculate geothermometers (Figs. P-18 and P-19). All geochemical data were evaluated and categorized for their reliability using charge balances. The focus on regional data included calculation of traditional geothermometers and evaluation of trends in common geothermal pathfinder elements (e.g. B, Li, F) to assess reservoir temperatures and likely distributions.

The primary database used was acquired from NGDS data, which contained USGS National Water Information System (NWIS) data downloaded in 2005. In order to update the NGDS file, NWIS data were downloaded for Nevada on 6/17/15, and the entire download was inserted into the NGDS dataset replacing the older version from 2005. Datasets were each converted to a common coordinate system (UTM NAD 27) and combined into one file, with some duplicates from different datasets removed. Not all duplicate well locations are removed from the dataset due to the excessive time requirements to do so, and it was not necessary given only one representative value (highest temperature, highest quality analysis) would be selected from each grid cell during the modeling.

Charge balances were calculated for all analyses, and all incomplete analyses (e.g., one or only a few chemical constituents) or a charge balance >20% were omitted from the database. However, any record that contained a SiO_2 analysis was retained regardless of charge balance so that silica geothermometers could be calculated for the location. Analyses were sorted by temperature and split into cold (<20°C) and thermal (≥20°C) waters to be evaluated separately. The data were then clipped to the study area in ArcMap, reducing the records to only those located within the study area for the play fairway project (north-central Nevada), plus a 20 km buffer around the study area boundaries. The data were then sorted to remove all samples that were creeks, streams, lakes, or rainwater.

Once the data were reduced to the study area, the analyses were evaluated, and additional records were removed from the data set. Ones that were removed at this stage typically had a good charge balance, but the balance was fortuitous and based on a limited, incomplete analysis, such as an analysis that only reported Na and Cl. Because the charge balances on these samples were misleading, their records were removed from the database.

Estimated subsurface temperatures were calculated using all compiled water analyses using the geothermometers shown in Table P-3. Each geothermometer was calculated in a spreadsheet along with a column for the average of the Na-K-Ca, Mg-corrected and SiO_2-Mariner geothermometer values. The SiO_2-Mariner temperature is based on a threshold in which the quartz geothermometer is used if the Mg-corrected Na-K-Ca temperature is ≥100°C, and the chalcedony temperature is used if this temperature is <100°C.

One representative geothermometer value was selected for each record based on the following criteria. If the record had both SiO_2 and Na-K-Ca, Mg-corrected geothermometers, the average was taken as the geothermometer for that sample. If the record only reported SiO_2 and no cation data, the SiO_2-Gigg geothermometer was selected as the value for that record. When either or both the Na-K-Ca, Mg-corr and SiO_2 geothermometers were lacking or unrealistically low, the K-Mg geothermometer was selected, because the sample was most likely from a lower temperature source for which this geothermometer is preferred. When SiO_2 was either lacking or unrealistically low (e.g., negative numbers), the Na-K-Ca geothermometer was recorded for the record. A column was added to the database spreadsheet noting which geothermometer was selected for any given chemical analysis. A map of these final geothermometry values appears in Figures P-18 and P-19, along with associated plots showing the distribution of chalcedony and Na-K-Ca, Mg-corrected geothermometers available from springs and wells in the study area (Appendix C).

Table P-3. Applied Geothermometers

Geothermometer	Reference
K-Mg	Giggenbach, 1988
Na-K	Giggenbach, 1988
Na-K-Ca	Fournier and Truesdell, 1973
Na-K-Ca, Mg corrected	Fournier and Potter, 1979
Quartz	Fournier, 1981
Chalcedony	Fournier, 1981
Quartz-Adiabatic cooling	Fournier, 1981
SiO2-Gigg	Giggenbach, 1992
SiO2-Mariner	Mariner et al., 1983

Although not included as part of this phase of modeling, geothermometers were also calculated for all available cold waters to provide a first approximation of the location of potentially blind geothermal systems. Shevenell et al. (2012) noted several areas in Nevada with elevated geothermometer temperatures from cold springs associated with blind systems that were later discovered. This data compilation can be used to focus some future exploration efforts into areas with known anomalous geothermometer temperatures from cold waters. Appendix C includes a map of these areas within the study area.

Geothermometer Uncertainty: The geochemical data were then evaluated and categorized for use in the predictive fairway model. Given that the model grid cells may contain more than one chemical analysis from springs and/or wells within the cell, one value needed to be selected to represent the highest quality geothermometer value for each cell. The value obtained for the grid cell was weighted based on the quality of the individual analyses within the cell. In order to weight the various geothermometer calculations, quality factors were assigned to each analysis based on measured temperature, maturity indices, charge balance, and the difference between the Na-K-Ca and Quartz geothermometers. These quality factors provide one measure of uncertainty incorporated into the numerical model discussed in the Task 9 section. Discussion of these factors and weighting of the geochemical data appear in the Task 9 section. Figures showing the distribution of available water chemistry and geothermometry in the study area appear in Appendix C.

Conceptually, quality factors were assigned based on the assumption that the best analyses would have a small charge balance. Springs and wells sampled from higher temperature sources typically are expected to be the best samples, and those with Na-K-Ca geothermometers close to the Quartz geothermometer are considered the most reliable due to the close agreement in temperatures from different estimates (e.g., those using cations vs. those using SiO_2). The maturity index (MI; Giggenbach, 1988) was also considered in assigning a quality to the analyses given that those with MI>2.5 are closest to equilibrium when considering cation concentrations, whereas those <2.5 are increasingly farther from equilibrium, either in the partially equilibrated or immature water categories. Based on these criteria, subjective assignments of quality factors were assigned with 30% of the weighting of the factor being attributed to the factors assigned to each sample temperature and the difference between the Na-K-Ca and Quartz geothermometers. The MI and charge balance were each assigned a 20% weighting factor in estimating the total quality factor for the analysis. The higher weighting given to temperature and the difference in geothermometer temperatures was assigned, because a higher temperature water has likely re-equilibrated less during travel from the reservoir than a cooler water, and the geothermometer difference is suggestive of a good temperature estimate when the two geothermometers are similar, irrespective of the other two factors. The highest QF that could be assigned based on these criteria is 100 based on a summation of the four different criteria used in the quality assessment. Table P-4 shows a summary of the assignment of these quality factors, which were appropriately re-scaled during the modeling portion of the work such that error estimates could be consistent across data types.

The distribution of the data that fall into the different categories noted in Table P-4 are listed in Table P-5. The total number of available analyses from thermal waters in the study area was 962, with relatively few samples (wells) being >120°C (29, or 3%), with the greatest number of samples in the 20 to 40°C range (372, or 39%).

Table P-4. Quality factors assigned to water analyses for use in statistical modeling

Spring Temp (°C)	Quality Factor	SiO_2 Only	Charge Balance	Quality Factor	Qzt vs Na-K-Ca (°C)	Quality Factor	MI	Quality Factor
30%			*20%*		*30%*		*20%*	
>120°C	30	75	≤5%	20	±10°C	30	>2.5	20
>100-120°C	26	65	>5-10%	16	±15°C	24	>2.25-2.5	16
>80-100°C	22	55	>10-15%	12	±20°C	18	2-2.25	12
>60-80°C	18	45	>15-20%	8	>±20°C	12	>1.5-2	5
>40-60°C	14	35	>20%	6	>±40°C	5	>1-1.5	4
>20-40°C	10	25	SiO2 only	5	>±60°C	2	<1	1
<20°C	7	17.5			unknown	6		
unknown	9	22.5						

Table P-5. Number of samples available for each category for which quality factors were assigned

Spring or Well Temp (°C)	**# of samples**	**Charge Balance**	**# of samples**	**Qzt vs Na-K-Ca (°C)**	**# of samples**	**MI**	**# of samples**
30%		20%		30%		20%	
>120°C	29	≤5%	428	±10°C	96	>2.5	76
>100-120°C	13	>5-10%	126	±15°C	39	>2.25-2.5	138
>80-100°C	150	>10-15%	57	±20°C	41	2-2.25	144
>60-80°C	125	>15-20%	25	>±20°C	180	>1.5-2	208
>40-60°C	104	>20%	13	>±40°C	85	>1-1.5	162
>20-40°C	372	SiO2 only	313	>±60°C	196	<1	234
<20°C	2			unknown	325		
unknown	167						
Total	962		962		962		962

Additionally, an initial estimate of probability factors was constructed for the modeling. Table P-6 lists the factors assigned to different measured and geothermometer temperature ranges for both springs and wells in the study area. The factors assigned are based on expert-driven guidance of the ability of a power-capable, >130°C resource to occur, without direct consideration of other factors (e.g., favorable structural setting). These probabilities are combined with the other favorable factor probabilities (e.g., structure probabilities) in the modeling portion of the work.

The factors are not the same for wells and springs of the same temperature range, as a lower temperature spring has likely undergone more cooling compared to water of the same temperature in a well. For example, from Table P-6, a spring between >50-75°C has the same probability of representing a >130°C as a well with temperature between 50 and 100°C (probability of 0.4), with both less than the probability of 0.5 for a well geothermometer indicating reservoir temperatures in the range of 100-130°C. Similarly, a higher geothermometer than measured value is required to obtain the same probability factor. For instance, a well with a measured temperature of 60°C has a probability factor of 0.4, whereas a well with a geothermometer temperature of 60°C would only have a probability factor of 0.1. In this scheme, no site is assumed to have a 100% probability of a >130°C resource, and none have 0% probability.

Table P-6. Probability factors assigned to measured and calculated temperatures (ranges in °C)

Springs	Springs	Springs	Springs	Wells	Wells	Wells	Wells
Measured Temperature	Probability	Geothermom Temperature	Probability	Measured Temperature	Probability	Geothermom Temperature	Probability
<50	0.2	<50	0.2	<50	0.1	<100	0.1
50-75	0.4	50-75	0.4	50-100	0.4	100-130	0.5
>75-90	0.6	>75-100	0.6	>100-130	0.7	>130-200	0.8
>90	0.7	>100-150	0.7	>130	0.9	>200-250	0.85
		>150	0.9			>250	0.9
unknown	0.1	unknown	0.1	unknown	0.1	unknown	0.1

Error Analysis/Estimation:

Geothermometry:

Errors on geochemical analyses and geothermometer estimates were expert-based and data-driven. Errors on all measured temperatures were assigned as ±5%. Error assignment for calculated geothermometers were based on the following criteria, and in consideration of the assigned quality factors for each analysis.

1. No geothermometer was assumed to be in error by >50% or <5%.
2. Errors were estimated in increments of 5%.
3. The difference between the Na-K-Ca and quartz geothermometers was compared to the "best estimate" value of the geothermometer selected based on the considerations discussed in a previous section (% variation). If this value was >50% of the total "best estimate" used in the model, and the quality factor was ≤50, an error of 50% was assigned.
4. If the quality factor was >50, the approximate %error was based on the ratio of the difference of the Na-K-Ca minus quartz over the Best Estimate (% variation).
5. If this % variation was low, but the quality factor was <50, the %error was downgraded from the % variation value by 5%.
6. If either the Na-K-Ca or quartz calculated geothermometers were negative, so that the difference between the two is meaningless, a percent error of 20% was assigned to samples with quality factors >50, and 35% to those with quality factors <50.

Where multiple values are available, the best geothermometer estimate and associated probability and error for each grid cell were selected for use in the numerical model based on the quality factor and estimated % error of an individual analysis.

Well Database – Part of Degree of Exploration Model: A database of all known wells in the study area was also constructed from a variety of sources noted below (Table P-7). This data set includes many more locations than the geochemistry data set, as most wells do not have available chemical analyses, but many have recorded temperatures. This database is primarily used to construct a degree of exploration model in which known temperatures (hot or cold) at deeper levels suggest a greater degree of exploration, and hence a greater degree of confidence for temperatures and geothermometers within a given grid cell. The lack of exploration in areas with other favorable factors (e.g., favorable structural setting) would be suggestive of the greater likelihood of the presence of blind geothermal systems.

Table P-7. Sources of Well Data

Sources of Data	Primary Well Types	Website
NBMG	Oil and Gas	Portions provided by Dave Davis (NMBG) and Shevenell (ATLAS)
NBMG/NDOM	Permitted Geothermal	Portions provided by Dave Davis (NBMG) & Lowell Price (NDOM)
NGDS	Geothermal, water	http://repository.stategeothermaldata.org/repository/resource/a748ce233a25e3e0dd00c9865d3d2492/
NV State Engineer	Water	http://water.nv.gov/mapping/ (well log file bottom of page)
NWIS	Water, observation, research	http://waterdata.usgs.gov/nwis
SMU	Gradient	http://geothermal.smu.edu/static/DownloadFilesButtonPage.htm

The combined dataset was then clipped in ArcMap to the study area with the resulting number of entries from each data set noted in Table P-8. NWIS is listed separately to demonstrate the statistics for the 2015 data, but these numbers are included in the table in the NGDS row. The totals do not include the second listing of the NWIS data.

Table P-8. Number of Entries for Well Data

	Number of Entries							
	Clipped to Project Area	No Temp	No Depth	No Temp & No Depth	Contain Temp	Contain Temp and Depth	% with Temp & Depth	% with Temp
Oil and Gass	1,349	892	221	221	457	457	34%	34%
Permitted Geothermal Wells	1,089	559	343	337	530	524	48%	49%
NGDS*	6,881	5,100	3,037	2,560	1,781	1,303	19%	26%
NV State Engineer	35,535	31,805	437	429	3,729	3,722	10%	10%
NWIS	6,371	5,100	2,768	2,560	1,271	1,063	17%	20%
SMU Gradient Wells	2,409	646	818	479	1,763	1,424	59%	73%
Totals	47,263	39,002	4,856	4,026	8,260	7,430	16%	17%
* Note, includes some wells from other noted databases for data through 2012								
NGDS numbers include NWIS data dowloaded 6/17/15; NWIS numbers not counted twice in totals.								

As can be seen, most of the datasets have <50% of the well records that report both well depth and maximum (or bottom hole) temperatures. The SMU dataset contained the highest percentage (59%) of complete data with both well temperatures and depths. Only 10% of the entries in the Nevada State Engineers database contain both temperature and depth data, as temperature is not routinely reported for these wells, which are typically permitted by the state as water wells. A complete tabulation of the 47,000 records of this dataset encompassing the study area is included in the project database submitted to GDR (both in Excel and shapefile format). A map showing the distribution of these wells also appears in Appendix C.

Explanation of Variance: Ormat would not agree to any relaxation of the NDA supplied to *ATLAS*, which did not allow for disclosure or publication of any information provided by Ormat. Thus, it was not possible for *ATLAS* to fulfill the DOE contract obligations requiring reporting and data submittal and publishing, if Ormat data were evaluated. Discussions were held with the PI (Faulds) and DOE project manager (Holly Thomas), and it was decided that the time allocated to reviewing Ormat data could be better used in other areas of the project. Thus, Shevenell constructed a well database for the study area to be used in the degree of exploration modeling in lieu of evaluating Ormat well records at McGinness Hills and Jersey Valley.

Deliverables: 1) Compilation of available geochemical data for the Great Basin study area completed in Q1. 2) Characterization of geochemical indicators of favorable geothermal settings completed in Q2.

Milestones: M3.1 and M3.2 were completed in Q1 and Q2, respectively (Table P-1).

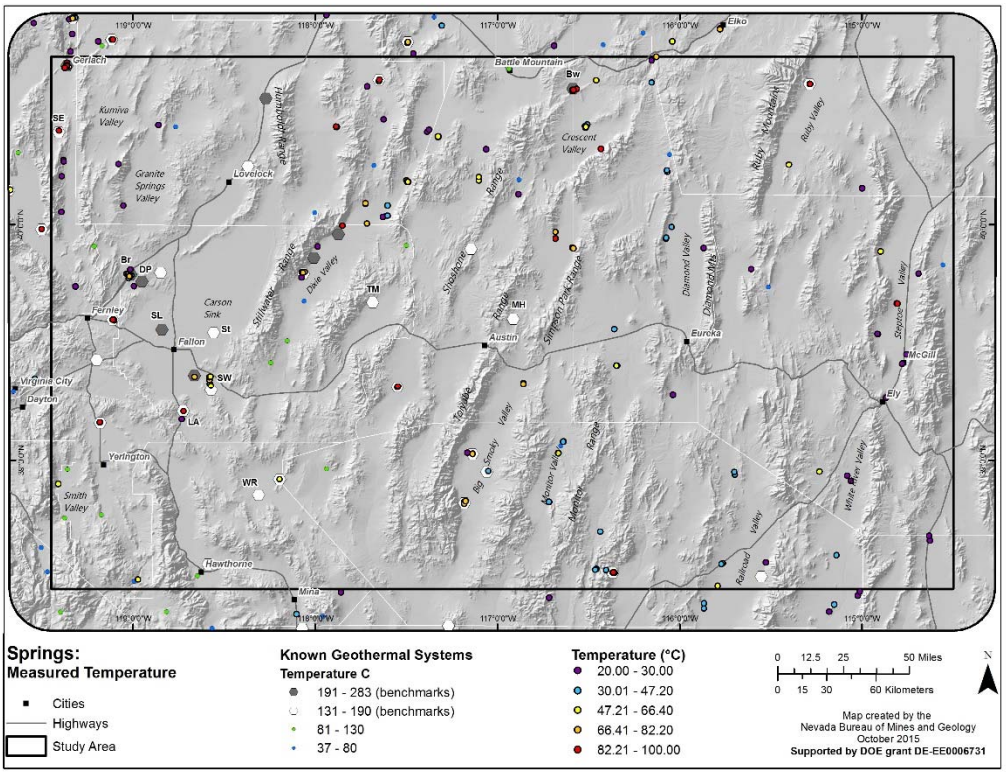

Figure P-16. Measured temperatures from springs within the study area.

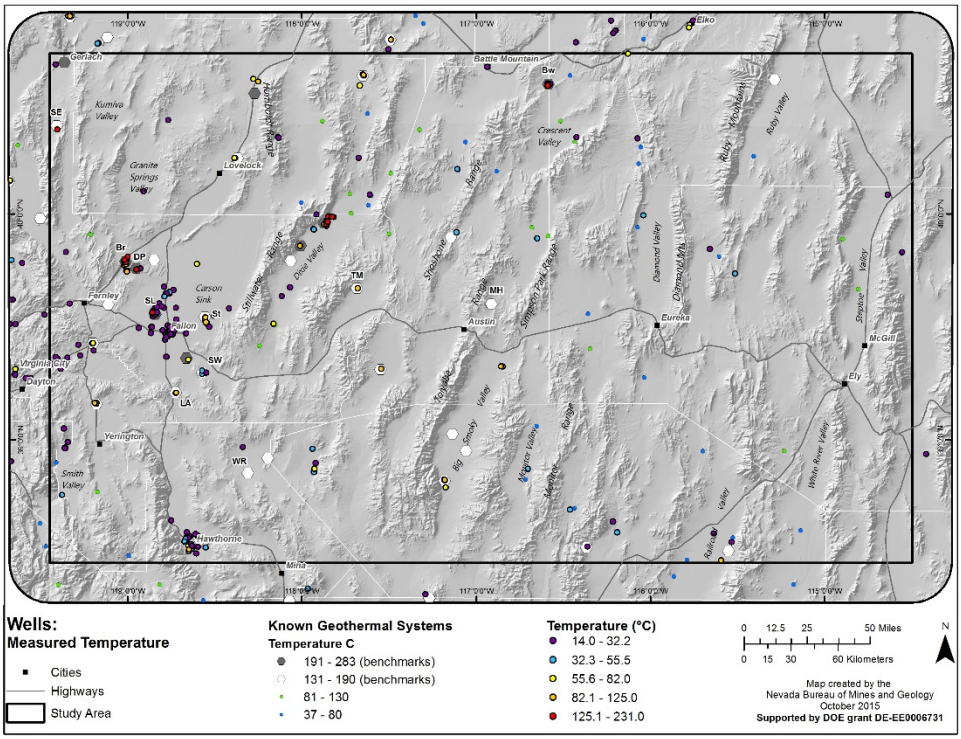

Figure P-17. Measured temperatures from springs within the study area.

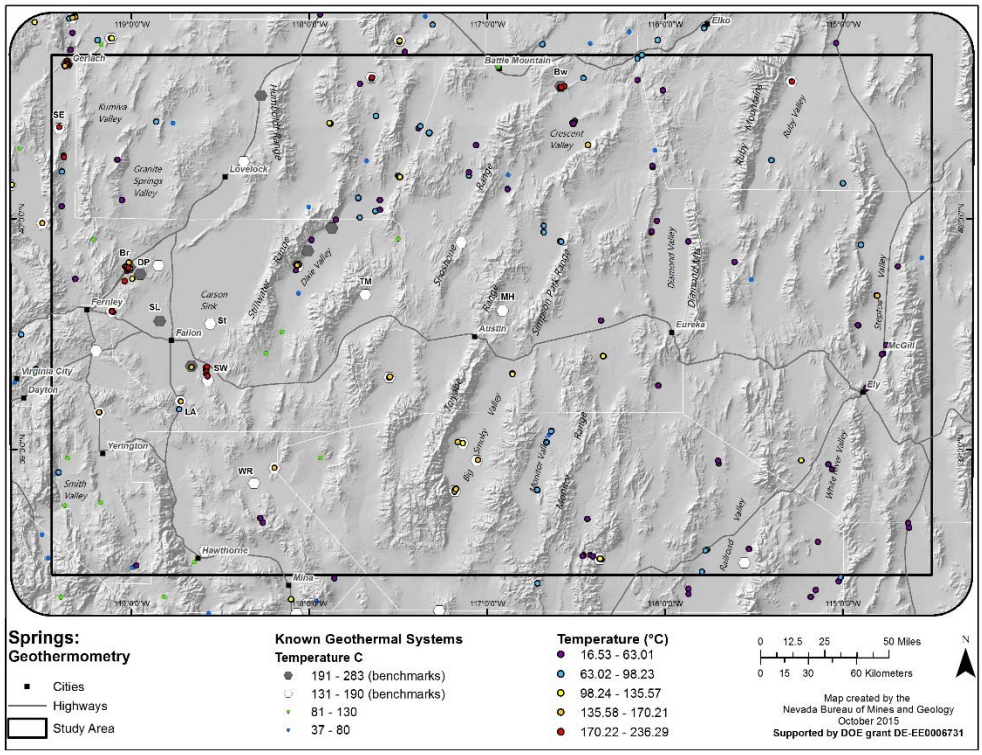

Figure P-18. Geothermometry from springs within the study area.

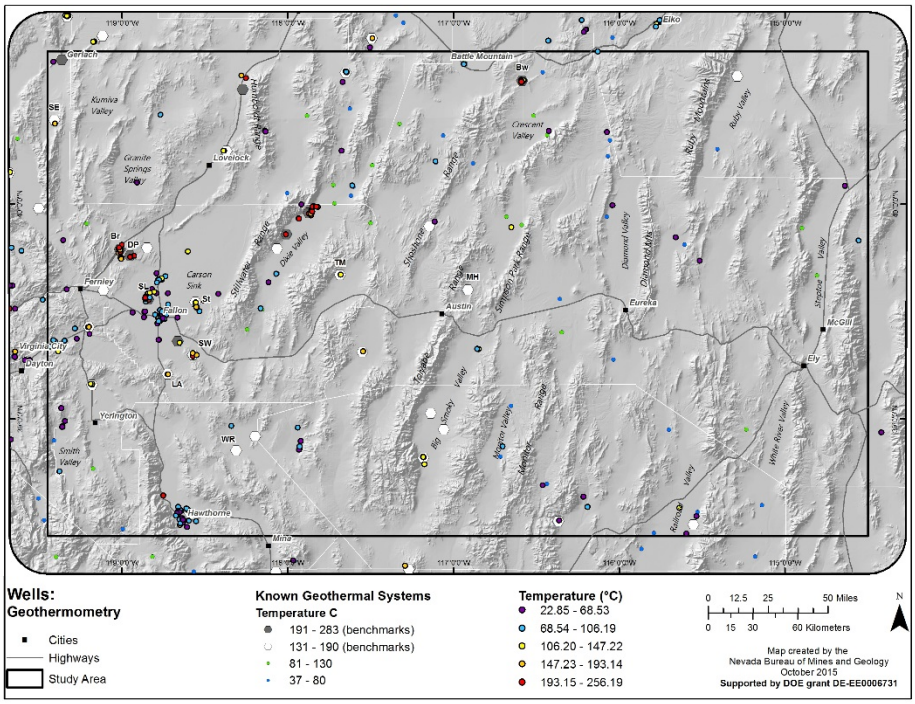

Figure P-19. Geothermometry from wells within the study area.

Task 4 – Review and Interpretation of Geodetic Data

The purpose of this task was to utilize geodesy to measure active tectonic deformation of the crust and provide kinematic control on structural settings that host geothermal systems in the Great Basin. Because better technology and processing techniques are now available, there are better models of crustal deformation and a better understanding of the physical mechanisms behind seismic strain accumulation and release. Strain rate maps depict the intensity of the active deformation and provide control on the transtensional state of stress across individual fault systems that can be compared to other kinds of data, e.g., slip and dilation tendency analysis (Task 7). Together these techniques provide a means to relate active strain rate to favorability for geothermal systems.

NBMG manages a high-precision GPS network called MAGNET, used to quantify the rates, patterns, and style of deformation in the western Great Basin (Blewitt et al., 2009). This network works with other high-precision networks to constrain deformation rates in Nevada to <0.1 mm/yr. Data from GPS networks are integrated in a single processing system in the Nevada Geodetic Laboratory, allowing us to review and interpret all geodetic data in the study area. In essence, the geodetic data provide a snapshot of strain rates over the past ~20 years in contrast to the longer term seismologic (~50-150 years, Task 2.4) and Quaternary fault history (~2.6 Ma, Task 1) of the region.

Major accomplishments in review and analysis of the geodetic data include the following.

- Tensor strain rate data were provided to evaluate the degree to which, in combination with other data, components of the crustal strain rate field predict the presence of geothermal systems. Limitations of the dataset include the uncertainties in the estimates of strain rate, some of which come from the fact that coverage by GPS geodetic networks is uneven and not yet complete across Nevada. Horizontal crustal strain rate was estimated by resolving the components of strain rate in the velocity gradient tensor estimated from the GPS velocity field. The strain rate mapping methodology incorporates a velocity field interpolation based on cubic-spline functions (Kreemer et al., 2000).
- Strain rate maps for the project study area were extracted from the model of Kreemer et al. (2014). These maps (Fig. P-20) include values for strain rate extracted from the model on a grid with spacing of 0.02 degrees for all tensor components, allowing for decomposition of strain rate into shear and dilatational components. These data were provided to test and assess the underlying theory that active crustal deformation is predictive of geothermal favorability.
- The preliminary geodetic strain rate maps were presented to the project team for integrated analysis and combined with other datasets in the favorability modeling. Specific methods of combining the geodetic data with other data types were discussed in detail with the team.
- Strategies for extracting and integrating strain rate values with other variables in the favorability analysis were explored and discussed. It was decided to focus on strain rate parameters in addition to parameters that compare the direction of the principal strain rates to the strike of faulting in a spatially continuous way.
- As the project has progressed, new geodesy-based data files were imagined and conceived as a result of feedback from the broader group. Files with the local azimuth of predicted shear planes from tensor strain rates, tensor strain rate uncertainties, and values for strain rate at all vertices of known active faults were provided to the team for continued analysis.
- Subsequent discussion focused on the need for correcting for earthquake cycle viscoelastic transients in the strain rate field. Hammond provided the predictions of a viscoelastic relaxation model for the central Nevada seismic belt earthquakes (from Hammond et al., 2009), and Kreemer provided a strain rate fields generated both with and without the correction.
- Subsequent integrated favorability analysis of the corrected and non-corrected fields showed that the non-corrected fields (that include the transient part of the relaxation strain rate field) were more effective at predicting the location of the geothermal systems. This suggests that earthquake cycle-related strain is important for targeting geothermal systems.

Explanation of Variance: None.
Deliverables: 1) Compilation of available geodetic data for the Great Basin study area completed in Q1. 2) Characterization of geodetic signatures (e.g. higher strain rates, transtensional strain) of favorable geothermal settings completed in Q4 (Month 10). 3) Velocity and strain rate maps.
Milestones: M4.1 was completed in Q1; M4.2 was finished in Q3; M4.3 was completed in Q4.

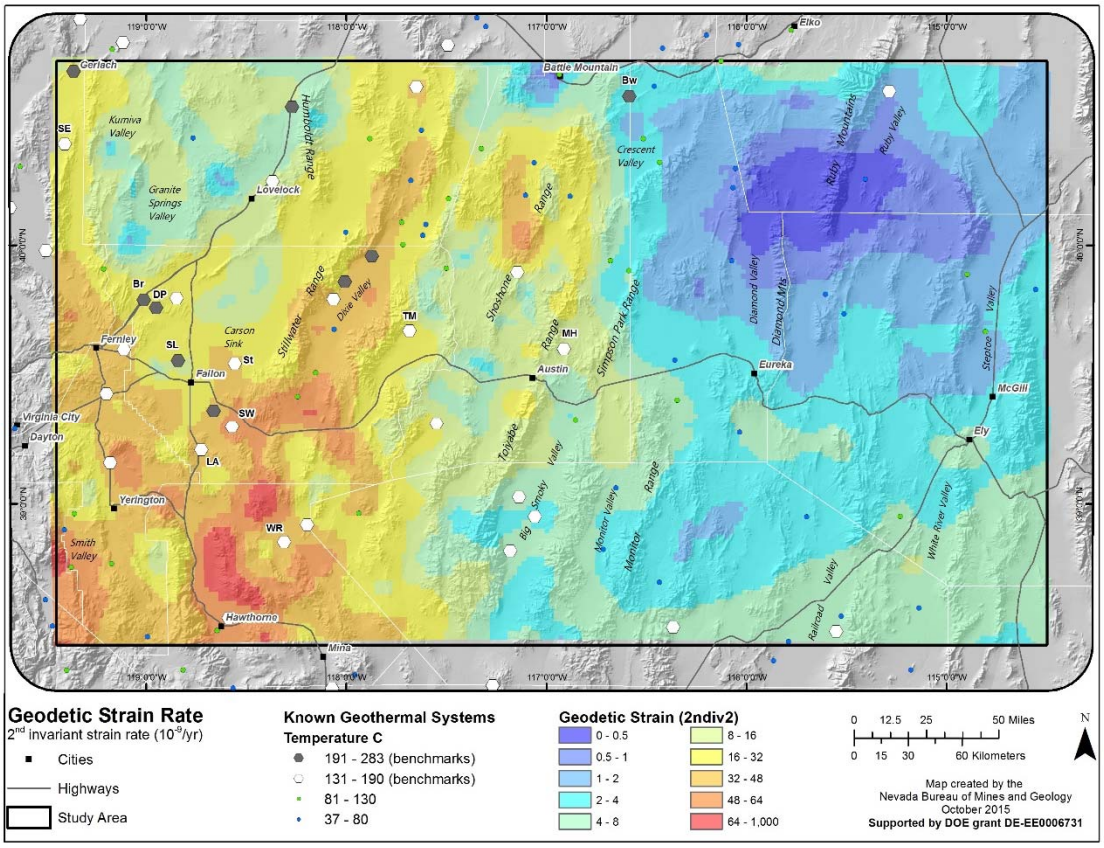

Figure P-20. Transient model of the 2nd invariant of strain rate for the study area. This includes the effects of post-seismic relaxation.

Task 5 – GIS Database Compilation, Preliminary Modeling, Database Management

The purpose of this task was to incorporate the available geologic and geophysical data sets for the study area into one coherent geodatabase. This was accomplished according to the following subtasks.
Subtask 5.1: GIS Database Compilation: Each data set was compiled into a single integrated ArcGIS platform for the study area. ArcGIS provides a central role in data presentation and screening, transferring geo-referenced data to and from other modeling software packages (e.g. 3D Stress for slip-dilation tendency analysis, Geosoft Target for well data, and EarthVision for 3D modeling) used for many of the geostatistical analyses throughout this project. In order to validate the implications of each individual data set, they were cleaned and checked for quality and location accuracy in ArcGIS. Individual data sets are listed in Table P-9.
Explanation of Variance: None
Deliverables: Multiple digital data sets (as listed above) in ArcGIS platform.
Milestones: M5.1 was initially completed in Q2 and finalized in Q4 (Table P-1)

Table P-9. Datasets Produced in Nevada Play Fairways Project

Dataset	Sub dataset
Structural Setting	Type of structure (e.g., fault step-over, accommodation zone)
Quaternary Faults	Recency of faulting
	Slip Rates
Slip Tendency and Dilation Potential	Slip Tendency Analysis of Quaternary Faults
	Dilation Potential Analysis of Quaternary Faults
Gravity	Gravity Station Locations (for use with error analysis)
	Complete Bouguer Anomaly
	Horizontal Gradient
	Thickness of Cenozoic Cover "depth to basement map"
Magnetotelluric (MT)	Station Locations (for sue with error analysis)
	3D resistivity model with multiple depth slices
GPS geodesy	2nd Invariant of the geodetic strain rate
Reflection Seismic Profiles	Reflection Seismic Profiles
Earthquake seismicity	Location, magnitude, and time of events
Wells	Well Temperatures
	Well Geochemistry
Springs	Spring Temperatures
	Spring Geochemistry
Heat	3km depth temperature model
Land Status	Wilderness and wilderness study areas
	Roadless areas
Infrastructure	Power lines
3D Geologic Models	Carson Sink and Steptoe Valley

Subtask 5.2 – Preliminary Modeling: This task involved preliminary predictive modeling and ranking of known and prospective blind geothermal systems in the study area. This was completed at the beginning of Q3 coincidental with the team meeting on April 2-3, 2015. The nature of the initial model was experimental and provided the following: 1) assessment of the completeness and quality of each data set, 2) assessment of the utility of each data set in predicting geothermal potential, and 3) guidance on adjusting remaining workflow tasks to maximize the synergistic potential of the final predictive modeling in Task 9.

In preparation for modeling, ArcGIS grid formats and software functionality were reviewed, and database standards and definitions for the ArcSDM statistical package were prepared. A preliminary predictive geothermal 'fairway' model for the broad study area was assembled in ArcGIS following procedures and methodologies outlined in a series of planning meetings with most of our research team. The preliminary fairway model consisted of the following components, each represented in grid-cell format in ArcGIS and combined using specified weights and mathematical operators (Fig. P-21):

- To guide model construction, benchmarks were derived from the 86 known geothermal systems within the study area. These data were obtained from Faulds and Hinz (2014). Ideally only benchmarks that are or have produced electrical energy would be included, but only 14 such systems are present in the study area, and this number is not a large enough population to be statistically robust. We selected a larger primary set of benchmark geothermal systems based on estimated or measured temperatures >130°C, of which there are 34 known examples in the study area. This 130°C cutoff is useful because based on current binary power plant technology and utility costs, reservoirs >130°C can generally be developed economically, provided they have access to the power market.
- Structural component of permeability model:
    - Ellipses defining structural settings was converted to grid format, and each setting was assigned favorability weights according to the structural classification.

  - A Quaternary fault database shapefile of line segments representing faults was coded and weighted for three parameters: recency of faulting, slip rate, and slip/dilation tendency. The three weighted parameters were then combined into a single index for each fault segment. A 2-km buffer was used to convert the fault line segments into a grid map.
  - The structural setting grid layer was multiplied by a factor of 8 before adding it to the Quaternary fault grid layer to produce a weighted sum 'structural model'.
- Regional-scale permeability model: Three raster layers representing earthquakes, geodetic strain rate, and horizontal gravity gradient comprised the regional-scale permeability model (Fig. P-22).
  - For the earthquake layer, only those earthquakes with magnitudes sufficiently large that they could be detected anywhere in the study area with the array in place at the time of the earthquake were included. A grid layer was created, and within each cell in the model, the total number of earthquakes occurring within a 20 km radius was summed.
  - For the geodetic strain rate layer, an xyz file of the second invariant of strain was provided by the Nevada Geodetic Laboratory and was converted to grid format. That grid was reclassified into a scale from 1 to 7 using an approximate log-normal conversion.
  - The horizontal gravity gradient layer was supplied in grid format and had a scale ranging from 0 to 7.6.
  - After normalizing the range of data for all three regional data layers to similar ranges, they were weighted with the following scheme: 1 for earthquakes, 1.7 for the horizontal gravity gradient, and 1.5 for the strain grid. After each grid was multiplied by its respective weight, the three grids were added together to produce a single weighted-sum regional-scale model.
- Combined permeability model: The regional-scale model grid was then weighted (multiplied) by a factor of 2 before adding it to the structural model grid to produce an overall weighted sum 'combined permeability model'.
- Heat source model: A derivative map representing temperatures at 3 km depth was used for the heat source model. This map was created through collaboration between the SMU Geothermal Laboratory and Great Basin Center for Geothermal Energy ~10 years ago.
- The Fairway grid model: The fairway grid model (Fig. P-23) was created using a scaled linear sum of the combined permeability model and the heat source model. The equation used was: combined permeability model + 3.2 * heat source model. The relative weights were determined from examination of scatter plots revealing the distribution of heat source values and permeability model values throughout the study area, and comparing them to heat source and permeability values where known geothermal systems were present.
- Degree-of-Exploration Model: For the preliminary model, a degree-of-exploration model initially constructed by Coolbaugh et al. (2007) was used. The grid layer contains values ranging from near 0 to near 1, where 0 = no exploration (and no potential for blind systems) and 1 = 100% exploration (any geothermal system, if it exists, would already be found). The degree-of-exploration model included location, type, and depth of wells, depth of the water table, and presence or absence of a regional carbonate aquifer. The degree-of-exploration model was intersected with the fairway model to highlight areas where undiscovered and/or blind geothermal systems are most likely to be found in the study area.
- A team meeting was held to review the preliminary model results and methodology. A field trip was conducted to visit example areas to review the predicted favorabilities. A GRC paper was prepared to document this work (Faulds et al., 2015), and the results were also described at the DOE peer-review meeting in Denver, Colorado.

Explanation of Variance: None.
Deliverables: GRC paper shows results of this preliminary model, which has since been superseded by enhanced data sets and a more rigorous statistically based model, as described below in the *Methodology* and *Results* sections.
Milestones: M5.2 was completed at the beginning of Q3 (Table P-1).

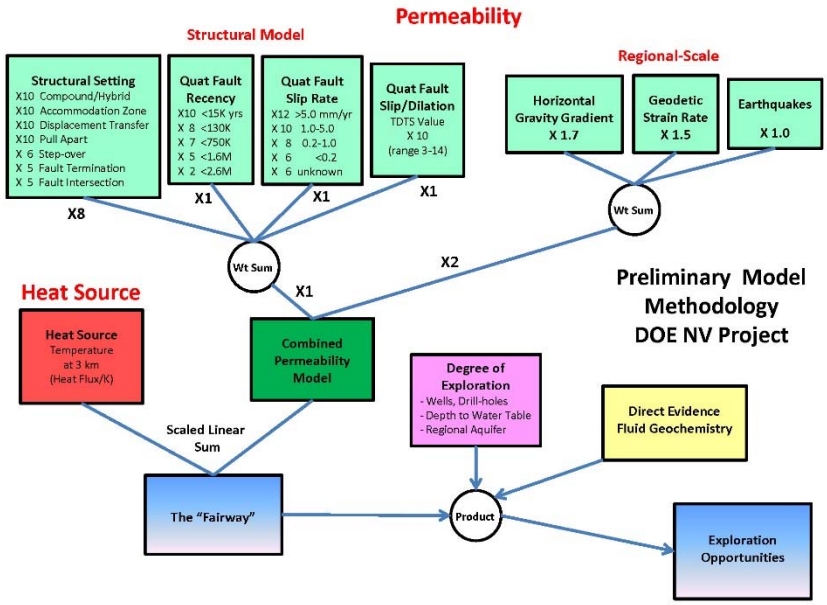

Figure P-21. General methodology and weighting parameters for various components of the preliminary model for this project.

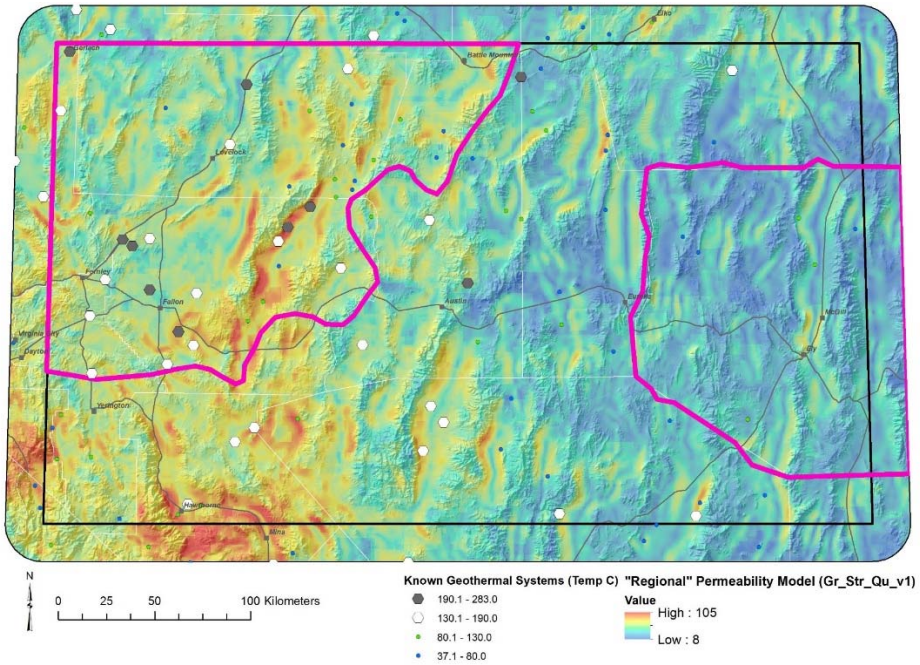

Figure P-22. Preliminary model of regional-scale permeability, incorporating horizontal gravity gradient, geodetic strain rate, and earthquakes. White dots are geothermal systems ≥130ºC. Purple lines correspond to areas for which favorable structural settings had been identified as of March 2015.

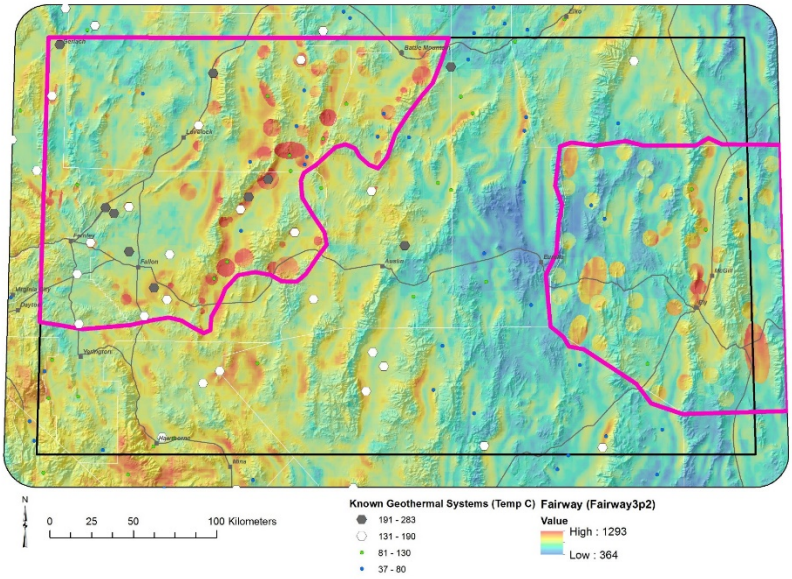

Figure P-23. Preliminary model of the "fairway", incorporating local (structural model) and regional-scale permeability, as shown in Figure P-21, and temperatures at a depth of 3 km. White dots are geothermal systems ≥130ºC. Purple lines correspond to areas for which favorable structural settings had been identified and thus local permeability estimated, as of March 2015.

Subtask 5.3 – Database Management: Data generated in this project has been submitted to DOE-GDR at https://gdr.openei.org. The data was sufficiently complete, in appropriate format acceptable to DOE, and included all files required for an independent analyst to reproduce and verify the work. The data will be made publicly available via the National Geothermal Data System (NGDS) once it has been submitted and accepted into the DOE-GDR system.

Explanation of Variance: We had originally anticipated submitting data sets at the end of each quarter. Because submittal of such data is a time-consuming process and it was critical for this project to complete the data compilation, interpretation, and preliminary model in a timely fashion, we concluded that it is much more prudent to submit data to the DOE-GDR site at the end of Q4 rather than after each quarter.

Deliverables: 1) Individual raw, geospatial capable data files for each data set, including geologic, geophysical, geochemical, and geodetic data. 2) A single ArcGIS MXD for the Great Basin study area with individual layers for geology, geophysics, geochemistry, geodesy, and all predictive modeling layers associated with each part of the workflow. A comprehensive list of individual files submitted to GDR/NGDS is provided in Appendix D. 3) A comprehensive portfolio of all major data layers and models is provided in Appendix E.

Milestones: M5.3 was completed at the end of Q4 (Table P-1).

Task 6 – Identify and Characterize Structural Settings

The purpose of this task was to identify favorable structural settings across the study area and further characterize favorable settings on the basis of the evaluating the compiled geologic and geophysical data. Favorable structural settings are the foundation for assessing local permeability (see Task 9 and Play Fairway Methodology section). Most known geothermal systems in the Great Basin that are associated with specific fault patterns or structural settings. The most common settings include step-overs or relay ramps in normal faults, terminations of major normal faults, fault intersections, and accommodation zones (Faulds et al., 2006, 2011, 2013; Hinz et al., 2008, 2014b; Faulds and Hinz, 2015). These fault interaction areas correspond to long-term critically stressed areas (Sibson, 1996; Curewitz and Karson, 1997). In contrast, the central segments of major normal faults with maximum displacement contain relatively few

geothermal systems. Although each example of a favorable setting does not host a geothermal system, such settings are the most likely prospects for blind, undiscovered systems.

Through evaluation of geologic maps, published papers, fault databases, aerial photos, seismic reflection profiles, and gravity data, we identified ~375 favorable structural settings across within the study area (Figure P-24). The favorable settings cover ~12% of the study area. Each setting is defined by a circle or an ellipse that approximately encompasses the favorable setting (e.g., entire step-over or accommodation zone). We realized while developing this data set that each setting needed to be rated in a complex way, depending on general quality, certainty that it exists, type of setting, recency of Quaternary faulting, Quaternary slip rate, and slip-dilation tendency. In addition, based on feedback from the technical monitoring team, we rated each setting based on its size, as larger geothermal systems and electrical generating potential generally correspond to larger zones of favorable permeability.

Explanation of Variance: None. This task did involve more effort than originally anticipated, but was completed in Q4.

Deliverables: Maps showing favorable structural settings throughout the Great Basin study area were completed in Q3, and relative rankings of each setting were completed in Q4.

Milestones: M6.1 was completed in Q3 (Table P-1) and included maps of the study area showing locations of favorable structural settings.

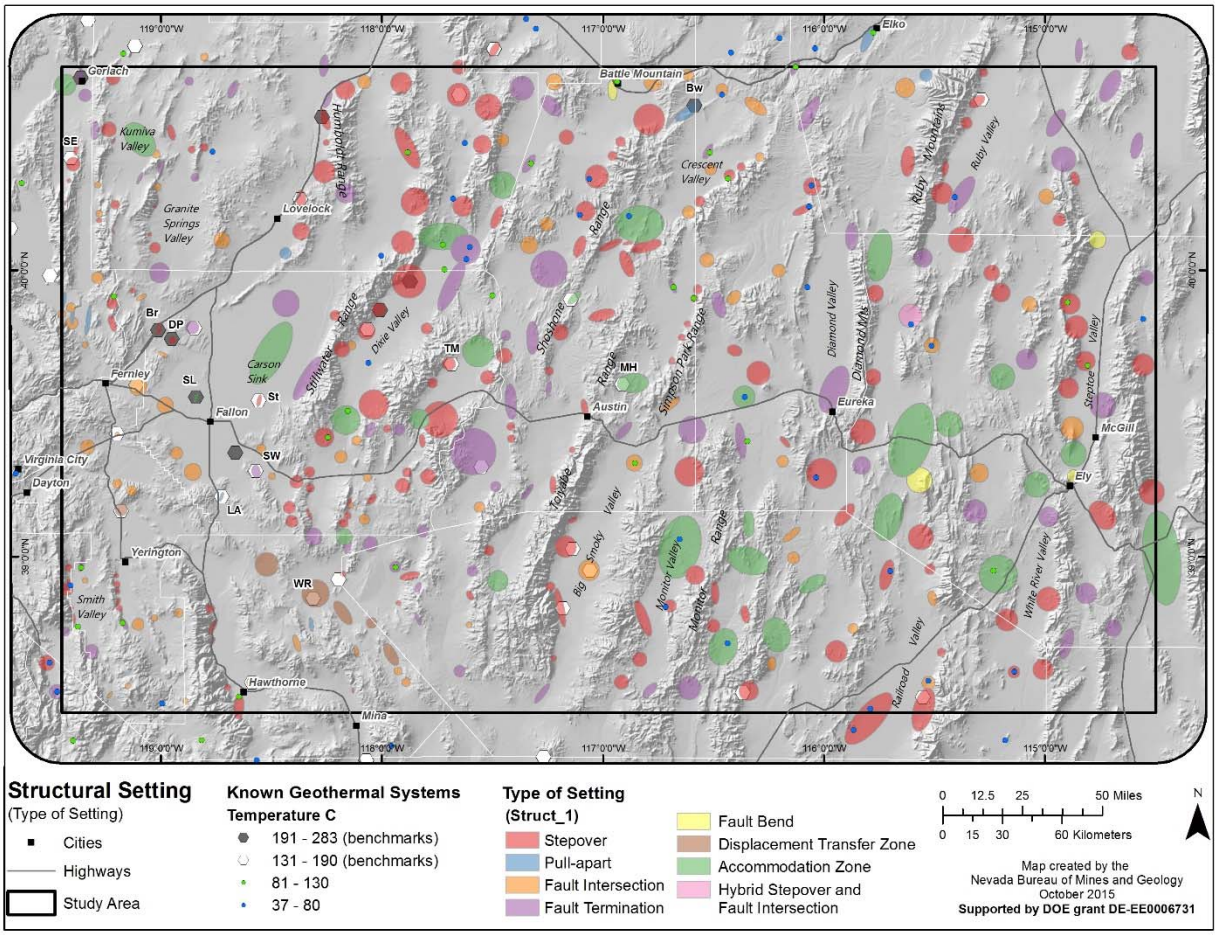

Figure P-24. Favorable structural settings identified in the study area and color coded according to type of setting. About 375 settings were recognized, which incorporate nearly 12% of the area. This includes 174 step-overs, 76 fault terminations, 76 fault intersections, 30 accommodation zones, 9 pull-aparts, 6 displacement transfer zones, and 4 fault bends.

Task 7 – Slip and Dilation Tendency Analysis

The purpose of this task was to assess available stress data in order to determine the tendency of faults in the study area to slip and dilate, which is directly related to the likelihood of such faults to transmit hydrothermal fluids. Critically stressed fault segments have a relatively high likelihood of acting as fluid flow conduits (Sibson, 1996; Barton et al., 1995, 1998; Morris et al., 1996; Ito and Zoback, 2000; Townsend and Zoback, 2000; Zoback and Townsend, 2001). As such, the tendency of a fault segment to slip (slip tendency; T_s) (Morris et al., 1996) or to dilate (dilation tendency; T_d) (Ferrill et al., 1999) provides a quantitative indication of the likelihood of a certain fault segment, relative to another fault segment, to be critically stressed for either slip or dilation, and therefore conduct fluids. The slip tendency of a surface is defined by the ratio of shear stress to normal stress on that surface: $T_s = \tau / \sigma_n$ (Morris et al., 1996). Dilation tendency is defined by the stresses acting normal to a given surface: $T_d = (\sigma_1-\sigma_n) / (\sigma_1-\sigma_3)$ (Ferrill et al., 1999), where τ is the resolved shear stress on the fault plane, σ_n is the resolved normal stress on the fault plane, σ_1 magnitude of the maximum principal stress, and σ_3 is the magnitude of the minimum principal stress. Slip and dilation tendency are both unit-less ratios of the resolved stresses applied to the fault plane by ambient stress conditions. Values range from a maximum of 1, a fault plane ideally oriented to slip or dilate under ambient stress conditions to zero, a fault plane with no potential to slip or dilate. Slip and dilation tendency values were calculated for each Quaternary fault segment within the study area (Figs. P-25 and P-26). As dip is not well constrained or is unknown for many of these faults, it was assumed to be 60° for all normal faults and 90° for strike-slip faults. Though dips can certainly vary, these assumed dip values represent the dips for normal and strike-slip faulting based on simple fault mechanics. While these assumed values, and inaccuracy of the assumed values, will affect the discrete slip and dilation tendency values on a particular fault, by assuming these reasonable values we can examine the *relative* variation in slip and dilation tendency values between different fault segments in the study area. The resulting along-fault and fault-to-fault variation in slip or dilation potential is a proxy for variations in permeability or fluid flow potential.

Azimuthal stress field variation within the study area was approximated based on regional published data and the data from the World Stress Map (Hickman et al., 1998, 2000; Robertson-Tait et al., 2004; Davatzes and Hickman, 2006; Heidbach et al., 2008; Moos and Ronne, 2010; Moeck et al., 2010; Hickman and Davatzes, 2010; Blake and Davatzes, 2011, 2012). We applied either a normal faulting stress regime, where the vertical stress is larger than the maximum horizontal stress, which is larger than the minimum horizontal stress ($S_v > S_{Hmax} > S_{hmin}$) or a strike-slip faulting stress regime, where the maximum horizontal stress is larger than the vertical stress which is larger than the minimum horizontal stress ($S_{Hmax} > S_v > S_{hmin}$). The normal or strike-slip character of the applied stress field was determined based on regional context and analysis of the geometry of each fault segment. Based on visual inspection of the limited stress magnitude data in and proximal to the study area, we used stress magnitudes such that $S_{hmin}/S_{Hmax} = 0.527$ and $S_{hmin}/S_v = 0.46$, which are consistent with complete and partial stress field determinations based on borehole imagery from Desert Peak, the Fallon area, and Dixie valley (Hickman et al., 1998, 2000; Robertson-Tait et al., 2004; Davatzes and Hickman, 2006; Hickman and Davatzes, 2010; Blake and Davatzes, 2011, 2012), all of which lie within the study area.

Twenty stress measurements were available within the study area and were utilized in determination of the stress field acting on fault segments. Of these, eight locations (e.g., Desert Peak, Dixie Valley, NAS Fallon) included calculations of the stress magnitudes of either the complete or partial stress field. For the remaining twelve, only stress orientation data, based on earthquake focal mechanisms, were available. The distance between each fault segment and the nearest of these twenty 'hard' stress values was calculated. This distance was used as a measurement of the uncertainty of the slip and dilation tendency calculations as the stress field acting on fault segments farther from these 'hard' data values is less certain.

In general the minimum horizontal stress direction trends WNW-ESE to NW-SE in the study area. Under these stress conditions normal fault segments striking NNE to NE are best oriented for both slip and dilation, whereas strike-slip fault segments striking WNW and ENE are the best oriented for slip. Because

dilation tendency does not incorporate any shear component, strike-slip faults and normal faults have the same dilation tendency.

Deliverables: 1) Slip and dilation tendency maps of Quaternary faults in the Great Basin study area completed in Q3 (Figs. P-25 and P-26). 2) 3D slip and dilation tendency calculations of faults in the Carson Sink and Steptoe basins completed in Q4.

Milestones: M7.1 was completed in Q3 (Table P-1; maps of the study area showing slip and dilation tendency of Quaternary faults). M7.2 was completed in Q4 (3D slip and dilation tendency calculations of faults in the Carson Sink and Steptoe basins).

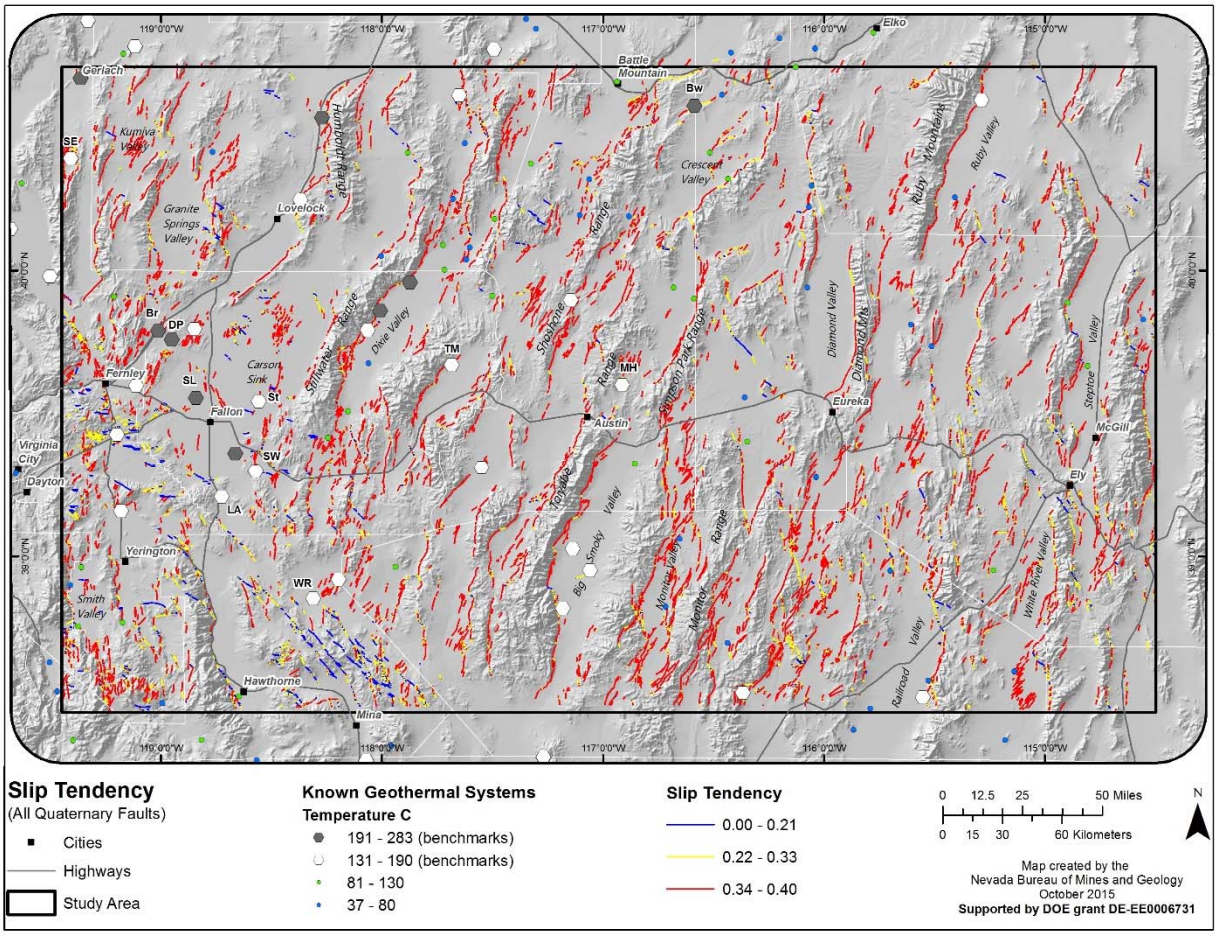

Figure P-25. Slip tendency on all Quaternary faults within the study area.

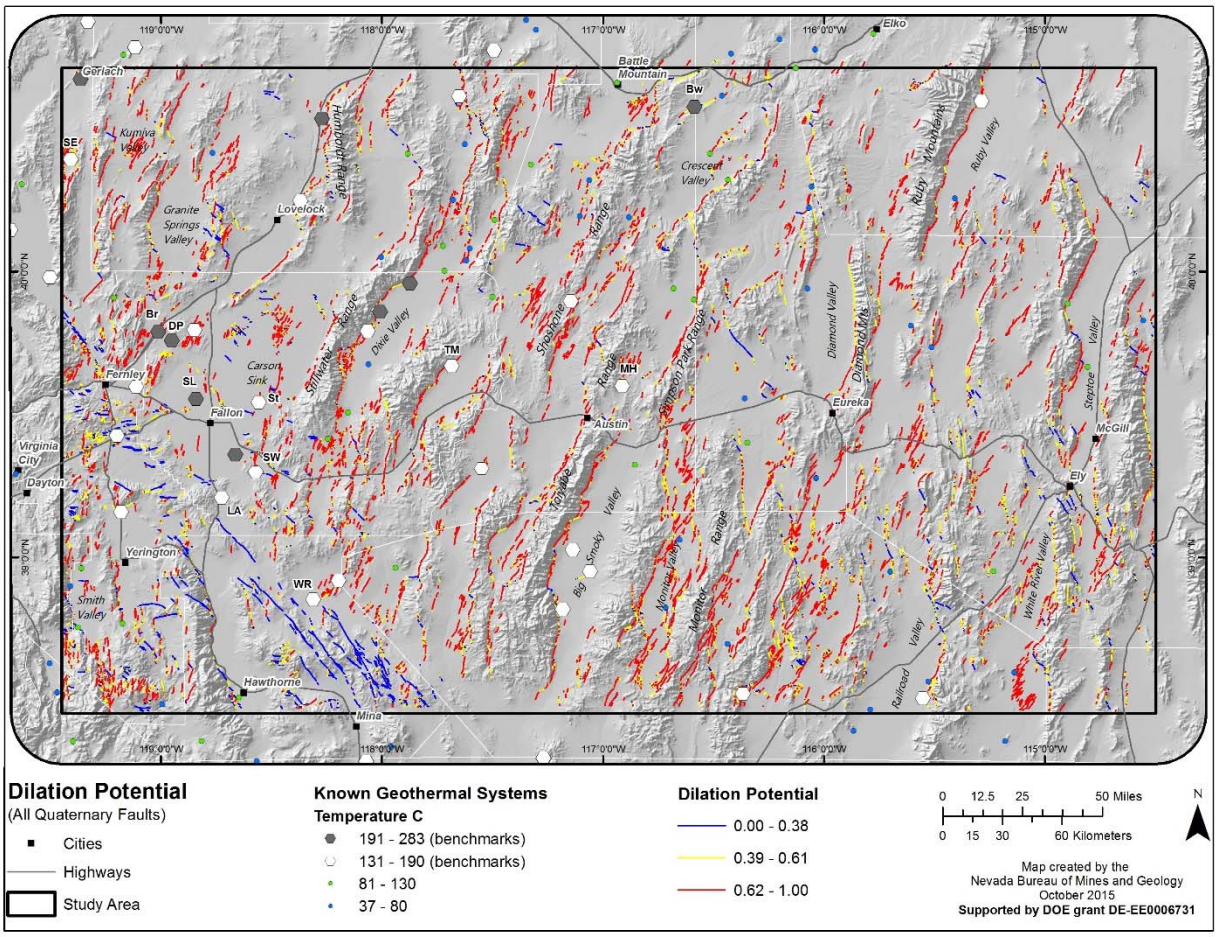

Figure P-26. Dilation tendency of all Quaternary faults within the study area.

Task 8 – 3D Geologic Modeling of Selected Basins

The purpose of this task was to generate 3D models of two large basins (Carson Sink and Steptoe Valley) that have significant geothermal potential. 3D geologic modeling of geothermal prospects is an essential pre-drilling component of the play-fairway exploration technique. In the subsurface, both fault zones and stratigraphic units can be vitally important in controlling geothermal fluid circulation. 3D geologic modeling, where based on sufficient subsurface constraints, can reveal fault and stratigraphic relationships important in defining the locations of geothermal play-fairways in the subsurface and therefore guide subsequent exploration, including drilling.

In the western part of the study area, the Carson Sink was chosen for 3D modeling due to abundant geothermal activity in the area (e.g., Faulds et al., 2010, Hinz et al., 2008, 2013, 2014b; McLachlan et al., 2011), including several operating power plants, significant potential for additional geothermal development from blind geothermal systems (e.g., northern part of Carson Sink), a recently completed detailed gravity survey, and numerous available seismic reflection profiles. The 3D model was developed for the northern part of the Carson Sink due to the denser array of seismic reflection profiles, presence of heretofore unknown favorable structural settings, and relatively unexplored nature of this area. In the eastern part of the study area, Steptoe Valley was selected for 3D modeling based on the presence of several geothermal systems, ample well data, abundant seismic reflection profiles, and studies indicating high geothermal potential in the area (Allis et al., 2013). Our analysis of seismic reflection profiles, available

geologic maps, and well data in the Carson Sink and Steptoe basin has revealed several favorable structural settings hidden beneath the subsurface of these basins.

The 3D structural modeling of the Carson Sink and Steptoe basin has further enhanced our understanding of the structural and stratigraphic framework of the favorable settings hidden beneath these basins, including several fault terminations and a major accommodation zone in the northern part of the Carson Sink and a major step-over in the Steptoe basin (Fig. P-24). We employed established 3D geologic modeling methods (Moeck et al., 2009; Jolie et al., 2012; Siler et al., 2012; Siler and Faulds, 2013) utilizing EarthVision software by Dynamic Graphics, Inc. The 3D structural modeling in the northern Carson Sink was based on interpretation of 14 seismic reflection profiles (Appendix A), lithologic interpretations from 5 wells, a recently completed detailed gravity survey and derivative depth to basement map, and available geologic maps of the area. The 3D structural modeling of Steptoe basin was based on interpretation of 8 seismic reflection profiles (Appendix B), lithologic data from three wells, and available geologic maps. The Carson Sink 3D model incorporates undivided Mesozoic basement, Oligocene rhyolitic ash flow tuffs, Miocene volcanic and lesser sedimentary rocks, and Quaternary basin fill litho-stratigraphic units. The contacts between these units were established based on seismic reflection interpretation, well data, geologic maps and the depth to Mesozoic basement surface. The Steptoe Valley 3D model incorporates undivided Paleozoic basement, Jurassic granitic plutons, Oligo-Miocene volcanic and lesser sedimentary rocks, and Quaternary basement fill units. The contacts between these units at Steptoe were established based on seismic reflection interpretation, well data, regional gravity data, and geologic maps.

Specific pertinent results from the 3D model of the Carson Sink include:

- The geothermal system at Stillwater (Figs. I-2 and P-27A) sits near the northward termination of the Rainbow Mountain fault zone. Stillwater also lies near both a significant change in strike from NNW to NNE in the Rainbow Mountain fault and the intersection of two NNE-striking, W-dipping faults with a WNW-striking, SW-dipping fault. This geometry is relatively well constrained by three local seismic reflection profiles and lithologic interpretations from two wells to ~3000 and ~2000 m depth. This complex area containing, stepping, intersecting, and terminating fault zones is responsible for generating and maintaining permeability at Stillwater.
- The broad accommodation zone in the central part of the northern Carson Sink is a complex area associated with at least twelve major faults, four dipping E or ENE, nine dipping W-NW and one N-dipping fault zone (Fig. P-27B). The most prominent coalescence of these oppositely dipping faults occurs at ~1400 m depth near the top of the Tertiary volcanic section and into the overlying Tertiary and Quaternary sedimentary basin-fill. These fault and litho-stratigraphic geometries are well constrained by four seismic reflection profiles.
- A major left step in the Stillwater range-front fault system transfers displacement basinward from the eastern fault to a buried fault to the west. Down-to-the-west displacement along the eastern fault, which is as much as ~3000 m to the south, steps to the western fault as the basin deepens to ~4200. North of this step-over, the western fault accommodates an increasing fraction of the down-to-the-west displacement, and displacement on the eastern fault decreases to the north. This step-over and the deformation associated with abrupt deepening of the basin may be associated with high density faulting and generation of permeability. The fault and litho-stratigraphic geometries in this area are constrained by one seismic reflection profile, as well as geologic mapping in the Stillwater Range to the east.
- A termination of a W-dipping, NNE-striking fault zone in the northern part of the Carson Sink, as constrained by three profiles (Fig. P-27C). At least four splays of the fault zone die out northward in this area.

Deliverables: Regional 3D models of two basins completed in Q4, incorporating regional 3D models of Carson Sink and Steptoe basins showing faults and stratigraphic units in the subsurface.
Milestones: M 8.1 was completed in Q4 (Table P-1).

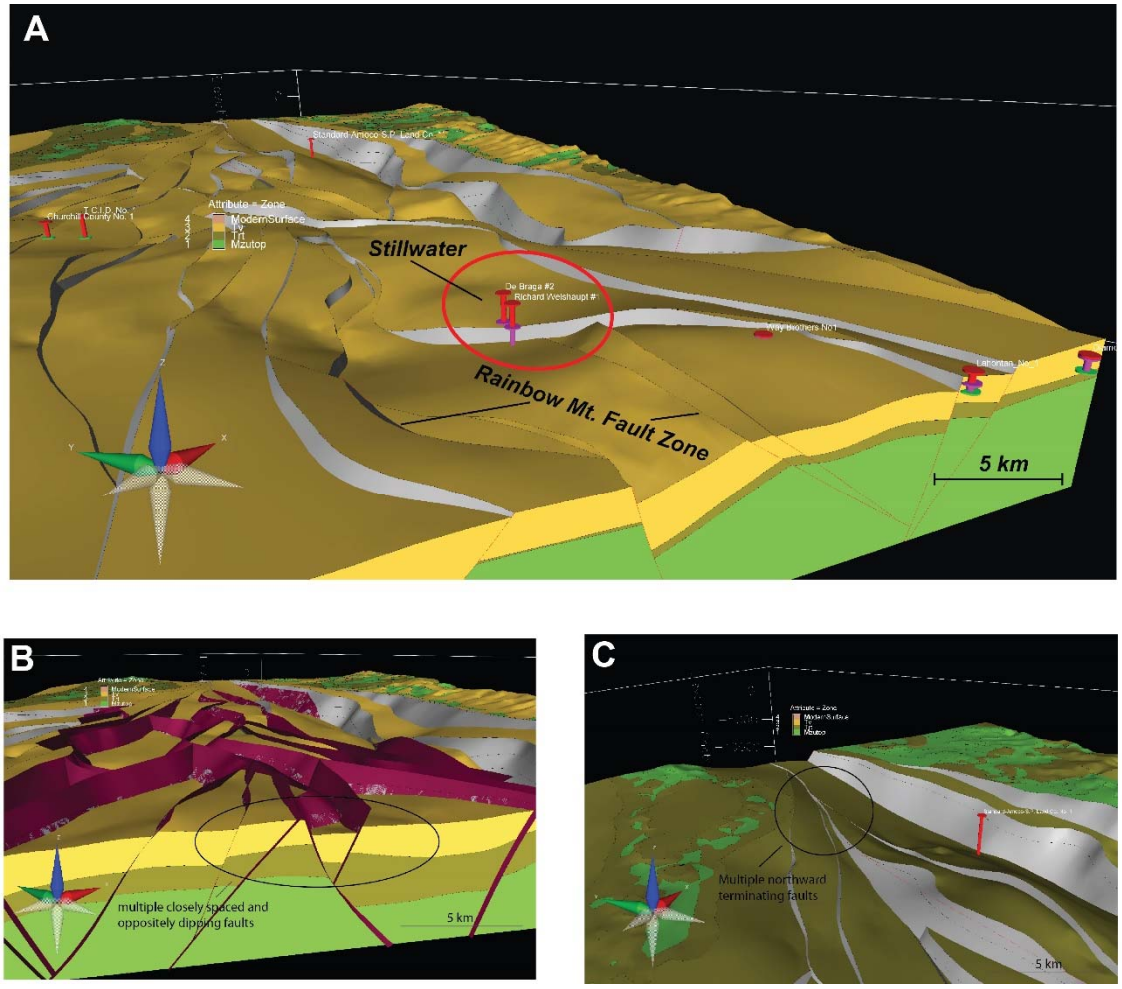

Figure P-27. A. View looking NE at fault systems in the vicinity of the Stillwater geothermal system. Y direction is north, X direction is east. The Stillwater geothermal system lies near De Braga #2 and Richard Weishaupt #1 wells and is controlled by the northward termination of the Rainbow Mountain fault zone and intersections between the Rainbow Mountain fault and NW-striking, W-dipping faults. B. View looking NE at 3D fault geometry of a complex, oppositely dipping fault systems within a major accommodation zone. Y direction is north, X direction is east. C. NE looking view of 3D fault geometry of the northward termination of several normal faults in the same area. Y direction is north, X direction is east. In all views, green lithology is Mesozoic basement, brown Oligocene ash flow tuffs, and yellow Miocene volcanic rocks.

Task 9 – Quantitative Ranking of Blind Geothermal Potential

The purpose of this task was to model the potential for economic geothermal systems within the study area. We provide a brief description here, but a more comprehensive discussion of this analysis and multiple figures illustrating the major components of the modeling are provided in the Methodology section below. The model employed a rating index with input from key hierarchal components necessary for an economic geothermal reservoir (the "play") to form, with permeability (structural control) and temperatures at suitable depths being the major components. The internal composition of these key hierarchal components (i.e. individual evidence layers) and the relative weights assigned to them was determined through a combination of statistical analyses and expert-driven knowledge from our experienced team. For example, based on experience, we assigned different weights to different types of structural settings depending on structural complexity and perceived potential to host geothermal activity. In some areas

where spatial statistics were limited, weighting factors were derived based on the team's experience in the Great Basin, using a fuzzy logic scheme. However, in the case of structure, it was possible in some cases to use more quantitative Bayesian-based weights-of-evidence statistics and logistic regression, scatter plots, and graphs to identify relationships and quantify weights for different input predictive layers based on their known frequency of hosting geothermal systems over broader regions. This is one manner in which statistics helped to quantify the conceptual models. Ultimately, weighted hierarchal layers were combined using the constraints of the fairway play, utilizing a decision tree system and/or statistically supported weights to produce a geothermal potential map. Weights of evidence for all data sets were anchored in analysis of the attributes of 34 benchmarks of known geothermal systems exceeding 130°C scattered across the study area (Fig. I-2).

It was initially planned to estimate the productivity of undiscovered reservoirs. Ultimately measured by produced megawatts, productivity is determined by parameters such as reservoir volume, permeability, and enthalpy, and is influenced by the type of fairway play, temperatures, depths, and size of the predicted favorable region. Industry accepted means of estimating productivity include volumetric heat-in-place methods, Monte Carlo simulations, and detailed numerical modeling. Even though the fairway model described in this report was able to efficiently distinguish potentially productive ground from less prospective ground for geothermal exploration (on the basis of comparison with benchmarks, see Methodology and Results sections), it is not a good predictor of resource size (Fig. P-28). Some constraints are provided by the fact that installed megawatts of production capacity from the 14 producing systems within the study area range from 0.1 to 72 MWe, averaging 28 MWe, but a more precise prediction of resource size remains elusive. Part of the challenge involves the relatively small size of the study area. If the investigation were expanded to cover the entire Great Basin or the western United States, where a larger number of producing systems occur in a greater diversity of geological environments, size patterns would become more definitive.

Finally, the tendency of geothermal systems to remain blind and degree of past exploration was integrated into the modeling to estimate the potential for undiscovered resources. Both the degree-of-exploration (e.g., drilling) and ability of a system to remain blind (e.g., water table depth and presence of impermeable cap rocks) vary highly throughout the study area. Relevant factors for blind geothermal resources that were incorporated into our modeling include: 1) presence of cap rocks (e.g. clay-rich sediments), 2) shallow cold aquifers, and 3) groundwater depth, as evaluated with geologic, well, hydrologic, and geophysical data. Methodology introduced by Coolbaugh et al. (2007) provided a framework for estimating these parameters with fuzzy logic methods and integrating them into probabilistic fairway predictions.

Deliverables: Databases containing rankings and a preliminary map showing contoured geothermal potential.

Milestones: M9.1 was completed in Q4 (Table P-1).

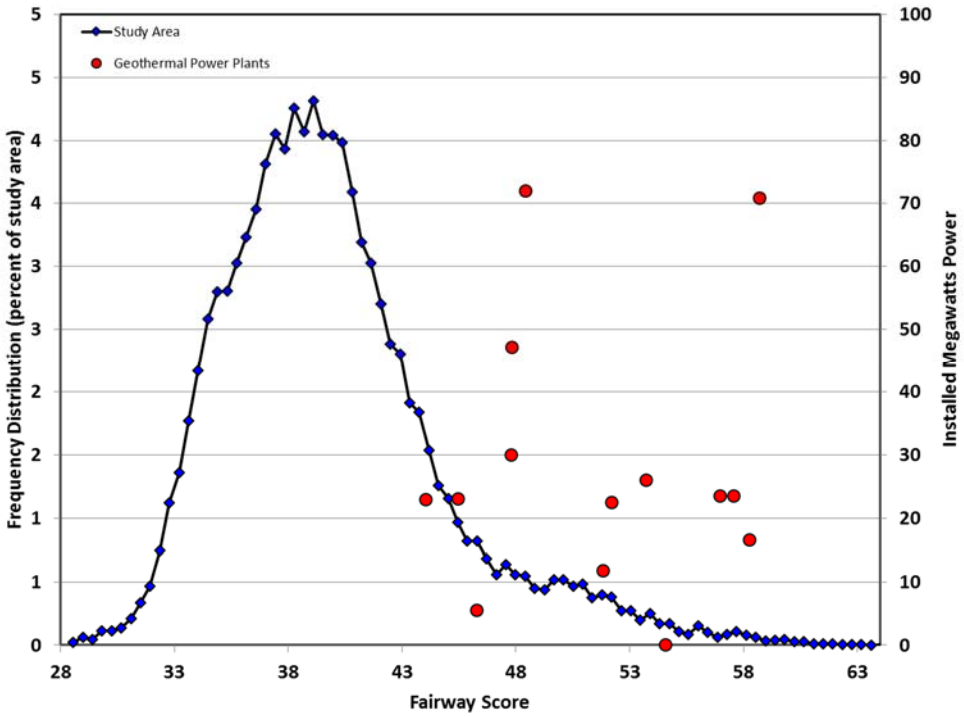

Figure P-28. Distribution of play fairway scores for the study area as a whole relative to those for systems with operating power plants, with installed capacity of power plants also shown.

Task 10 – Construct Geothermal Potential Maps of Study Area

The purpose of this task was to incorporate the Task 9 results to provide integrated, scaled geothermal potential maps of the study area along with clearly defined parameters. The maps define fairways for blind or undiscovered geothermal systems. Specifically, maps were produced for local, intermediate, and regional permeability. The permeability models were then combined with heat to produce a "fairway" map. The "fairway" map was combined with direct evidence from fluid geochemistry to generate an overall favorability map, which in turn was synthesized with degree of exploration to produce an exploration opportunities map. Construction of these maps is described in detail in the Methodology section below. Implications are then discussed in the Results and Discussion section.

Deliverables: Detailed statistically-based geothermal potential maps for the Great Basin study area completed in Q4, incorporating ~10 parameters.

Milestones: M10.1 was completed in Q4 (Table P-1; detailed geothermal potential maps).

Task 11 – Identify Data Needs for Phase II

The purpose of this task was to evaluate the detailed geothermal potential map (Task 1) and select the most promising areas for geothermal development, taking into account land-use status of those areas with high geothermal potential. Areas with the highest geothermal potential and favorable land-use status will then be recommended for detailed studies in Phase II. The selection process and description of proposed Phase II activities is described in detail below in the *Recommendations for Future Exploration* section. Ormat Nevada, Inc., has indicated interest in participating later phases of this project, as evident by an attached support letter (Appendix F).

Deliverables: 1) List of most prospective areas for undiscovered blind geothermal systems for further study completed. 2) Phase II preliminary proposal.

Milestones: M11.1 was completed in Q4 (Table P-1).

Task 12 – Final Reporting and Project Review

The purpose of this task was to synthesize all results into a final report. The final report describes Phase I activities and results, containing all deliverables with contributions from all team members. All databases, publications, and maps were uploaded to the DOE-GDR during October 2015. An important derivative of the final report will be a publication devoted to taking stock of lessons learned in applying geothermal play fairway analysis, with emphasis on advancing this discipline to a robust level, as in the petroleum industry. This contribution will describe what worked and did not work, while also noting data gaps and research and development needs, essentially representing a condensed version of this report.
Deliverables: Final report, with illustrations and databases of Phase I activities and results.
Milestones: M12.1 was completed in Q4 (Table P-1).

METHODOLOGY – PLAY FAIRWAY ANALYSIS

For the play fairway analysis of the broad transect across the Great Basin of Nevada, we developed an expert-guided, fuzzy logic system (e.g., Dixie Valley; Iovenitti et al., 2012) guided and constrained by spatial statistics, including weights-of-evidence and logistic regression. The model integrated each input data set that we carefully selected for this project into two key hierarchal components considered necessary for an economic geothermal reservoir (the "play") to form: 1) permeability and 2) heat. As adequate fluids are generally present in the subsurface in the Great Basin, a third fluid component was not utilized. The major contributing sections in this fairway model include: 1) regional permeability (regional strain and stress), 2) intermediate-scale permeability (entire distribution of Quaternary faults), 3) local permeability (favorable structural settings), and 4) availability of heat (Figs. I-4 and M-1). In addition, direct evidence from fluid geochemistry and degree of exploration, which incorporates well data, depth to water table, and regional aquifers, were integrated to better define exploration opportunities.

A major aspect of developing the play fairway model was determining the composition of the key hierarchal components (i.e., individual evidence layers) and the relative weights assigned to each both within and between each parameter. The determination of weights was aided by establishing benchmarks based on known geothermal activity and using weights-of-evidence and logistic regression to define weights based on spatial correlations. In the sections below, we first describe our selection of benchmarks and then progress through the workflow of analyzing each data set from data input, to initial data set modeling (e.g. interpolation), to statistical evaluation against benchmarks, to selection of weighting values for the play fairway model, and error analysis. We develop the play fairway model beginning at the finer scale (local permeability) and progressing to the broader scale (regional permeability). We view the local permeability as the most critical component of the fairway model in the Great Basin region, because the geothermal gradient and regional setting are generally conducive for geothermal activity throughout the region. Thus, the most critical variable is local permeability as dictated primarily by the makeup of the local structural setting.

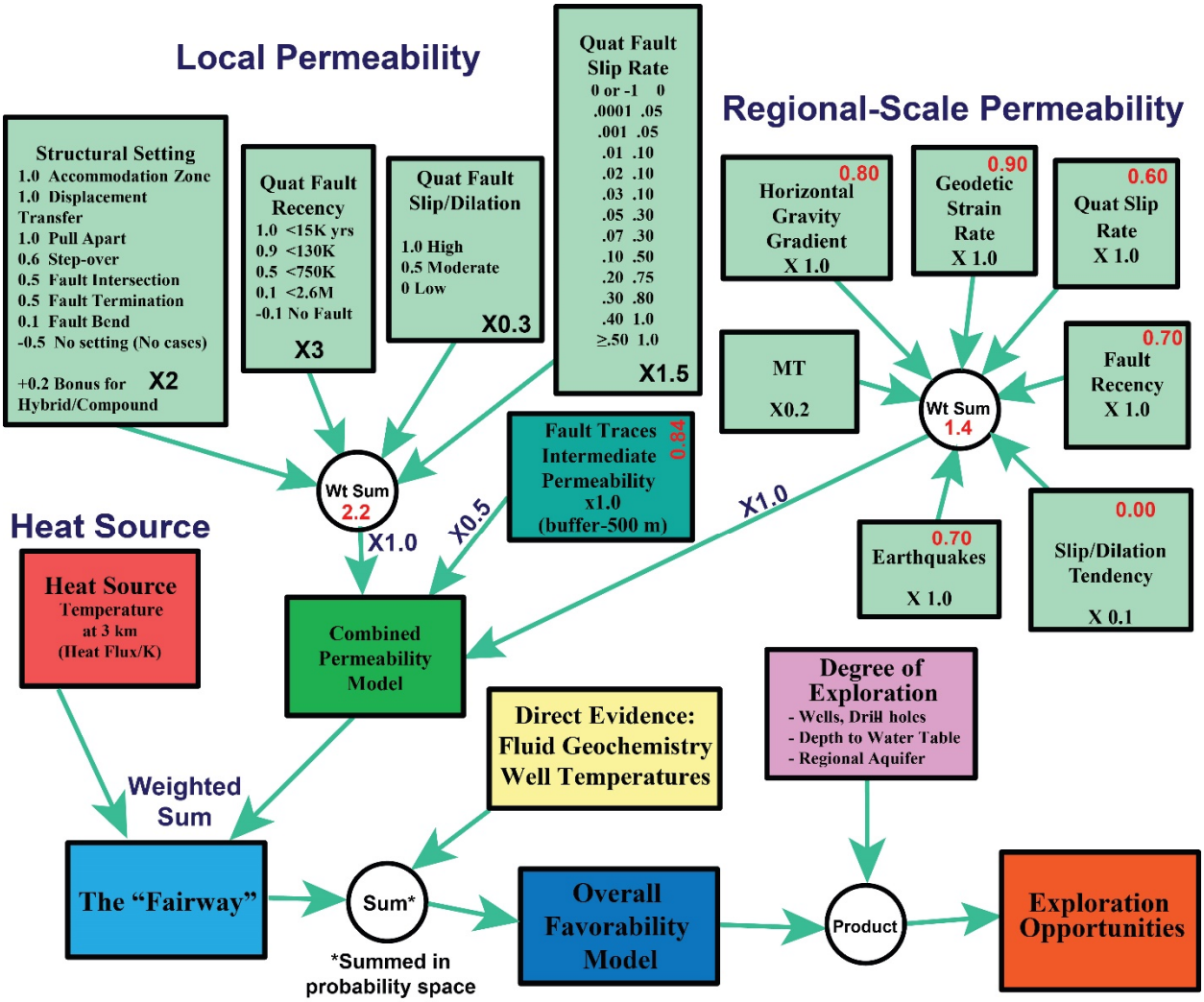

Figure M-1. Nevada play fairway modeling workflow. Red numbers indicate relative weights determined from weights of evidence. Black numbers indicate expert driven weights used in the analysis. In all cases, the expert driven weights took into account the statistical analyses.

Software tools used for data exploration, statistical analysis, and visual observations include:

1) Excel spreadsheets: used for data organization, unit conversion, weight assignments, graphical analysis, scatter plots.

2) Systat: used for logistic regression analysis.

3) ArcGIS: visualization of digital data on maps and mathematical combination of map data to produce predictive maps.

4) ArcSDM add-on extension in ArcGIS for calculation of Bayesian-based weights of evidence and some buffer analyses.

A detailed log of ArcGIS and ArcSDM operations completed for the project is available (Appendix G).

Benchmarks

To guide model construction, benchmarks were derived from the 86 known geothermal systems within the study area (Task 5.2; Fig. M-2, Table M-1). Ideally only benchmarks that are or have produced electrical energy would be included, but only 14 such systems are present in the study area and this number is not a large enough population to be statistically robust. We selected a larger primary set of benchmark geothermal systems based on estimated or measured temperatures >130°C, of which there are 34 known examples in the study area. This 130°C cutoff is useful because based on current binary power plant technology and utility costs, reservoirs >130°C can generally be developed economically, provided they have access to the power market. In addition to the primary >130°C benchmarks, additional sets of benchmarks were used to assess correlations with geothermal systems ranked by temperature across a broader range than just the >130°C. A total of six benchmark categories were used as follows:

Primary Benchmarks:

- Combined "high-medium temperature" systems (>130°C, number = 34). This final set of benchmarks constitutes the primary benchmarks used for determining statistically based weights in this study.

Additional Benchmarks:

- Power-generating geothermal systems (number = 14)
- "High temperature" geothermal systems (>170°, number = 17)
- "Medium temperature" geothermal systems (130-170°C, number = 17)
- "Low temperature" geothermal systems (80-130°C, number = 25)
- "Very low temperature" geothermal systems (37-80°C, number = 27)

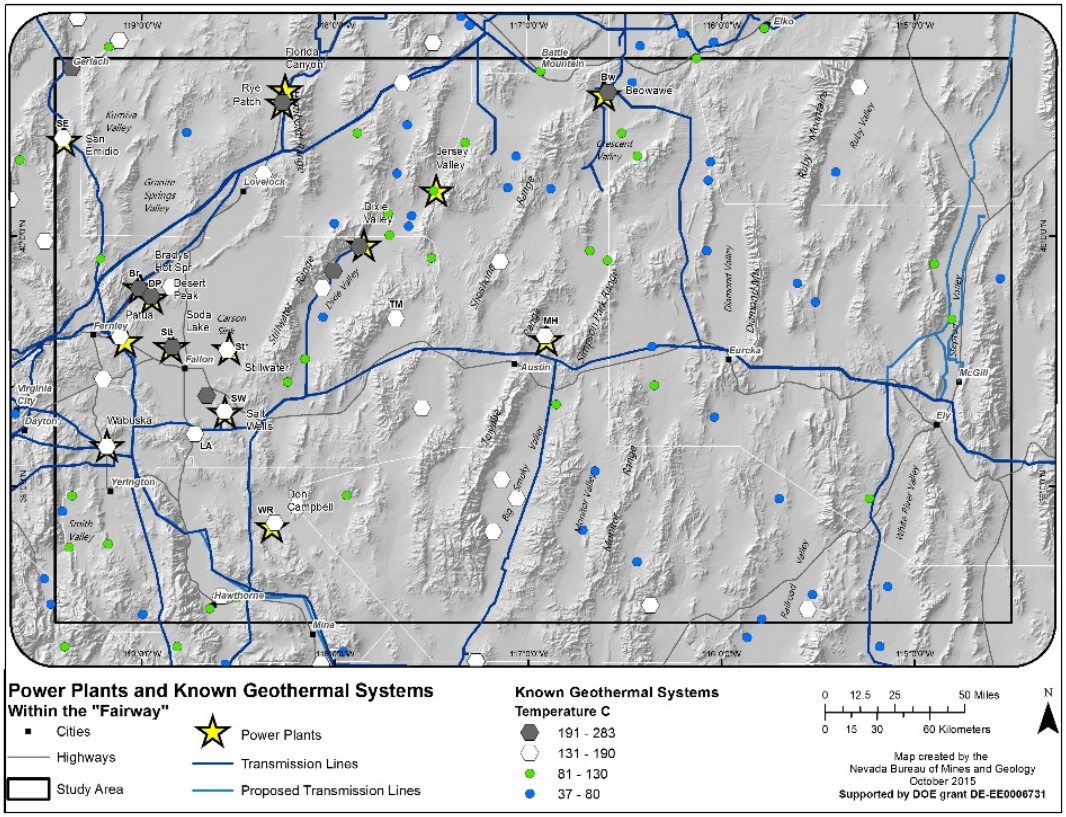

Figure M-2. Map of the 86 total benchmarks, including the 4 temperature groups and the power producing group.

Table M-1. Categories and Values for Benchmarks (≥130°C)

NAME	T (C)	GT (C)	Blind	STR	Power (MWe	Strain Rate (2nd Inv)	Log 10 Recency	Log 10 Slip Rate	TSTD	HG	EQ Index	Temp 3km	Combined Perm.	Fairway	Favorability
Dixie Valley	250	235	no	2	71	35.67	1.53	-1.49	1.03	4.68	156	138	42.45	58.69	0.99
Beowawe	216	227	no	9	17	3.00	1.23	-1.20	0.88	0.08	24	150	40.67	58.24	0.99
Humboldt House	205	224	yes	1	0	8.41	1.39	-1.79	1.02	3.07	11	154	36.44	54.55	0.99
Desert Peak	213	219	yes	2	23	20.33	2.47	-2.71	1.05	0.58	15	134	28.24	44.04	0.90
Soda Lake	216	213	yes	3	23	17.31	1.82	-2.95	0.93	0.21	22	132	29.89	45.45	0.96
Bradys	212	193	no	3	26	21.82	2.39	-2.55	1.06	1.83	18	132	38.20	53.72	0.99
Dixie Comstock	196	139	no	2	0	32.35	1.22	-1.63	0.99	5.86	113	126	43.80	58.58	0.99
Gerlach	131	192	no	1	0	17.36	1.93	-1.32	1.08	3.49	81	132	39.36	54.93	0.99
McGinness Hills	88	192	yes	3	72	12.15	2.29	-2.48	1.03	1.44	33	138	32.24	48.41	0.93
Carson Lake	191	0	yes	10	0	38.79	1.30	-2.61	0.89	2.50	86	147	27.19	44.48	0.89
Empire - San Emidio	148	190	no	2	12	25.56	1.69	-2.66	0.98	3.26	141	137	35.78	51.82	0.99
Salt Wells	177	188	no	3	24	52.47	1.41	-2.39	0.96	1.82	131	133	41.91	57.56	0.99
Sulphur Hot Springs	136	182	no	2	0	1.30	1.21	-0.58	1.05	3.09	4	168	37.99	57.70	0.99
Patua Hot Springs	135	182	no	8	30	44.15	2.22	-2.68	0.92	1.99	82	118	33.92	47.79	0.97
Stillwater	178	169	yes	3	47	35.07	1.38	-2.59	0.92	0.54	118	124	33.19	47.81	0.95
Tungsten Mtn	97	176	yes	2	0	23.50	2.12	-1.48	0.95	3.24	16	127	40.55	55.48	0.98
Lee-Allen	95	171	no	9	0	35.21	2.12	-2.39	0.75	1.75	55	138	34.20	50.45	0.98
Leach Hot Springs	132	169	no	7	0	33.09	2.10	-1.85	0.90	3.20	31	142	40.47	57.19	0.99
Jersey Valley	91	130	no	2	24	16.35	2.02	-2.26	0.96	3.24	28	150	39.37	56.97	0.98
Hot Creek Ranch	82	160	no	2	0	5.05	2.72	-2.75	0.99	2.60	108	120	34.68	48.75	0.98
Colado	155	149	yes	2	0	10.64	1.69	-2.15	0.97	3.68	45	147	35.10	52.38	0.98
Big Blue	32	155	no	7	0	3.85	2.25	-1.82	0.91	2.29	20	136	30.34	46.34	0.96
Desert Queen	104	155	yes	1	0	24.03	2.07	-2.79	1.04	0.36	20	135	29.32	45.24	0.88
Bacon Flat	153	0	yes	2	0	7.57	2.42	-1.93	0.89	5.38	75	149	35.29	52.77	0.03
Rawhide-Wedell	62	151	no	10	0	29.41	1.83	-2.34	0.99	4.26	229	145	28.93	45.98	0.96
Wild Rose	151	0	yes	8	23	38.09	1.97	-1.91	0.72	1.01	63	135	36.38	52.20	0.03
Peterson	92	150	no	1	0	18.58	1.65	-2.53	1.07	1.71	57	153	35.42	53.41	0.99
Reese River	150	63	yes	2	0	20.40	2.26	-2.64	1.09	1.12	18	146	31.33	48.43	0.89
Silver Springs	60	149	yes	7	0	35.71	2.62	-2.87	0.72	0.74	176	112	26.80	39.99	0.54
Wabuska	108	146	no	8	6	50.74	2.78	-2.77	0.91	1.87	69	114	32.86	46.26	0.94
Darroughs	129	145	no	2	0	4.86	2.39	-2.25	0.88	4.01	31	137	37.85	53.89	0.98
Dixie Meadows	94	145	no	0	0	34.42	1.20	-1.74	0.96	4.18	129	129	46.24	61.40	1.00
Hawthorne 3	0	137	yes	7	0	52.33	2.34	-1.97	0.69	0.57	998	114	33.61	46.99	0.47
McLeod Hot Spring	88	134	no	10	0	4.78	2.18	-1.65	1.02	2.17	12	132	33.13	48.68	0.96

Abbreviations: STR, Structure type: 1) fault termination; 2) step-over; 3) accommodation zone; 4) major normal fault; 5) fault bend; 6) antithetic normal fault; 7) fault intersection; 8) displacement transfer zone; 9) pull apart; 10) undetermined. GT, geothermometer; TSTD, sum of slip and dilation tendency; HG, horizontal gravity gradient; EQ, earthquake.

Local Permeability

Local permeability includes four parameters: 1) structural setting; 2) recency of Quaternary faulting; 3) Quaternary fault slip rates; and 4) slip and dilation tendency on Quaternary faults. The latter three parameters are used to rank the individual structural settings. In addition, the structural settings themselves are ranked on the basis of general quality, certainty that they exist, and type of setting. Thus, local permeability is focused entirely on the identified favorable structural settings (Task 6). Recent studies indicate the importance of favorable structural settings in controlling geothermal systems across the Great Basin. Nearly all systems appear to occupy a favorable structural setting (Faulds et al., 2011, 2013; Faulds and Hinz, 2015). Our ranking scheme of these settings is based on the observation that structural complexity correlates directly with geothermal activity. Previous studies have shown that the more complex structural settings are the most conducive for geothermal activity and that compound or hybrid systems are particularly favorable for developing commercial-grade systems (Faulds et al., 2013; Dering and Faulds, 2103; Hinz et al., 2014b, 2015). For example, although accommodation zones are much less common than fault terminations and host ~9% of the geothermal systems in the Great Basin region, ~26% of the operating geothermal power plants reside in accommodation zones. In contrast, step-overs in normal

faults host ~33% of known systems and ~29% of operating power plants (Faulds et al., 2013; Hinz et al., 2015). Accommodation zones and displacement transfer zones are more than twice as likely to host a commercial-grade system compared to step-overs. This probably reflects the greater structural complexity in accommodation zones, which contain multiple fault terminations and fault intersections and are generally larger features than individual step-overs. Thus, the type of structural setting was ranked with the simplest receiving the lowest weighting and most complex the greatest, with an additional bonus added for hybrid settings. Rigorous statistics were difficult to develop due to the low number of operating systems, but our relative rankings weight the most complex settings (e.g., accommodation zones and displacement transfer zones; Fig. I-3) two times that of the simpler settings, roughly mirroring the difference in the likelihood of accommodation zones and step-overs in hosting a commercial-grade system.

Because the size of a geothermal system is related to potential electrical production, we also considered ranking the favorable settings on the basis of size (km^2). However, it is important to note that some operating systems, such as the 15-20 MW system at Bradys (Fig. I-2), occupy a relatively small favorable setting (e.g., 300 m wide step-over at Bradys), which would be difficult to detect without detailed geologic mapping and thus may go unnoticed in our review of favorable structural settings across the study area. Clearly, larger systems require greater volumes and are likely to correlate with the larger favorable settings, but small to moderate systems are possible within even the smallest favorable setting identified in our analysis. Thus, we did not include size of the favorable area in the current analysis, but will do so in subsequent more detailed analysis of individual areas in a potential Phase II of this study.

Although nearly all known geothermal systems appear to occupy a favorable structural setting, it is important to stress that Quaternary faulting also plays a crucial role, as evidenced by the strong correlation between high enthalpy systems in the Great Basin region with Quaternary faults (Bell and Ramelli, 2007, 2009). We further note that high enthalpy geothermal activity in favorable structural settings is largely absent in tectonically quiescent continental rifts (e.g., parts of eastern North America, west Africa, other passive continental margins, etc.). These relationships indicate that favorable structural settings have very little potential without spatially associated Quaternary faults. Not surprisingly, our analysis shows a strong association of geothermal systems in the study area with Quaternary faults that have ruptured in the past ~130 ka (Fig. M-3) and a more moderate correlation with slip rates on Quaternary faults (Fig. M-4). As discussed in detail in the regional permeability section, statistical analysis suggests that the correlation with fault recency is about twice that of slip rates.

We should also note, however, that Quaternary faulting is generally less pronounced and more difficult to document within the favorable structural settings, as such areas are characterized by multiple closely-spaced faults with minimal offset compared to major range-front faults that accommodate large offset in periodic major earthquakes. In order to account for this, slip rates and fault recency were evaluated on nearby Quaternary faults that projected into each identified favorable setting.

The relationship of young faults and their associated slip rates to the favorability of structural settings is confirmed by statistical analysis of step-over structural settings in the study area. Step-overs can be analyzed more quantitatively than the other settings because of their relatively common occurrence in the study area (178 examples), their widespread distribution throughout the study area, and their positive association with geothermal activity. The mean age (recency) designation for step-over settings associated with ≥130°C geothermal systems (the primary benchmark dataset) is 65 ± 19 ka, compared to a mean of 177 ka ± 21 for step-overs without known geothermal systems. Similarly, the mean slip rate designation for step-overs with ≥130°C geothermal systems is 0.151 mm/yr ± 0.031 mm/year, compared to 0.103 mm/yr ± 0.010 for step-overs without known geothermal systems.

Slip and dilation tendency on Quaternary faults was also incorporated into the calculation of local permeability. Because many of the favorable settings lie in areas where detection of Quaternary faults can be difficult, slip and dilation tendency was calculated based on the values of faults both within the delineated areas as well as on nearby faults projecting into such areas. An average local value was assigned for the sum of slip and dilation tendency and then incorporated into the ranking of individual structural settings. The correlation between geothermal systems and slip and dilation tendency is not nearly as strong as that for fault recency, fault slip rates, and structural settings (Fig. M-4). This is primarily due to the fact that

many Quaternary faults in the region are favorably oriented for slip and dilation in the current stress field. Thus, although most of the benchmarks have relatively high slip and dilation tendency values, so does most of the region outside of these areas.

Utilizing a combination of statistical analysis and expert driven estimates, we weighted the four parameters defining local permeability as follows (Fig. M-1): 1) 3x recency of faulting; 2) 2x structural setting; 3) 1.5x slip rate; and 4) 0.3x slip and dilation tendency. This hierarchy is based on the observation that Quaternary faults are required to maintain local permeability at levels sufficient for a high enthalpy system. However, as noted above, the correlation with the recency of faulting is about twice as strong as that for slip rates. Moreover, a favorable structural setting is also necessary for higher permeability, but has little effect on geothermal activity in the absence of Quaternary faults. Thus, structural setting was assigned a weighting between that of fault slip rate and recency, specifically 2x. For slip and dilation tendency, we selected 0.3x due to the relatively poor correlation with benchmarks in the study area. The implications of the local permeability index map (Fig. M-5) that combines these four parameters are discussed in the *Results-Discussion* section, which follows the *Methodology* section.

Errors: Errors were assigned to each category of structural setting, fault recency, slip rate, and slip rate/dilation tendency used in the weighting of structural settings. The errors were estimated by the structural team members based on their knowledge of the accuracy and precision of the fault. These estimated errors were transferred to the membership function. Propagation of the errors into the overall structural score was done using the sum of the variances weighted by the squares of the respective weights assigned to each grouping (e.g., $x3^2$ for recency; Fig. M-6).

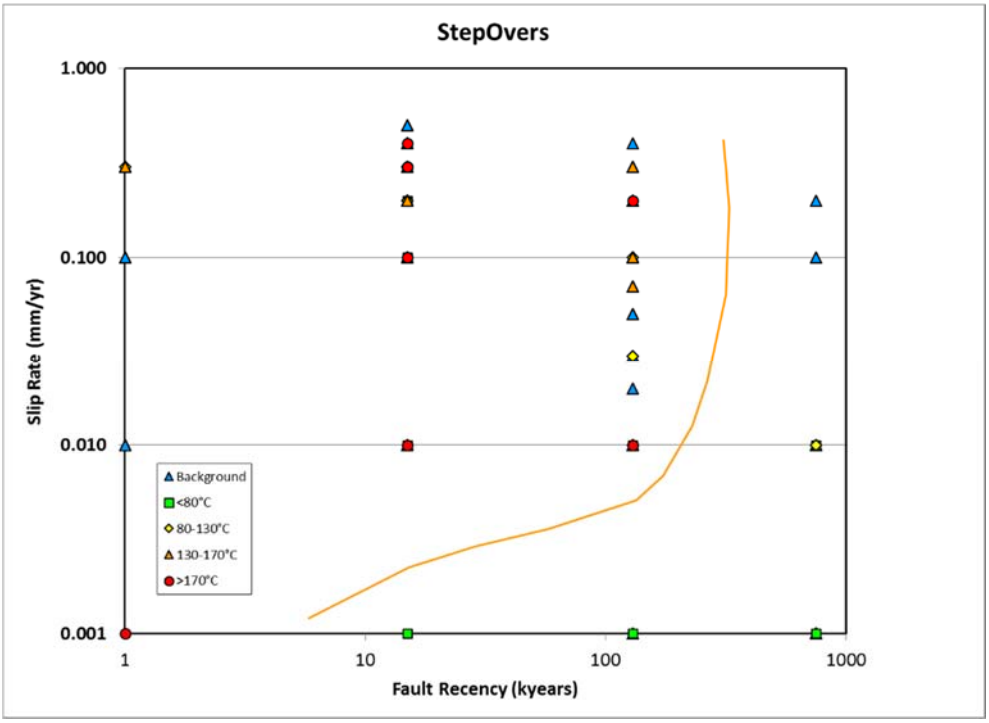

Figure M-3. Fault recency versus fault slip rate for benchmarks associated with fault step-overs in the study area colored by benchmark temperature category.

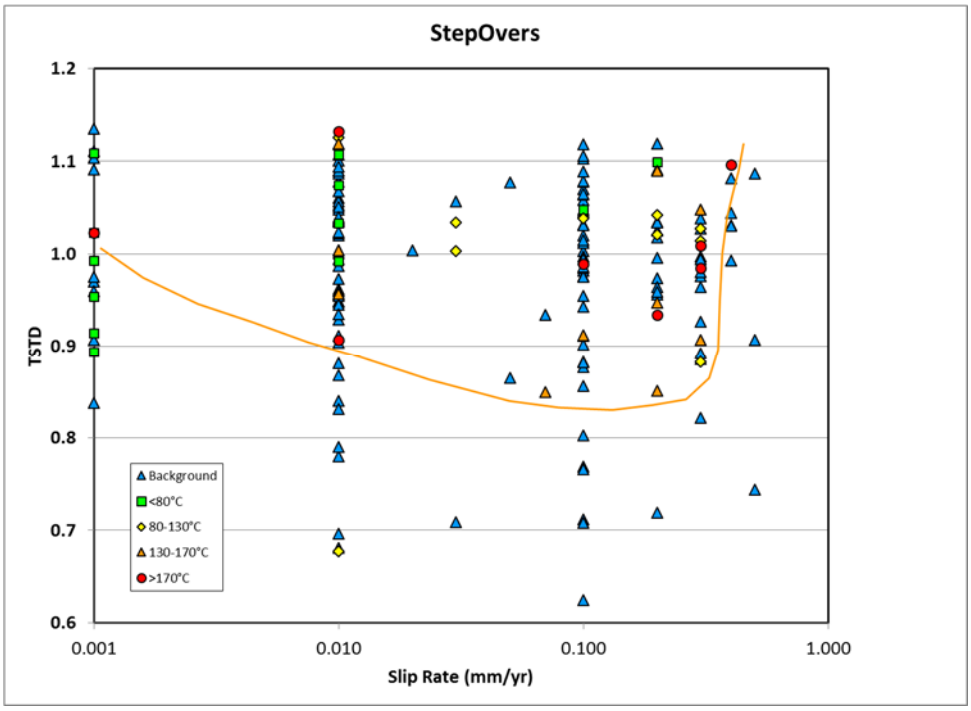

Figure M-4. Fault slip rate versus summed slip and dilation tendency for benchmarks associated with fault step-overs in the study areas colored by benchmark temperature category.

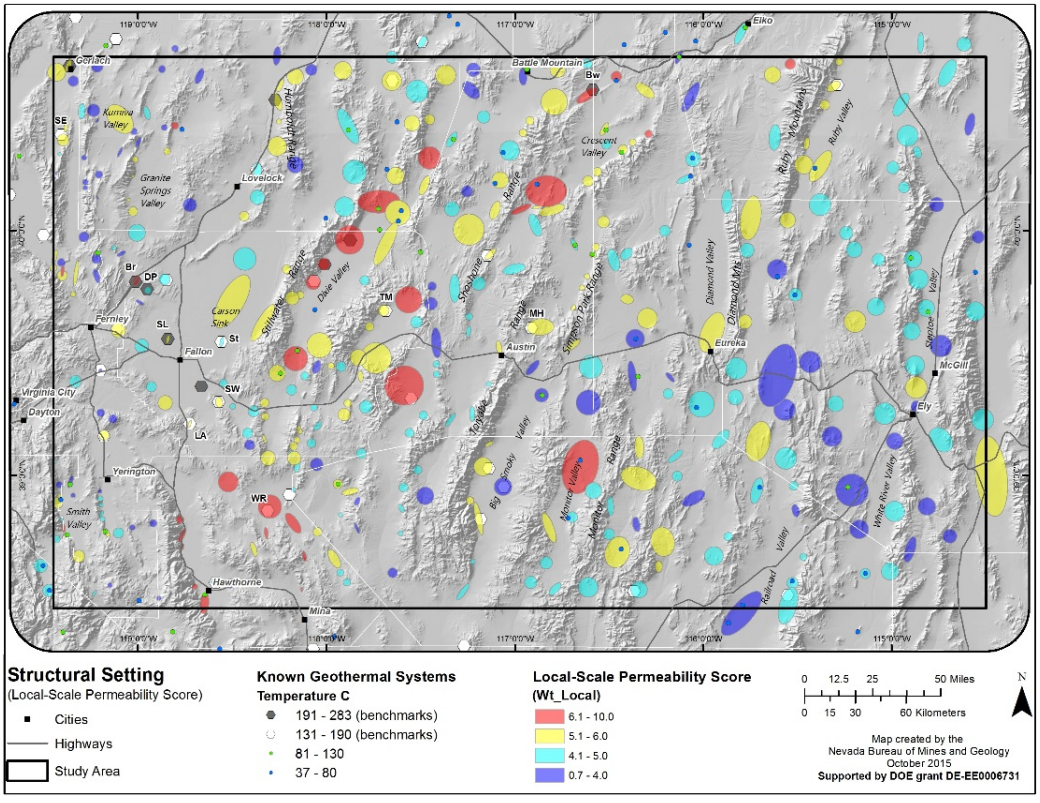

Figure M-5. Local-scale permeability scores for all structural settings.

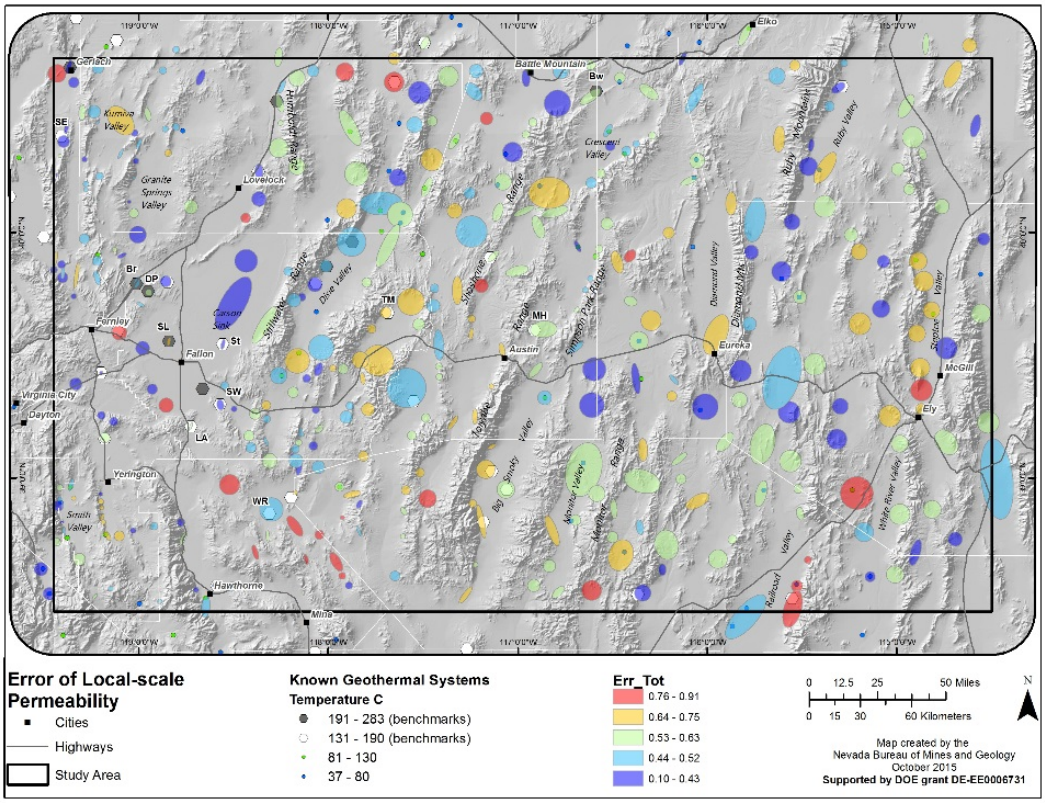

Figure M-6. Error of local-scale permeability for favorable structural settings.

Intermediate Permeability (Quaternary Fault Traces)

Input Data: Quaternary fault traces were included as a key ingredient in our fairway analysis to provide information intermediate in scale between local and regional permeability. The reasoning for inclusion of this parameter outside of local permeability is that some favorable structural settings, such as small step-overs and obscure fault intersections, may occur at a finer scale than could be observed in our analysis without available detailed geologic mapping (~1:24,000 scale). We note that only ~20% of this region has been mapped at sufficient detail to carry out a finer-scale analysis. Although relatively uncommon, some geothermal systems may also be controlled by major range-front faults. Thus, it is important to include Quaternary faults as a separate stand-alone layer in our permeability and fairway models, as Quaternary faults outside the favorable settings have some potential for hosting a high enthalpy system.

Data Layer/Model Construction: The detailed distribution of Quaternary faults was updated for this region based on analysis of existing databases (as described under Task 1). A buffer zone of 500 m was incorporated around all Quaternary faults (Fig. M-7).

Statistics: The 500 m buffer corresponds to the optimal fault buffer distance determined from weights-of-evidence analysis, which yielded a W+ of 0.84 +/- 0.33 for that distance.

Errors: The Quaternary fault weight assignment involves the use of a constant weight unmodified by other parameters, and the locations of many fault traces are relatively accurately known. This minimizes error, but potential misclassifications can occur near the edge of the fault buffers, and unrecognized Quaternary faults can introduce further errors. Accordingly, a constant error of 0.1 (12%) was assigned to Quaternary fault traces.

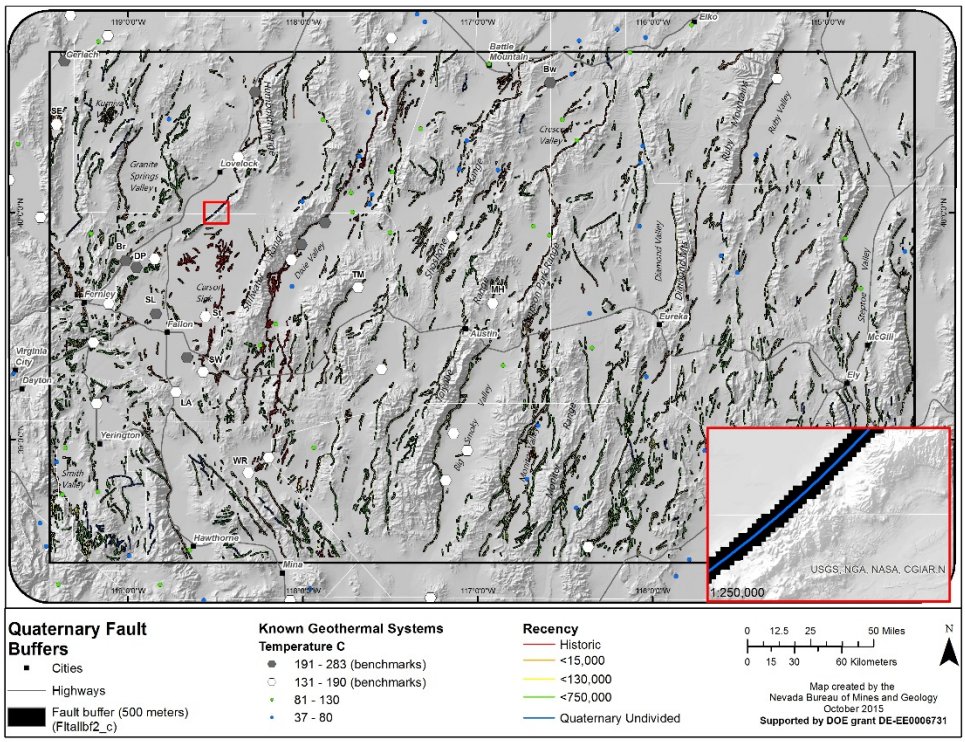

Figure M-7. Quaternary faults with 500m buffers within the study area.

Regional Permeability

The local favorability defined by structural setting and intermediate-scale favorability defined by Quaternary faults will not fully capture the distribution of geothermal potential throughout the study area, because not all structural settings and Quaternary faults have been recognized. Consequently, it is useful to include data that define broad regional zones of favorability to help highlight areas where additional exploration is most likely to find additional faults and structural settings that could ultimately lead to the discovery of more geothermal systems. The regional data thus provide a regional-scale perspective that may guide exploration strategies toward more local favorable targets, and they provide an independent method of evaluating geothermal potential for poorly studied areas that lack sufficient databases for careful analysis of local permeability. Seven types of regional-scale data were identified. They include 1) geodetic strain rate, 2) earthquake density, 3) age of Quaternary faulting, 4) Quaternary fault slip rates, 5) slip and dilation tendency on Quaternary faults, 6) horizontal gravity gradient, and 7) MT (low resistivity) anomalies. We note that age, slip rates, and slip-dilation tendency on Quaternary faults are included in both the regional- and local-scale permeability, because these parameters apply to both evaluating regional relations as well as the ranking of individual structural settings.

Geodetic Strain Rate:

Input Data: The world-wide strain model developed by Kreemer et al. (2014) was output at a customized 0.02-degree cell size and clipped to the study area.

Data Layer/Model Construction: The strain rate parameters of dilatation, shear, 2nd invariant of strain rate, and style of strain were calculated. Maps of each strain rate parameter were made and the correlation with known benchmarks was visually assessed. The equations used are standard and in the literature, with exception of strain style, which uses the formulation developed by Kreemer et al. (2014).

Statistics: Interrelationships among the predictive variables were explored with scatter plots that compared the distribution of strain rate and other parameters in the study area to the distribution of the benchmarks. Examined graphical relationships include:

- Strain style vs 2nd invariant
- Dilatation vs shear
- Absolute value of dilatation vs shear
- 2nd invariant vs slip rate (see below for discussion of slip rate)
- 2nd Invariant vs earthquakes (see below for discussion of earthquakes)

Logistic regression was used to determine optimized linear weights for combining input data together for predicting geothermal potential. Combinations of input data examined in this manner include:

- shear vs absolute value of dilatation
- 2nd invariant of strain rate vs strain style
- 2nd invariant of strain rate vs log of fault slip rate (slip rates discussed below)

The optimized weights were then used to combine these data pairs together into hybrid maps, which were evaluated in ArcGIS for their predictive ability relative to the benchmarks.

Bayesian statistics-based weights-of-evidence analysis were also used to quantify the relationship of the predictive data with the benchmark geothermal systems. Input data for weights-of-evidence included:

- The primary strain rate variables (the first four listed in part 1 above)
- Three hybrid combinations (shear vs dilatation, 2nd invariant vs strain style, and 2nd invariant vs slip rate). These layers were compared statistically against the six classes of benchmark geothermal systems in the study area (Figs. M-8 and M-9).

The analysis of interrelationships among the input data did identify significant co-relationships to predict geothermal potential. However, these relationships were sufficiently linear that they could be fully captured by weighted combinations of individual layers, without the need to create intermediate-stage hybrid data layers. Based on the statistical correlations and map patterns, the 2nd invariant of strain was chosen as the most stable and representative measure of strain rate with which to predict geothermal potential (maximum W+ = 0.96 +/- 0.27 with 16% of study area using the 34 high enthalpy benchmarks), although many of the other parameters performed nearly as well (Fig. M-10). Based on analysis of scatter plots and maps, the relationship between benchmarks and 2nd invariant of strain is best observed when the 2nd invariant is expressed in log format (log-normalized).

The 2nd invariant strain map shows two belts of higher strain: 1) a NW-trending zone along the Walker Lane belt of dextral shear and 2) a NNE-trending 120-km-wide zone centered on the central Nevada seismic belt, extending from the Carson Sink on the west to central Nevada and the McGinness Hills area on the east (Fig. M-10). Some of the highest strain rates are focused in the Dixie Valley area and between Dixie Valley and the Walker Lane. As previously discussed, a sizeable part of this signal may reflect the viscoelastic transient effects associated with earthquakes in the region over the past ~100 years. Analysis of the corrected and non-corrected fields showed that the non-corrected fields (that include the transient part of the relaxation strain rate field) were more effective at predicting the location of the geothermal systems, and thus the non-corrected field was incorporated into our analysis.

Errors: A GIS-based layer of errors associated with the 2nd Invariant of strain was provided by the Nevada Geodetic Laboratory, who participated in the development of the world strain model. These include errors associated with velocity determinations as well as with the interpolation of strain rates across a grid with variable densities and qualities of GPS stations (Fig. M-11).

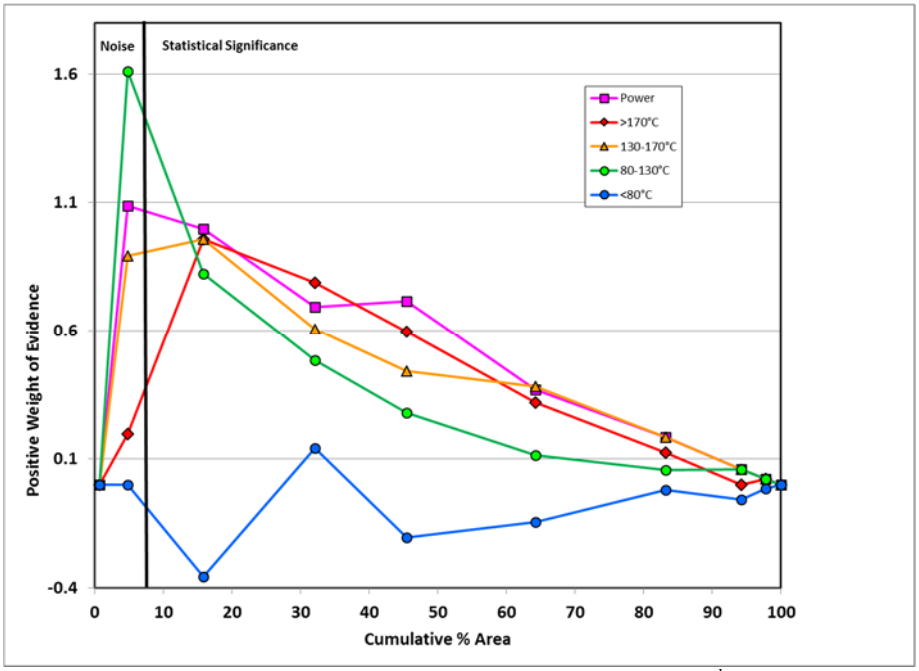

Figure M-8. Cumulative descending binary weights of evidence for the 2nd invariant of strain relative to benchmark categories. The statistically significant portion of the graph is indicated.

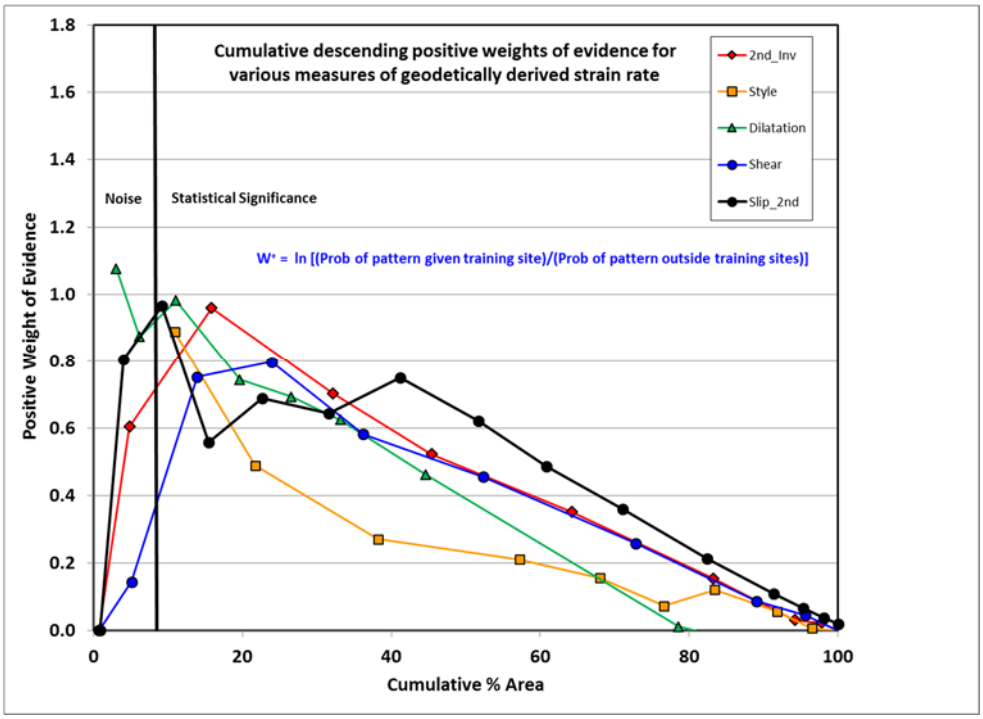

Figure M-9. Cumulative descending binary weights of evidence for multiple types of strain per the > 130°C benchmarks. Weights for a hybrid combined layer of 2nd invariant of strain x fault slip rate are included for comparison. The statistically significant portion of the graph is indicated.

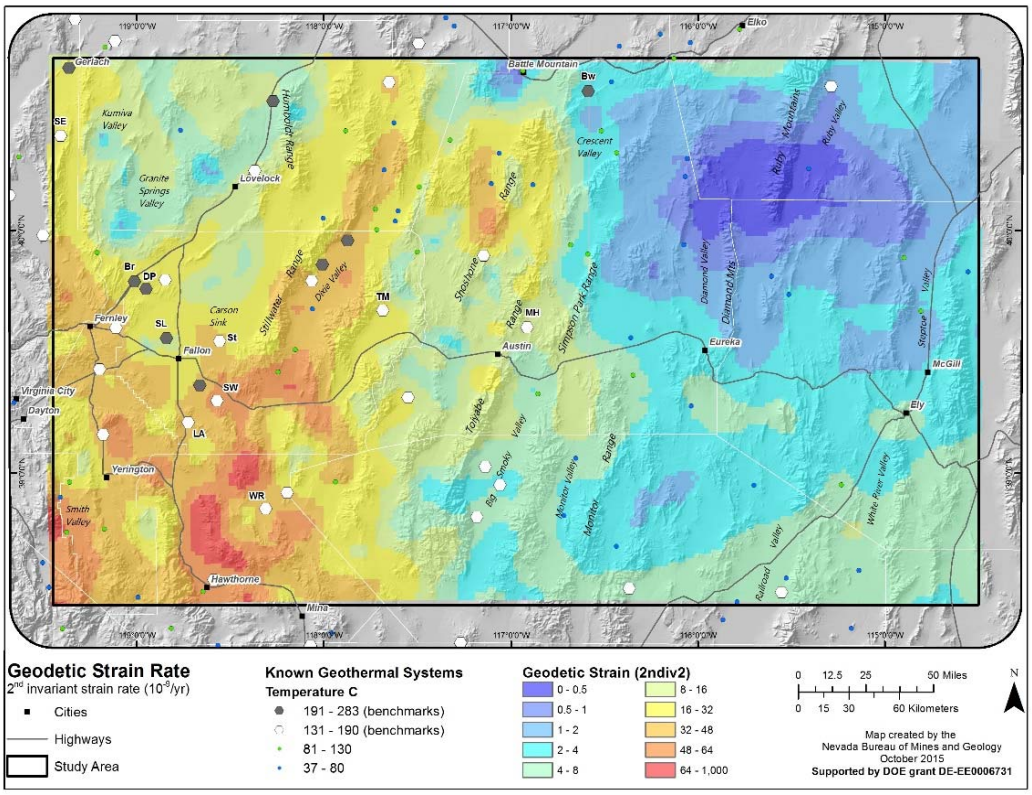

Figure M-10. Second invariant of the geodetic strain rate.

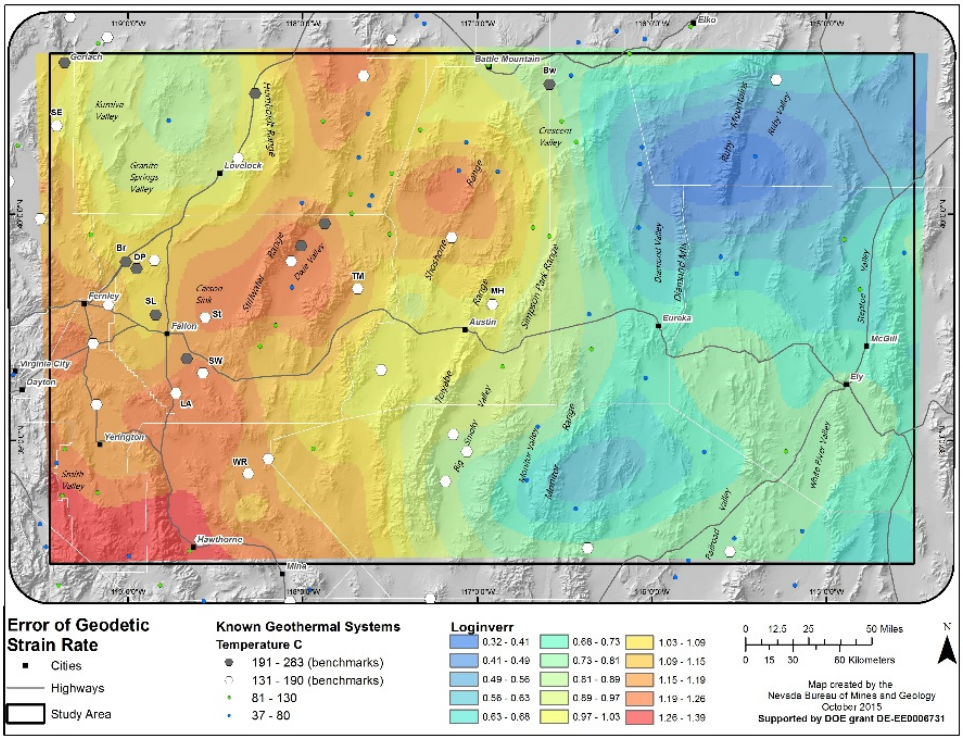

Figure M-11. Error of the 2nd invariant of the geodetic strain rate.

Earthquakes:

Input Data: Because we have taken the approach that the time-frequency of earthquakes has a more direct impact on geothermal potential than earthquake magnitude, the earthquake data were evaluated on the basis of location of epicenters and exclusive of magnitude, as described under Task 2.4. The earthquakes cluster along the Walker Lane, along the western fringe of the study area, in a NNE-trending zone along the central Nevada seismic belt centered on Dixie Valley, and in the central part of the southeastern quadrant of the study area (Fig. M-12).

Data Layer/Model Construction: The time-frequency of earthquakes and the distance from an earthquake epicenter to a point of interest (grid cell in model) were considered for modeling. Accordingly, a hybrid map was constructed that modeled earthquake occurrence density inversely weighted by distance. To approximate an inverse-distance-weighted sum of earthquake occurrence, the following procedures were completed:

Step 1) Earthquakes were summed for each grid cell in the model at four different distances (radii): - 20 km, 10 km, 5 km, and 2.5 km

Step 2) These four earthquake grids were then summed together to produce an overall earthquake activity map, effectively weighted inversely by distance (Fig. M-12B).

Statistics: The resulting weighted-sum earthquake grid was evaluated with weights-of-evidence using the primary benchmarks (n=34) and for a dataset of all benchmarks (n=87). A maximum positive weight of 0.67 +/- 0.26 over 23% of the study area was obtained using the primary benchmarks. This is a moderate degree of correlation, but it should be noted that these data are restricted to the past ~150 years, with robust databases from only the past several decades. These data may be biased depending on the position of a particular area within the overall earthquake cycle, which can be thousands to tens of thousands of years long in this region.

Errors: Estimated error (in log-scale units) ranges from a high of 0.5 at low end of earthquake sum scale (-0.3) to a "low" of 0.25 at the high end of the earthquake sum scale (3.4). Because of the log scale, the actual value of the error is higher at the high end. Low-end error of 0.5 is based on ½ the value induced by earthquake clusters in low quake-prone areas of the map, times ½ the value reduced in weight to account for less-likely occurrence of clusters in some parts of the map. High-end error of 0.25 is based on ½ range of perceived likely variation in earthquake density in high-earthquake-prone areas, based on observed heterogeneity on the map (Fig. M-13).

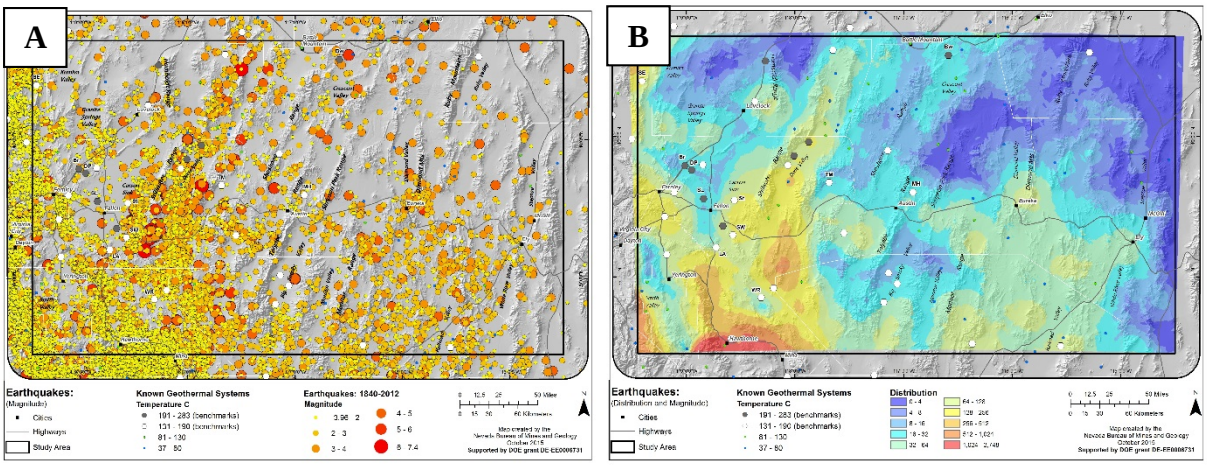

Figure M-12. Earthquake seismicity (A) and inverse-distance weighted sum of activity (B).

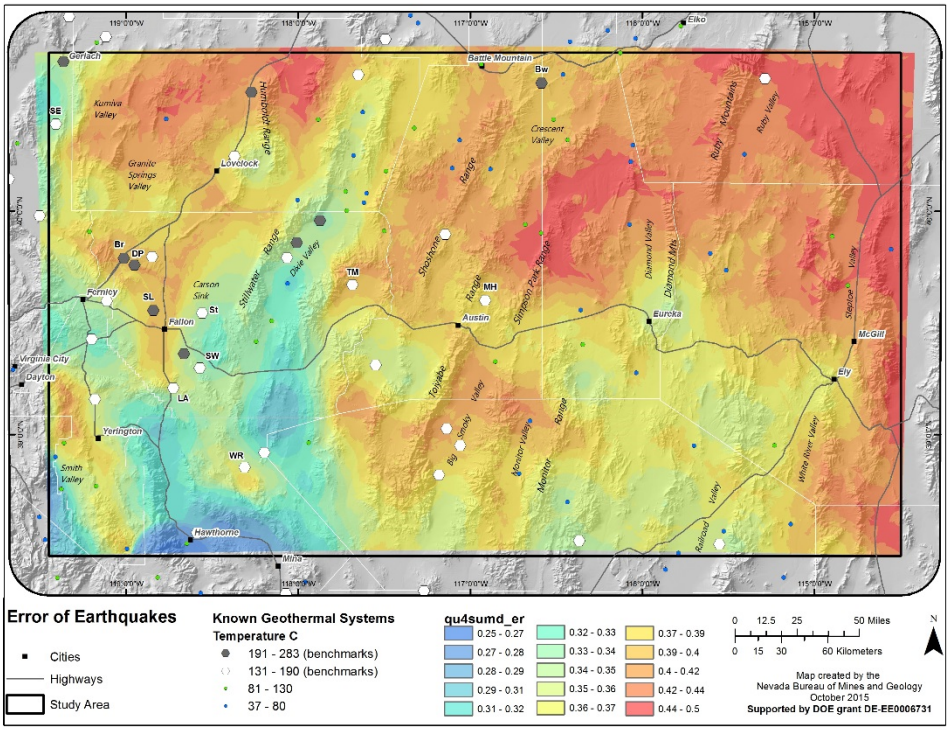

Figure M-13. Error of earthquake distribution.

Quaternary Fault Recency:

Input Data: The recency (age) of Quaternary faulting was updated for this region based on analysis of existing databases (as described under Task 1).

Data Layer/Model Construction: It is observed that recency of Quaternary faulting, though variable throughout the study area, is clearly clustered in specific areas (Fig. M-14A). For that reason, a regionally interpolated map of fault recency, in which values of recency are estimated for each grid cell in the model, appears to have predictive potential, and subsequent statistical analysis support this view (see below). Both normal and strike-slip faults were used. The map was generated in the following steps:

Step 1) Ages of faults were assigned using the maximum age of a given category.

Step 2) Historic faults were grouped with 15,000 yr faults.

Step 3) Fault ages were converted to their Log10 equivalents (log-transformed).

Step 4) The vertices of the fault line segments were converted to a point dataset so that an interpolated map could be created.

Step 5) an interpolated map of fault age was created using inverse distance weighting with a power of 1 and the following criteria: cell size 1000 m, fixed search radius of 20 km, minimum number of points = 1.

Three versions of maps were produced with the following input-data treatments: 1) using all Quaternary faults, 2) using all Quaternary faults transformed to log-scale, and 3) using log-scaled Quaternary faults with historic faults grouped with 15 ka faults. This latter version produced the most uniform and preferred results (Fig. M-14B).

Statistics: The log-scaled recency of faulting map (Fig. M-14B) shows an en echelon pattern of activity across the study area, with loci in the Carson Sink-Dixie Valley region, Battle Mountain area, Ruby Mountains, and Railroad Valley. Weights-of-evidence was used to compare the recency map against all six categories of benchmarks. A maximum positive weight of 1.75 +/- 0.45 was obtained with 2.6% of the study area using the primary >130°C benchmarks.

Errors: A 0.35 error in log-space is scaled from 0 to 0.35 depending on distance to nearest Quaternary fault, maximizing at a 12 km distance. The value of 0.35 equals ½ of the estimated 1/3 local contribution to the log10 fault recency grid (Fig M14-B), the other 2/3 being more regional in character. This is added (in variance space) to a constant error equal to 10% of range of Log Fault Recency values (0.2; Fig. M-15).

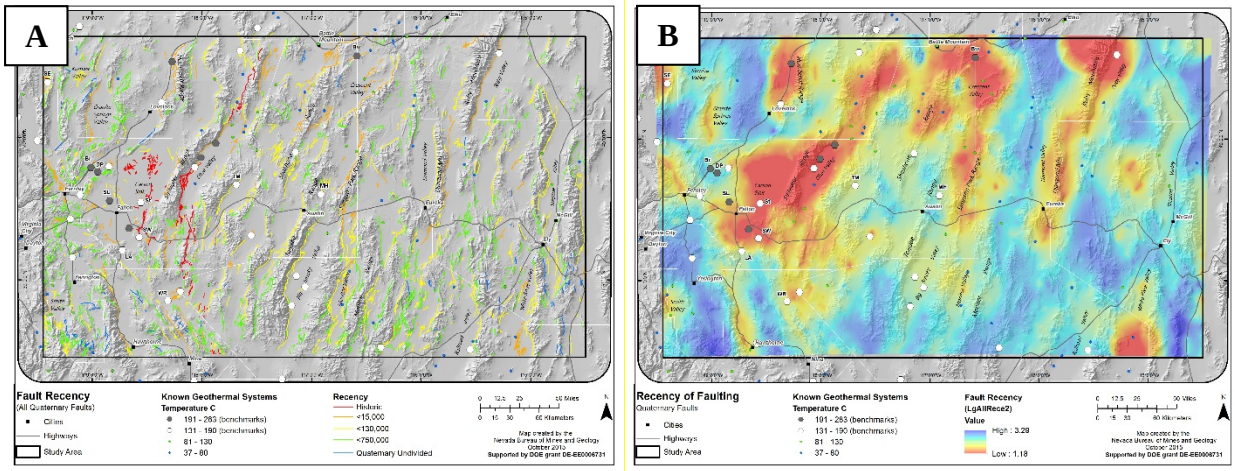

Figure M-14. Quaternary fault rupture age (A) and interpolated fault rupture age (B).

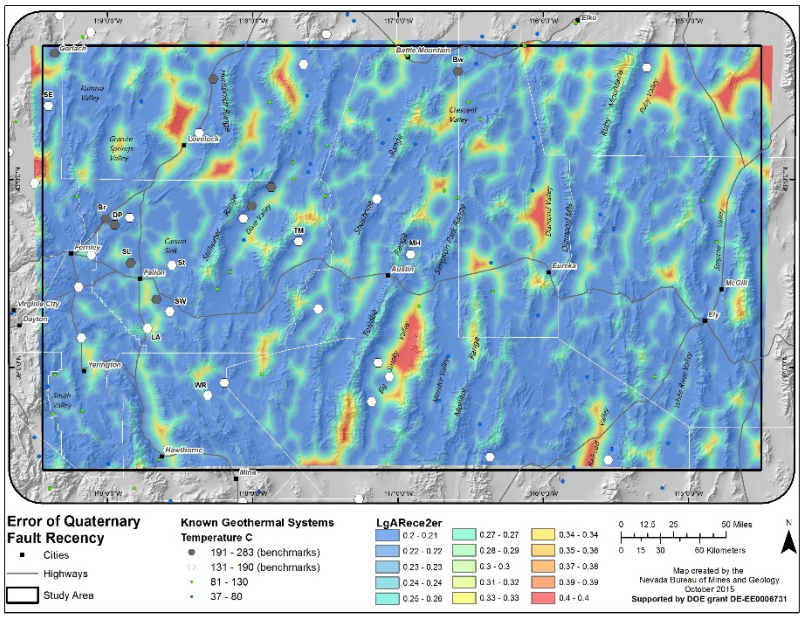

Figure M-15. Error of the Quaternary fault recency model.

Quaternary Fault Slip Rates:

Input Data: Slip rates on Quaternary faults were updated for this region based on analysis of existing databases (as described under Task 1).

Data Layer/Model Construction: Similar to the case with fault recency, it is observed that Quaternary fault slip rates, though variable throughout the study area, are clearly clustered in specific areas (Fig. M-16). For that reason, an interpolated map of fault slip rates, in which values of slip rate are estimated for each grid cell in the model, appears to have predictive potential, and subsequent statistical analysis support this view (see below). Both normal and strike-slip faults were used. The predictive map was created in the following steps:

Step 1) The slip rate was log-transformed (converted to Log10) for each fault segment.
Step 2) The vertices of the fault line segments were converted to a point dataset so that an interpolated map could be created.
Step 3) Interpolated maps of slip rate and log base 10 of the slip rate were created using inverse distance weighting with a power of 1, using the following criteria: cell size 1000 m, fixed search radius of 20 km, minimum number of points = 1.

Three versions of maps were produced, using: 1) normal faults, with slip rates not log-transformed, 2) normal faults transformed to log-scale, and 3) all faults (both normal and strike-slip) transformed to log-scale. This final version produced the most uniform and sensible results and was used for modeling (Fig. 16C).

Statistics: Fault slip rates show a scattered distribution across the region with several loci generally associated with major range-front faults. Notably, many of the high enthalpy systems occur near the margins of areas with higher slip rates (e.g., Gerlach, Lee Allen, Wild Rose, systems in Dixie Valley, Tungsten Mt., Peterson) or between areas with higher slip rates (e.g., McGinness Hills). Weights-of-evidence was used to compare the Log-scaled slip rate map against all six categories of benchmarks. A maximum positive weight of 1.21 +/- 0.45 was obtained with 4% of the study area using the primary benchmark (high-medium temperature) data set. This is a slightly lower correlation then for the recency of fault category.

Errors: A 0.68 error is scaled from 0 to 0.68 depending on distance to the nearest Quaternary fault, maximizing at a 12 km distance. The value of 0.68 equals one half of the estimated one third local contribution to the (Fig. 16C) grid, the other 2/3 being more regional in character. This is added (in variance space) to a constant error equal to 10% of the range of values (0.4; Fig. 17).

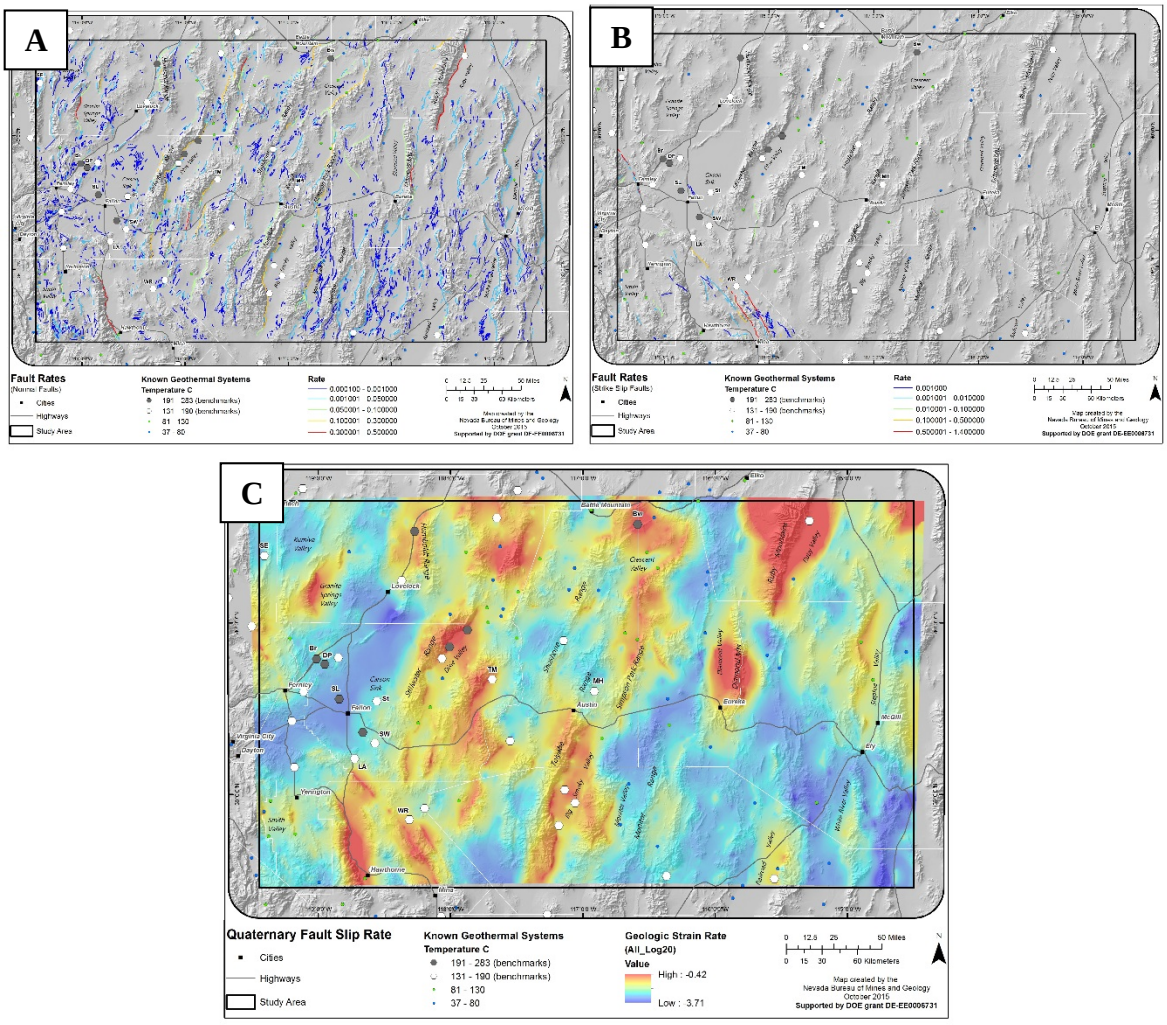

Figure M-16. Normal fault slip rates (A), strike-slip fault slip rates (B), and interpolated fault slip rates combining both Quaternary normal and strike-slip fault slip rates (C).

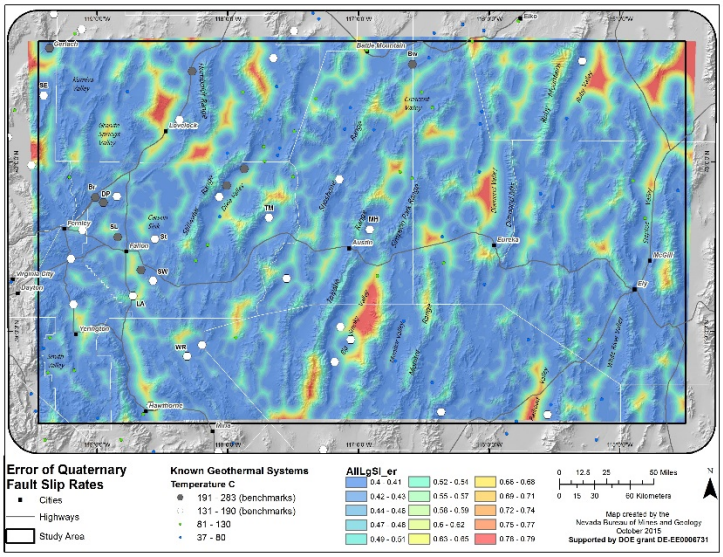

Figure M-17. Error of the Quaternary fault slip rates.

Fault Slip and Dilation Tendency:

Input Data: Slip and dilation tendency on Quaternary faults (as described under Task 7) was incorporated into the analysis of regional-scale permeability. These results were summed and are shown in Figure M-18.

Data Layer/Model Construction: Similar to the case with fault recency, it is observed that slip and dilation tendency, though variable throughout the study area, are clustered in specific areas. This degree of regional correlation is caused by the somewhat uniform character of the stress field over distance and the tendency of young faults in a given area to have similar strikes. For these reasons, an interpolated map of summed slip and dilation tendency (TSTD; Fig. M-18) was thought to have predictive potential. However, subsequent statistical analysis has not defined a clear relationship, and for that reason, the weight given to this layer has been minimized (see later sections). Both normal and strike-slip faults were integrated in a single interpolated map in the following steps:

Step 1) The vertices of the fault line segments were converted to a point dataset so that an interpolated map could be created. (this was done previously).

Step 2) An interpolated map of TSTD was produced using inverse distance weighting with a power of 1 and the following criteria: cell size 1000 m, fixed search radius of 20 km, and minimum number of points equal to 1.

All Quaternary faults, including both normal and strike-slip were used, and the data were not log-transformed.

Statistics: Weights-of-evidence was used to compare the TSTD map against all six categories of benchmarks, and no statistically significant correlations were found. For both local and regional-scale permeability, the correlation between geothermal systems is relatively weak compared to age and slip rates on Quaternary faults (Figs. M-14B and M-16C), as most of the region contains Quaternary faults that are favorably oriented for slip and dilation in the current stress field.

Errors: A 0.12 error is scaled from 0 to 0.12 depending on distance to the nearest Quaternary fault, reaching a maximum value at a 12 km distance. The value of 0.12 equals ½ of the estimated 1/3 local contribution to the grid (fig. M-18B), the other 2/3 being more regional in character. This is added (in variance space) to a constant error equaling 10% of the range of values (0.4; Fig. M-19).

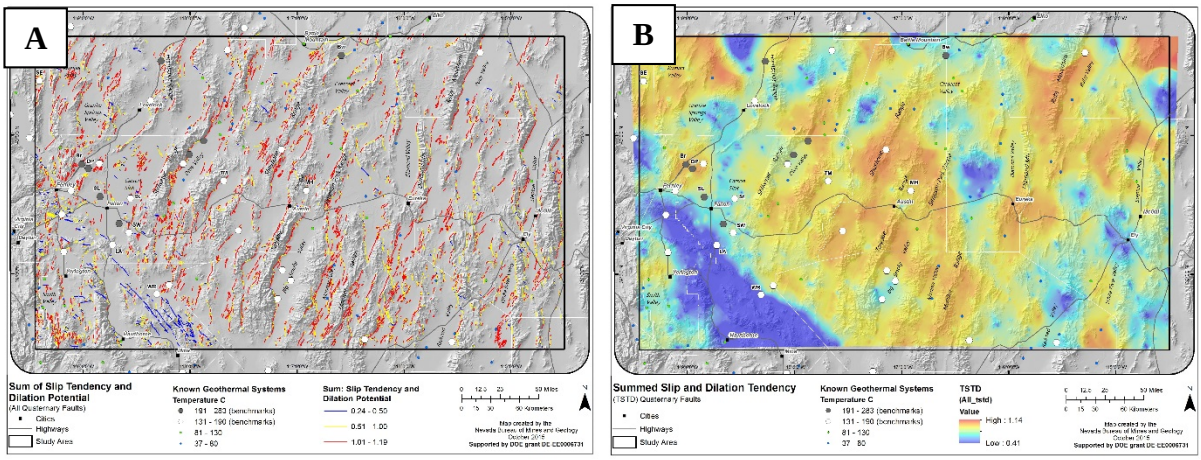

Figure M-18. Sum of the slip and dilation potential results calculated for Quaternary faults (A) and interpolated sum of slip and dilation potential (B).

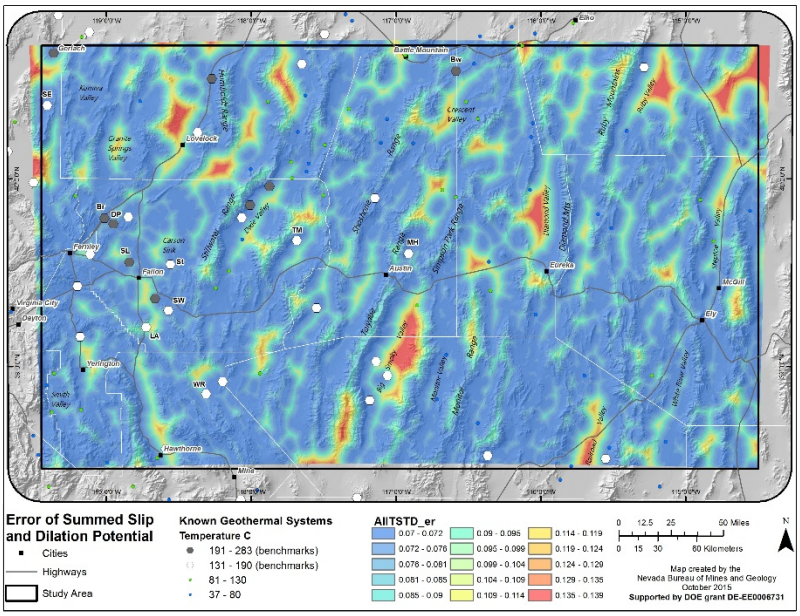

Figure M-19. Error of the summed slip and dilation potential of Quaternary faults.

Gravity:

Data Input: Several different derivatives of gravity data were provided for this study, including complete Bouguer anomalies, horizontal and vertical gravity derivatives, and derivative depth to basement calculations (see Task 2.2; Fig. P-12). Horizontal gravity gradient in this region is typically highest in value in the vicinity of major normal faults due to the juxtaposition of lower density sedimentary basin fill against high density basement rocks. Although the main segments of major normal faults are typically not associated with geothermal activity, the ends and discontinuities (e.g., step-overs, intersections with other faults) along such faults do correlate with geothermal systems. A more rigorous analysis of the gravity signature, whereby the lateral terminations and subtle discontinuities of major gravity gradients would be delineated, was beyond the scope of the Phase I study, as it requires both acquisition of detailed gravity surveys in several representative areas and development of new algorithms for analyzing and distinguishing gravity gradients.

Data Layer/Model Construction: Both the total horizontal gradient (Fig. M-20; HGM) and the first vertical derivative of the gravity field (VDHGM) were found to provide useful information for predicting geothermal potential based on their ability to track young faults. Accordingly, color-scaled maps of both of these derivative products were produced and evaluated statistically with the benchmarks.

Statistics: Weights-of-evidence was used to evaluate the correlation of the HGM and VDHGM maps with all six categories of benchmarks (Fig. M-21). In the case of VDHGM, as an experiment, two different grid cell sizes were evaluated, 400 m and 800 m. Each of the maps yielded similar results, with a positive weight-of-evidence in some cases exceeding 4 at the highest levels of the gradient at less than 0.1% of the study area. The HGM (Fig. M-20) was chosen as the best representative for modeling gravity, because the map as a whole exhibited a lower degree of background noise compared to the VDHGM, though statistical weights were similar for both. Logistic regression analysis with the benchmarks indicate an x0.8 weight for this parameter in the regional permeability model. We adjusted this to x1.0 based on expert geologic opinion. Thus, there is a relatively strong correlation between horizontal gradient and the 34 benchmark systems. A more rigorous analysis of the gravity signature, whereby the lateral terminations and subtle discontinuities of major gravity gradients would be delineated, was beyond the scope of the Phase I study, as it requires both acquisition of detailed gravity surveys in several representative areas and development of new algorithms for analyzing and distinguishing gravity gradients.

Errors: For the map as a whole, a 10-15% relative error was estimated by Dr. Gary Oppliger. A second component of error is a function of station density, where station density function ranges from 1 to 0, multiplied by standard deviation of population (which just happens to equal 1.0). The station density function equals 1 if zero stations are present in 5 km-radius-circle, and goes to zero when 10 stations are present in a 5 km-radius circle, and stays at zero with more stations (>10; Fig. M-22).

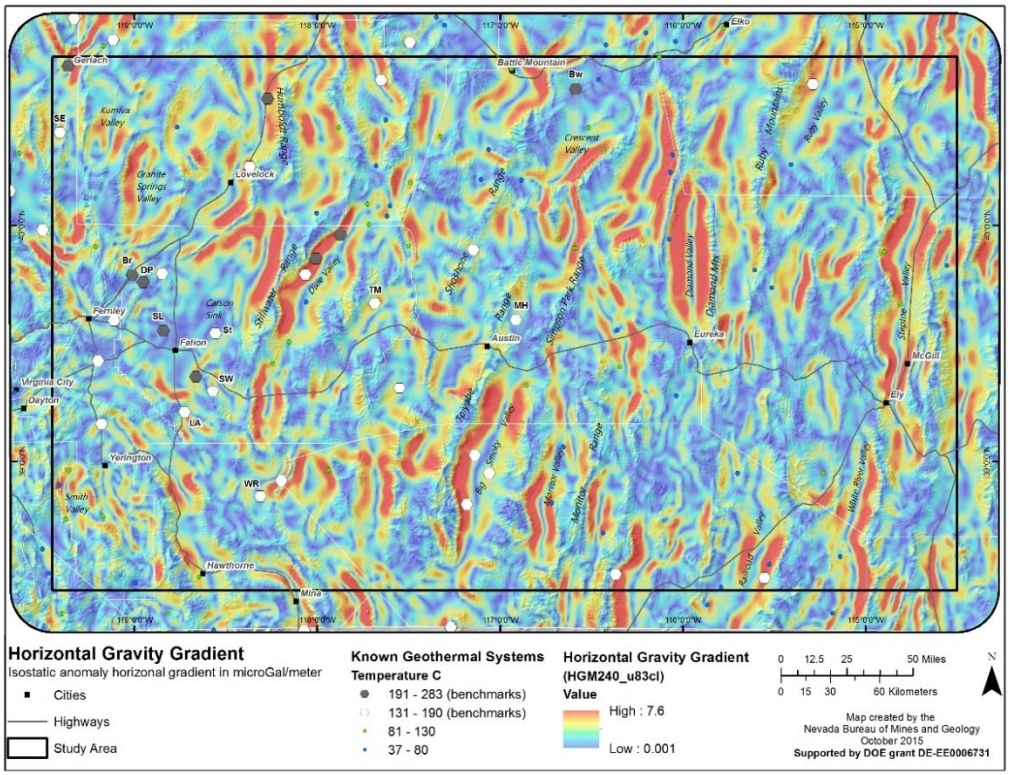

Figure M-20. The total horizontal derivative of the Complete Bouguer anomaly computed at 2.40 g/cc.

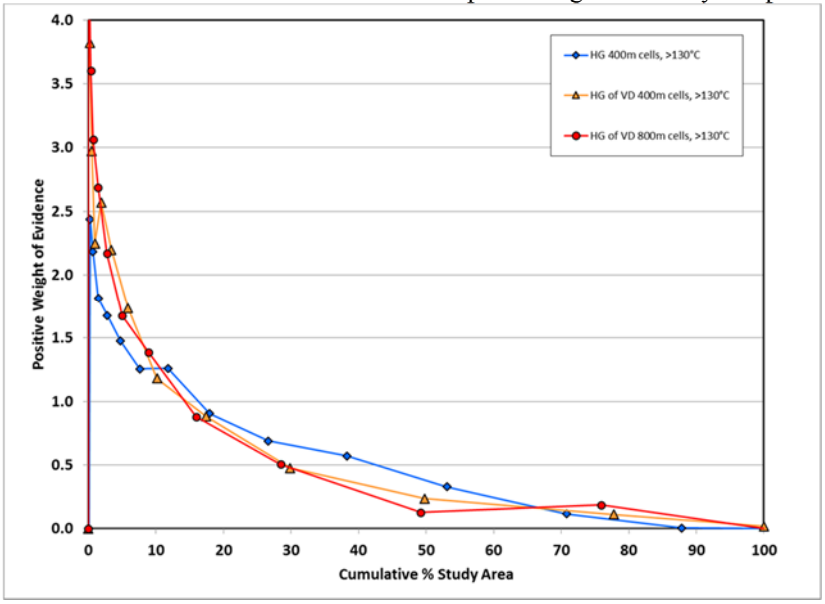

Figure M-21. Cumulative descending binary weights of evidence for horizontal gravity gradient, horizontal gradient of the first derivative with 400 m cells, and horizontal gradient of the first vertical derivative with 800 m cells versus the >130 °C benchmarks.

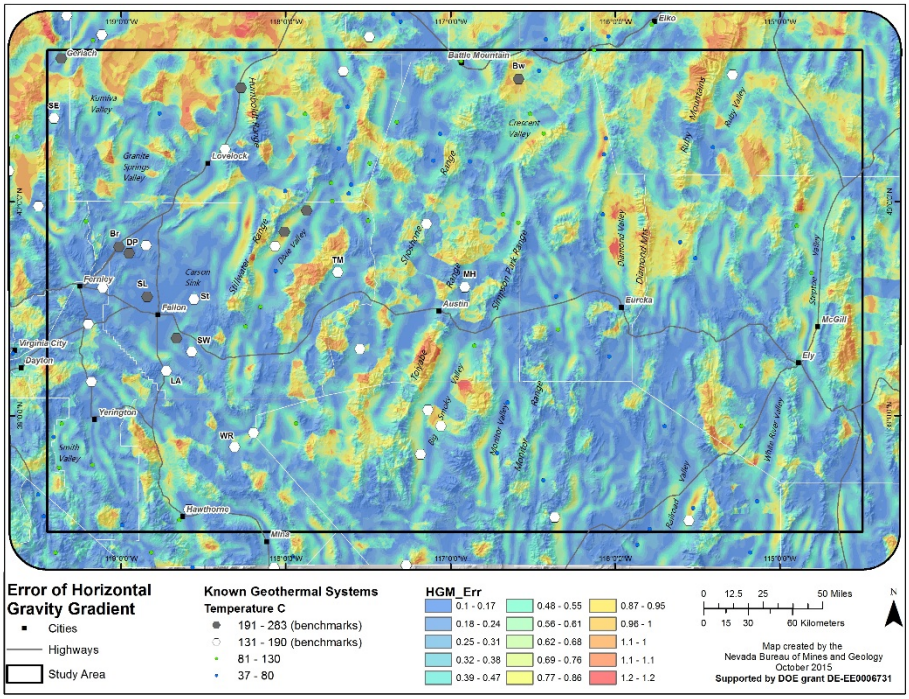

Figure M-22. Error in the horizontal derivative of the Complete Bouguer anomaly computed at 2.40 g/cc.

Magnetotelluric (MT) Data:

Several detailed MT surveys were provided for this study, but overall MT data cover less than ~5% of the study area, making correlations with the 34 benchmarks difficult. Only four of the benchmarks lie within areas encompassed by the MT surveys. Although the correlation between some of the major producing geothermal fields, such as Dixie Valley and McGinness Hills, and crustal-scale low-resistivity anomalies is well established (Fig. P-14; Wannamaker et al., 2013), the lack of widespread coverage across the study area precludes adequate statistical analysis and related extrapolations of geothermal favorability. The resistivity values from ~2.75 to 3.65 km depth were incorporated into the analysis for the surveyed areas but are not presently included in the overall play fairway analysis. These data will be useful for detailed studies in Phase II.

Regional Permeability Model:

Input Data: Six of the regional data layers described above were combined into a single regional-scale permeability model. These layers are strain rate, earthquakes, fault recency, fault slip rate, gravity, and slip-dilation tendency.

Model Construction, Statistics, and Play Fairway Analysis (PFA) Weights: Statistics were used to guide the assignment of weights to each layer. Two types of statistics were run.

1) Weights-of-evidence: Binary weight tables were calculated for each of the five data layers listed above, plus the slip and dilation tendency layer. Positive weights (all of which are statistically significant) at a uniform 20% of the study area are as follows:

Horizontal gravity gradient:	0.80
2nd invariant, strain rate:	0.90
Fault slip rate:	0.60
Fault recency:	0.70
Earthquakes:	0.70

Slip and Dilation: no statistically significant correlation observed

2) Logistic regression: Area-weighted linear logistic regression was used to combine the above five evidence layers into a single regional permeability model. To ensure approximately equivalent data distributions, the geodetic strain rate, earthquakes, fault recency, and fault slip rate grids were converted to log-format before combination with the horizontal gravity gradient. Results of that output are shown in Figure M-23.

Given the broad similarity of weights for each of the data layers shown in #1 above, the research team decided to combine each of the five main data layers using equal weights for each. In addition, on the argument that the slip and dilation tendency should correlate to some degree with geothermal activity, and given the limitations of the benchmark data set (a greater number of benchmarks would improve statistical distinctions), we opted to include slip and dilation tendency as an additional input layer, but at a reduced weight of 0.1. Each of the input data layers was rescaled or normalized to an equivalent mean and standard deviation prior to summation into a single output layer (Fig. M-23). The color-scaled depiction of this layer (Fig. M-24) was found to be virtually indistinguishable from the logistic regression version calculated above (Fig. M-23).

Errors: As described above, data-input/quality-related errors were estimated for each of the input layers to the regional permeability model. The combined error was estimated using a basic propagation equation involving the sum of the variances of each input layer. Prior to summation, each component variance was adjusted by multiplying by the square of the respective scaling factor used to normalize the grid prior to their summation to form the final regional permeability model. Those scaling factors are:

Horizontal gravity gradient: 1.0
Second-invariant, strain: 1.815
Earthquakes: 1.717
Fault slip rate: 2.227
Fault recency: 2.408
Fault slip and dilation: 0 (this layer has a negligible impact on the overall model)

The output error map in relative terms (divided by the value of the regional permeability model) is shown in Figure M-25. In general, relative error tends to be higher in areas where estimated values of regional permeability are low. Significant issues of data quality do not appear to be present in the model.

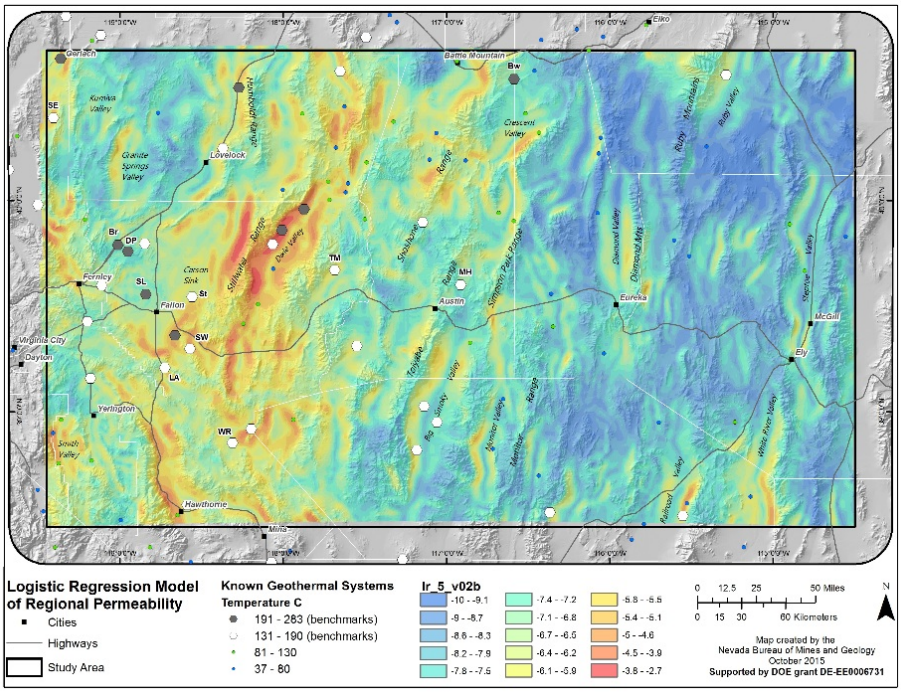

Figure M-23. Logistic regression model of the regional-scale permeability.

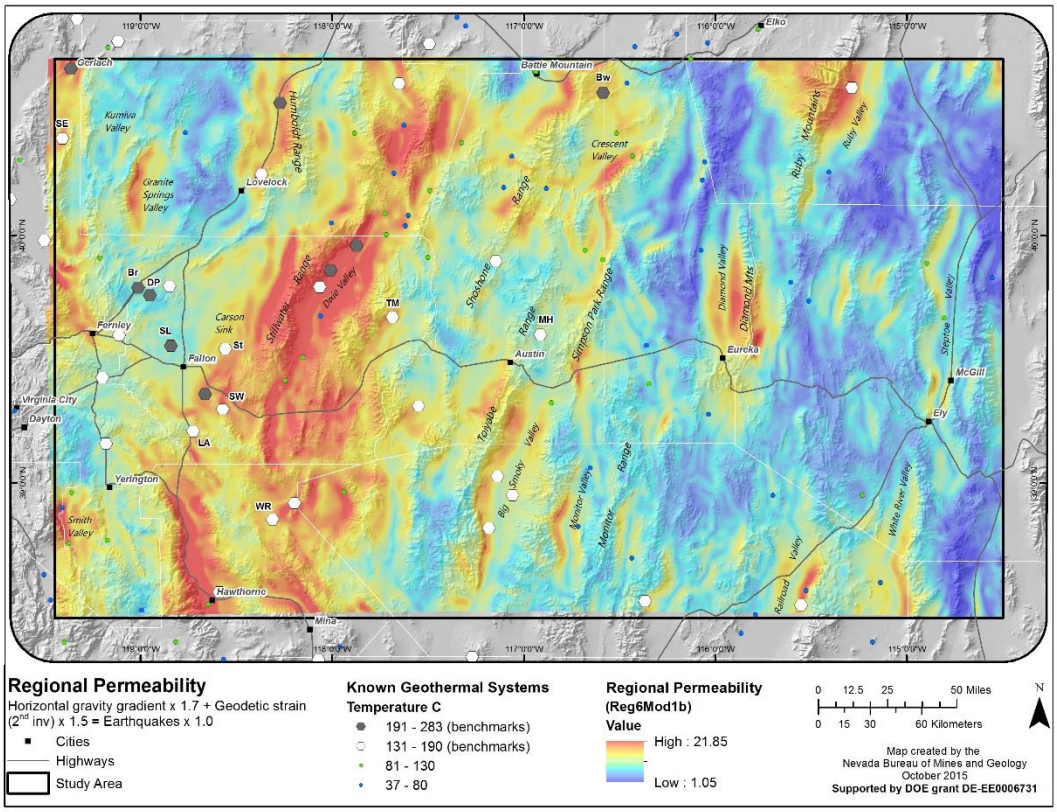

Figure M-24. Regional permeability model integrating the horizontal gravity gradient, 2nd invariant of the strain rate, fault slip rate, fault recency, earthquakes, and slip and dilation tendency.

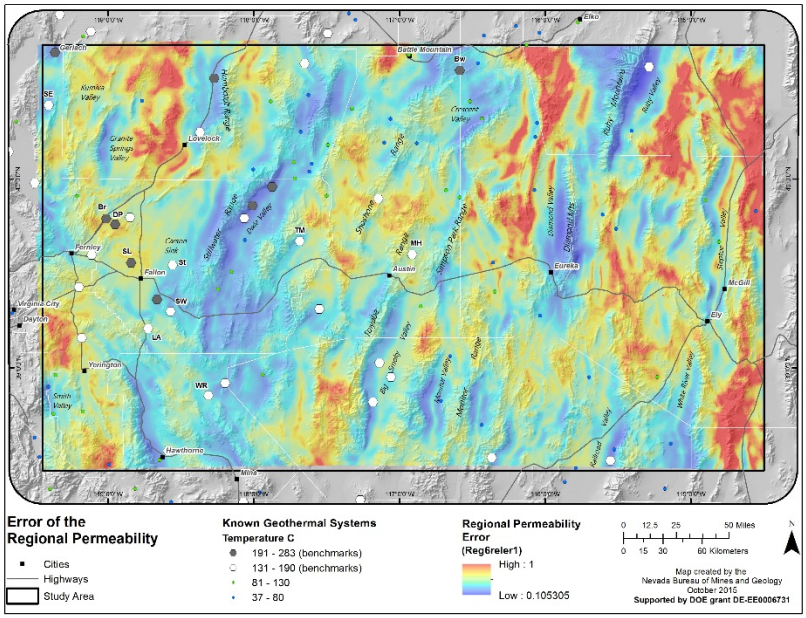

Figure M-25. Relative error of the regional-scale permeability.

Combined Permeability Model

The local- and regional-scale permeability models were combined with the intermediate-scale Quaternary faults layer to generate an overall *combined* permeability model. Relative weight assignments were guided by statistics. Weights-of-evidence analysis using the 34 primary benchmarks yielded positive weights of 2.2, 0.84, and 1.4, respectively for the local-scale, intermediate-scale, and regional-scale models (at a normalized 10% of cumulative study area). This translates to relative weights of 1.5, 0.6, and 1.0 for each layer. Given the tendency of the local-permeability layer to be marginally over-correlated due to better mapping detail available for geothermal areas compared to the rest of the study area, it was decided to moderately reduce its weight, and a simplified overall weighting scheme of 1.0, 0.5, and 1.0 was adopted for combining the local, intermediate, and regional layers together, respectively (Fig. M-26).

Errors: The error of the combined permeability model was propagated from the individual contributing layers using the sum of error variances of the three input layers, each weighted by the square of their respective scaling factors. Similar to the regional permeability model, relative error tends to be higher in areas where the estimated values of combined permeability index are low (Fig. M-27).

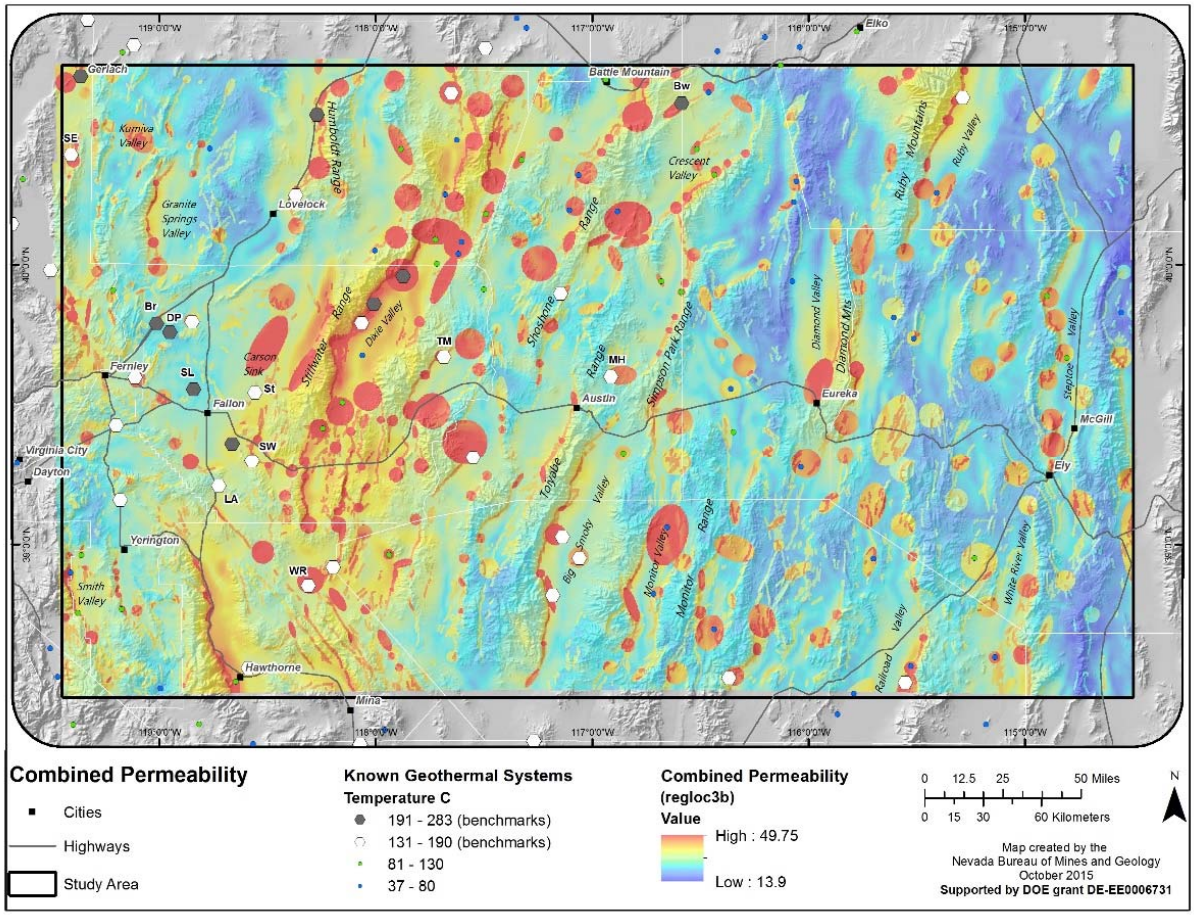

Figure. M-26. Combined permeability model.

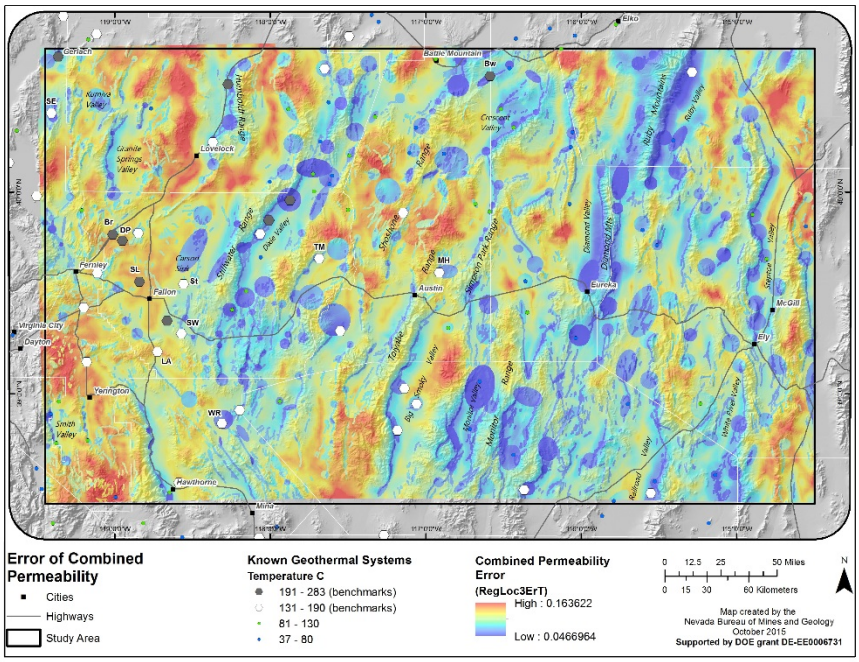

Figure M-27. Relative error for combined permeability model.

Heat Source Model (Temperature)

The construction of the heat model, which portrays temperatures at 3 km depth, is described in Task 1 above. This map reveals broad zones of elevated temperatures across the north-central and northeastern parts of the study area (Fig. P-4). The correlation of this map with geothermal systems was previously documented by Coolbaugh et al. (2005). Based on those statistical relationships and the fact that heat is considered one of the primary hierarchal components of a geothermal system, this layer forms an integral component of the fairway model.

Errors: A spatial assessment of error distribution was not made when the heat model was first produced 10 years ago (Coolbaugh et al., 2005). However, because of the incorporation of geology into this model to estimate local thermal conductivities, this model is significantly more accurate at the scale of this project than other regional heat flow models. Nevertheless, errors can be significant where well data are lacking or where lithologically derived estimates of thermal conductivity are not representative. To account for these issues, a relative error of 15% was assigned to the heat model. This is considered a liberal estimate of error, since +/-15% represents a significant amount of the entire 100°C range of temperatures present at a depth of 3 km in the heat model for the study area.

The Fairway

The heat model and the combined permeability model were merged to produce "The Fairway", which forms the primary predictive data product of this study. In order to assess in detail the optimal manner of combining the heat and permeability layers together to form the fairway, the full distribution of heat source and permeability values in the study area were compared to the geothermal benchmarks using a scatter plot (Figure M-28).

The scatter plot demonstrates that geothermal systems are strongly associated with high values of the combined permeability index, consistent with the high positive weights of evidence obtained using the 34 primary geothermal benchmarks. These positive weights include 2.2 +/- 0.18 at a 10% threshold of the

study area and 3.0 +/- 0.42 at a 1% threshold of the study area. These weights clearly show that the combined permeability index is a strong predictor of geothermal potential.

In contrast to the permeability index, regional temperatures at 3 km do not appear to be good predictors of geothermal potential within the confines of the study area (note that the temperature map specifically excludes geothermal wells so that it represents a regional temperature distribution independent of geothermal activity). This lack of correlation is confirmed by logistic regression, which, based on the data, generates a set of discriminator lines nearly parallel to the x-axis (blue line, Fig. M-28). However, a more regionally based assessment over the entire Great Basin (Coolbaugh et al., 2005) identified a statistically significant correlation between the same temperature data and geothermal systems. Given the expectation that regional temperature anomalies should impact the economic viability of geothermal systems by generating sufficient heat at shallower depths, where fractures are more likely to have sufficient permeabilities, it was considered important to include the heat model in the fairway calculation. The relatively small size of the study area may limit the ability to resolve the correlation. The distribution of heat and permeability values for geothermal systems ≥130°C could be used to develop discriminator lines more strongly sloping toward the x-axis (black lines, Fig. M-28). However, based on model results, this slope is considered somewhat aggressive, and a more conservative compromise between the logistic regression result and the distribution of higher temperature geothermal systems was adopted (magenta line, Fig. M-28) to produce the overall Fairway prediction (Fig. M-29).

Errors: Error was propagated from the respective component errors of the heat model and combined permeability model using the sum of the component error variances weighted by the square of their respective scaling factors. As with previous error images, relative errors tend to be higher where values of the index are low (Fig. M-30).

Given the key role that the fairway prediction plays in this research project, the nature of these errors was evaluated further. In Figure M-31, the magnitude of the error is used to scale the magnitude of anomalous values of the fairway index. Specifically, on this map, the mean of the fairway scores is subtracted from the fairway score at each point on the map to generate an anomaly "difference", which is then divided by the error at the same point, to produce a map analogous to z-scores, in which higher numbers represent progressively greater confidence that the fairway value is greater than the mean fairway value. On this map, colors above yellow represent anomaly differences that are greater than the error estimate, and colors of orange and above represent anomaly differences that are greater than twice the error estimate. Of key importance is the fact that the distribution of warmer colors mimics all of the areas of greater prospectivity defined by the Fairway Map itself, thus indicating that the anomalous areas on the fairway map have statistical significance.

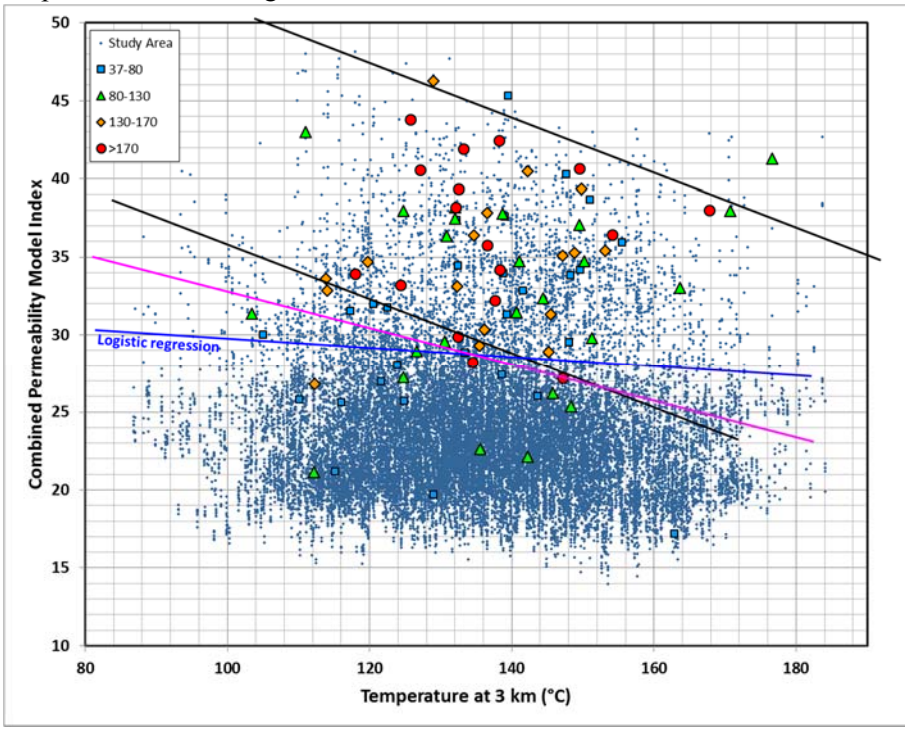

Figure M-28. Heat source model (Fig. P-4) versus the combined permeability model (Fig. M-26) and the benchmarks. The benchmarks score well on the combined permeability model index, and the primary benchmarks (>130°C) score more consistently high compared to lower temperature benchmarks. See text for explanation of blue, black, and magenta lines.

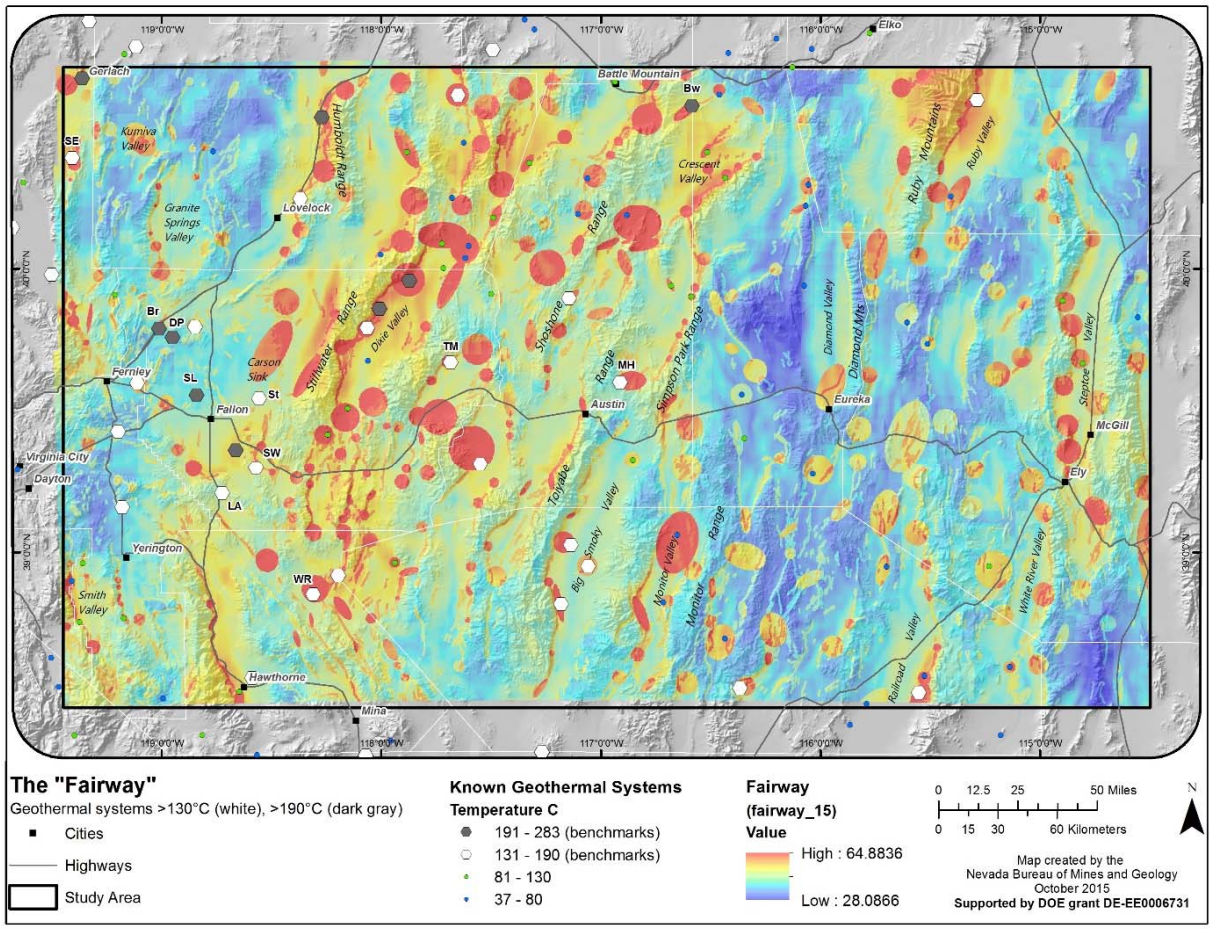

Figure M-29. The play fairway model of the study area.

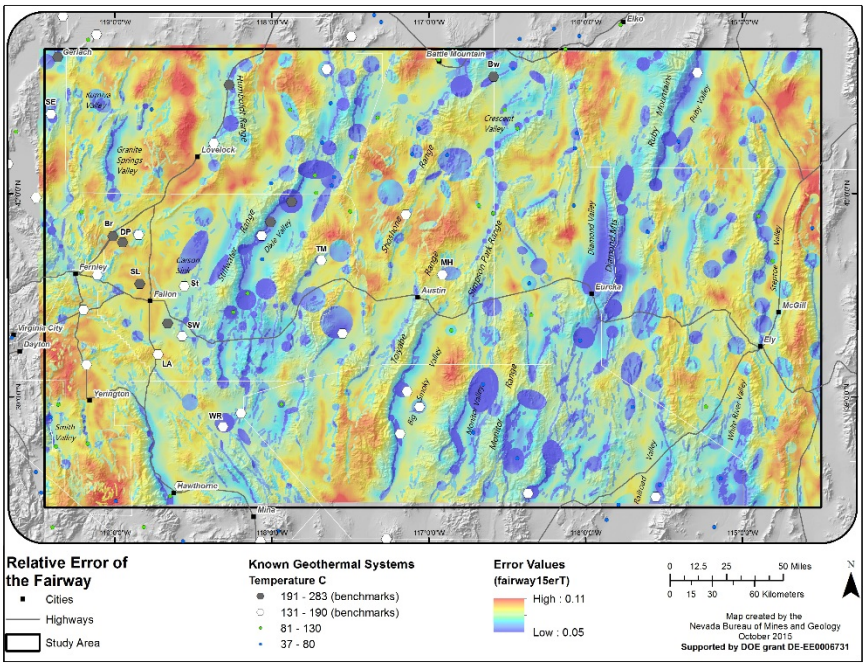

Figure M-30. Relative error of the play fairway.

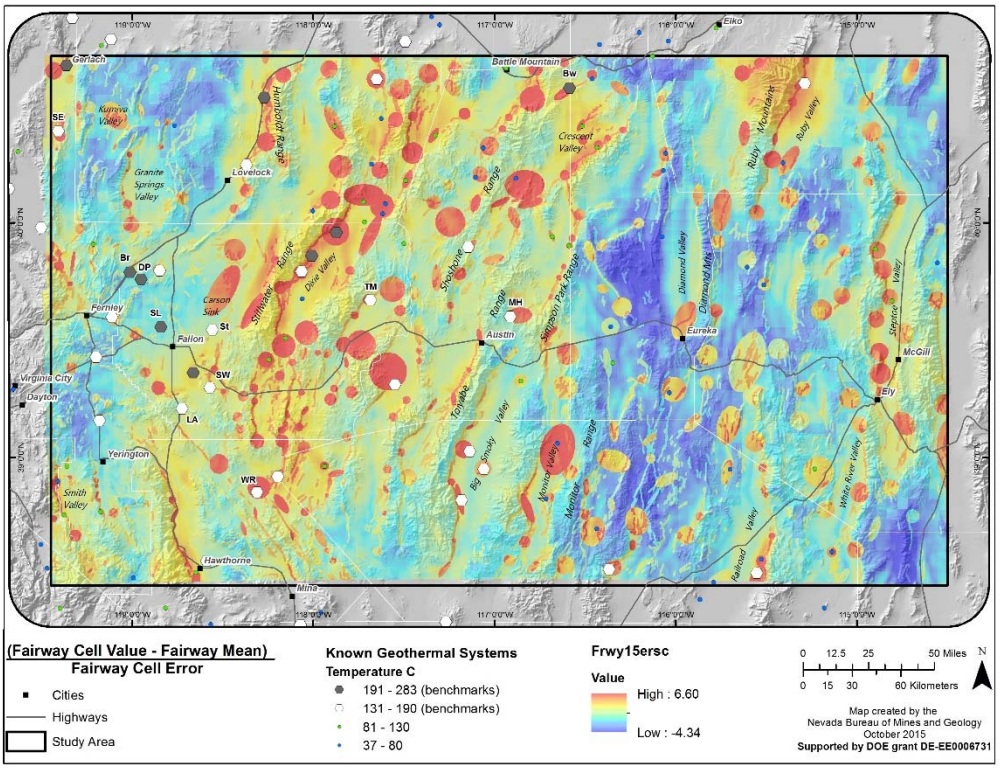

Figure M-31. Anomaly magnitude of the play fairway model (Fig. M-29) normalized by the estimated error. The mean of the fairway scores is subtracted from the fairway score at each point on the map to generate an anomaly "difference", which is then divided by the error at the same point, to produce a map analogous to z-scores, in which higher numbers represent progressively greater confidence that the fairway value is greater than the mean fairway value. On this map, colors above yellow represent anomaly differences that are greater than the error estimate, and colors of orange and above represent anomaly differences that are greater than twice the error estimate.

Direct Evidence

Direct evidence includes information directly pertinent to whether or not geothermal activity is present at a particular location of a fairway. Analogous to oil seeps or successful oil wells in petroleum exploration, or discovery of outcrops with visible gold mineralization in metals exploration, in geothermal exploration such evidence can include thermal springs, associated favorable geothermometry, high temperatures at shallow depths in wells, or as an extreme case, successful flow tests in geothermal wells. In such cases, favorable direct evidence transitions into the addition of another geothermal benchmark (known geothermal system).

The fairway model represents the key product of this research, because it helps define the terrain where additional geothermal exploration is justified. However, it is important not to ignore direct evidence of geothermal activity, as it can have a significant impact on ranking green-field exploration targets and selecting specific fairway targets for further work.

In this project, direct evidence includes spring temperatures and geothermometry and well temperatures and geothermometry. Generally, the higher the spring temperature and the higher the spring or well geothermometer estimate, the greater the index of direct evidence. Based on familiarity with thermal spring and well geochemistry, the project geochemist (Dr. Lisa Shevenell) has assigned a scale of probabilities (probability of occurrence of a geothermal system ≥130°C) based on spring temperatures and spring and well geothermometry (Table P-6).

Well temperatures are more challenging to assess, because temperature tends to increase with depth, so that on average, the deeper the well, the higher the temperature. To address this issue, for each well, a temperature anomaly was calculated which is the difference between the measured temperature and the "background" temperature. The "background" temperature is based on the regional temperature gradient and the depth of the well. The regional temperature gradient was extracted from the regional heat map (which models the temperature at a depth of 3 km), by subtracting an estimated average surface temperature of 18°C from the temperature at 3 km and dividing by a depth of 3 km. Well temperature anomalies were then converted to probabilities using the same conversions used for spring temperatures (Table P-6), after subtracting 18°C from the spring temperature scale.

Layer Construction: The direct evidence probabilities assigned to each spring and well were loaded into ArcGIS. For each cell in the model, a 2 km-radius search was made for the highest well and spring probability, which was then assigned to the grid cell. Compared to the fairway map, which defines broad areas of interest, the direct evidence map defines very localized anomalies, consistent with the point-based nature of springs and available wells (Fig. M-32).

Errors: Errors associated with direct evidence are of two types. The first type is related to the accuracy of a temperature measurement and the ability of a geothermometer to represent current temperature conditions at depth. These errors have been estimated and are documented in Task 3 of this report.

A second error type is associated with the probability assignments for spring and well temperatures and geothermometers (Task 3, Table P-6). This error is much less well constrained and consequently is greater than the first error type because probability assignments are qualitative in nature, and because relatively high probabilities are commonly involved. Probability assignments are based on qualitative experience that links temperature and geothermometer anomalies to the likelihood of occurrence of a geothermal system. In this project, in lieu of more quantitative data, error associated with probability assignment was assumed to equal 25% of the magnitude of the direct evidence probability (relative error of 25%), though it could be higher in some cases. Because these errors are considered greater than errors associated with direct measurement and geothermometry, they dominate the error estimate, and the direct measurement errors were not directly employed.

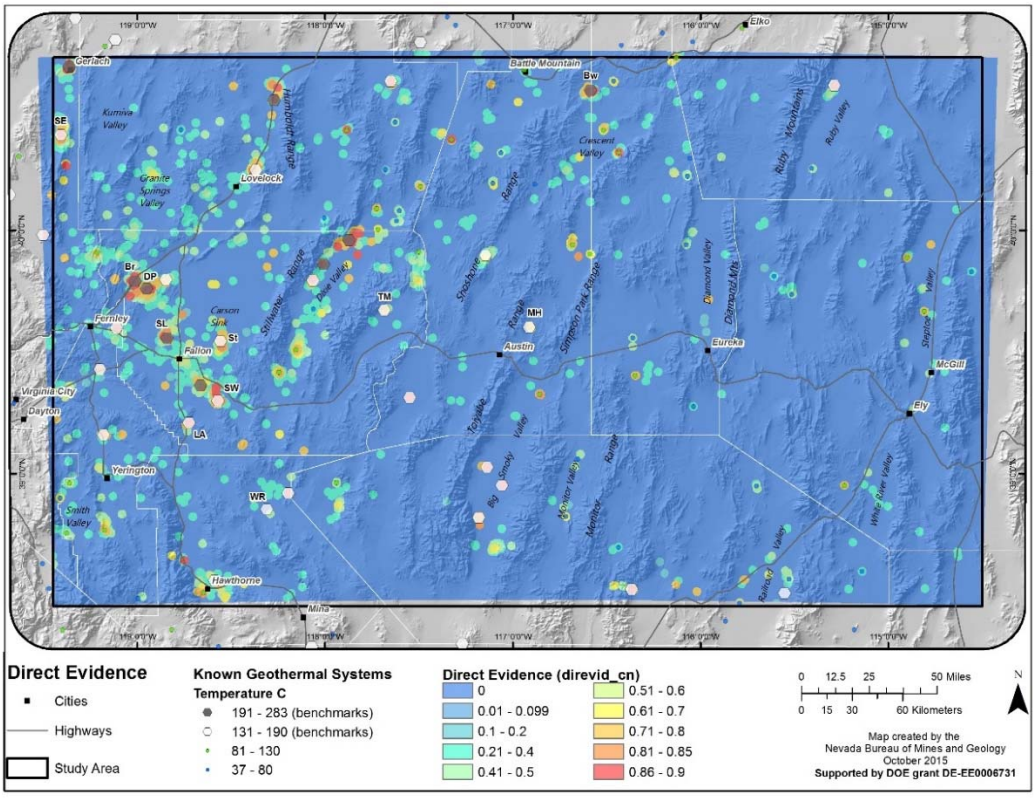

Figure M-32. Direct evidence of geothermal activity in the study area.

Overall Favorability Model

A more complete measure of geothermal favorability can be provided by combining the fairway model with the direct evidence model. Integration of these two layers is challenging because they exist at different probability scales and units. The fairway model is not scaled in terms of probability (but is a measure of favorability) and predicts broad regions of dispersed favorability, whereas the direct evidence model is expressed in terms of probability, and those probabilities can be high, but very localized. A Bayesian-based weights-of-evidence equation was used to combine the fairway and direct evidence models in probability space, after each model was converted to equivalent "weight-space".

Step 1: Weight conversion of fairway model: Multiple weights of evidence were calculated for the fairway model using weights-of-evidence statistics and the primary 34 geothermal benchmarks (≥130°C geothermal systems). Estimation of the multiple weights was an iterative process, beginning with binary cumulative-descending weights-of-evidence, followed by categorical weights-of-evidence, and then followed by reclassification into groups (bins) of statistically significant categorical weights ranging from low to high (Fig. M-33). Note that the statistical weights (approaching and exceeding +3 and -3) are further evidence that the fairway model is doing a good job modeling the benchmarks. The red linear line segments in Figure M-33 were used to scale the weights smoothly across the range of fairway scores.

Step 2: Weight conversion of the direct evidence model: The probabilities in the direct evidence model were converted to equivalent weights by estimating the amount of weight necessary to change a given probability from the prior probability to the probability contained in the direct evidence model. This was done using the standard weights-of-evidence probability equation with a prior probability equal to the number of ≥130°C geothermal systems in the study area (34) multiplied by the assumed area of each geothermal system (9 km^2), divided by the total area of the study.

Step 3: Combination of the fairway and direct evidence models: After conversion of both layers into weight-space, they were combined into an overall model using the Bayesian statistics-based weights-of-evidence equation (Bonham-Carter, 1996), in which the predicted probability, expressed as a "posterior logit", is the sum of the weights of each layer for each grid cell and the equivalent weight of the prior probability (prior logit).

Results: The resulting favorability model (Fig. M-34) is characterized by local areas of high probability surrounded by broad areas of lower probability. This is a natural result of superposition of locally high probabilities from anomalous springs and wells on top of a regional fairway favorability map.

Errors: The error estimate of the favorability model (Fig. M-35) is qualitative in nature because probability assignments in the direct evidence model are qualitative. The relative error of the direct evidence layer (assumed equal to 0.25) was combined with the relative error from the fairway model (Fig. M-30) using a sum-of-variance form of equation in which the two relative errors were weighted by the squares of their respective proportions of weights that they supplied on a grid cell-by-grid cell basis. Relative errors are highest where direct evidence predominates in the favorability model, as evidenced by red colors corresponding to well and spring point data (Fig. M-35).

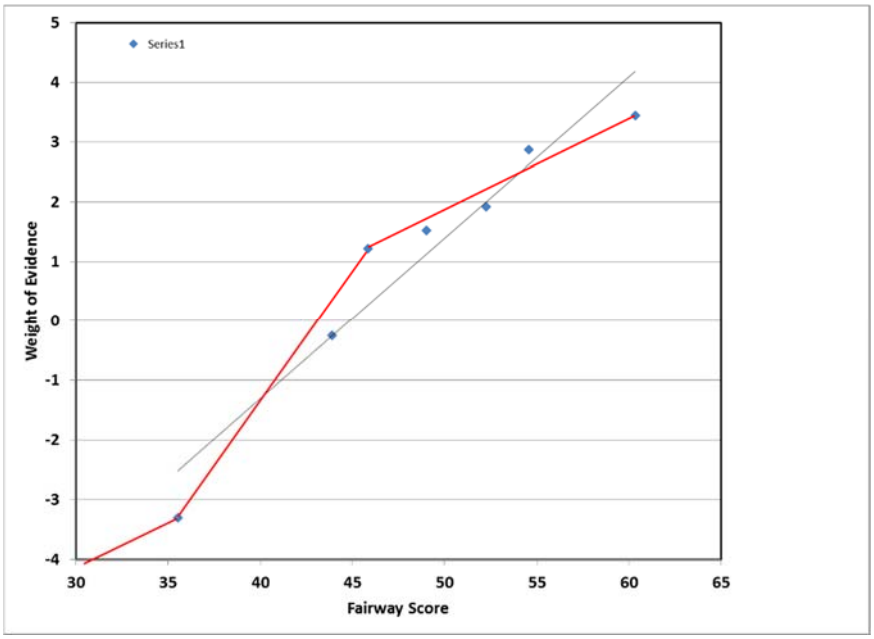

Figure M-33. Multiple categorical weights of evidence for the play fairway using the primary (>130 °C) benchmarks. The black line is a best-fit line using all weights. The red line segments, which represent a tighter fit to the data with different trends for positive and negative weights, were used in the modeling.

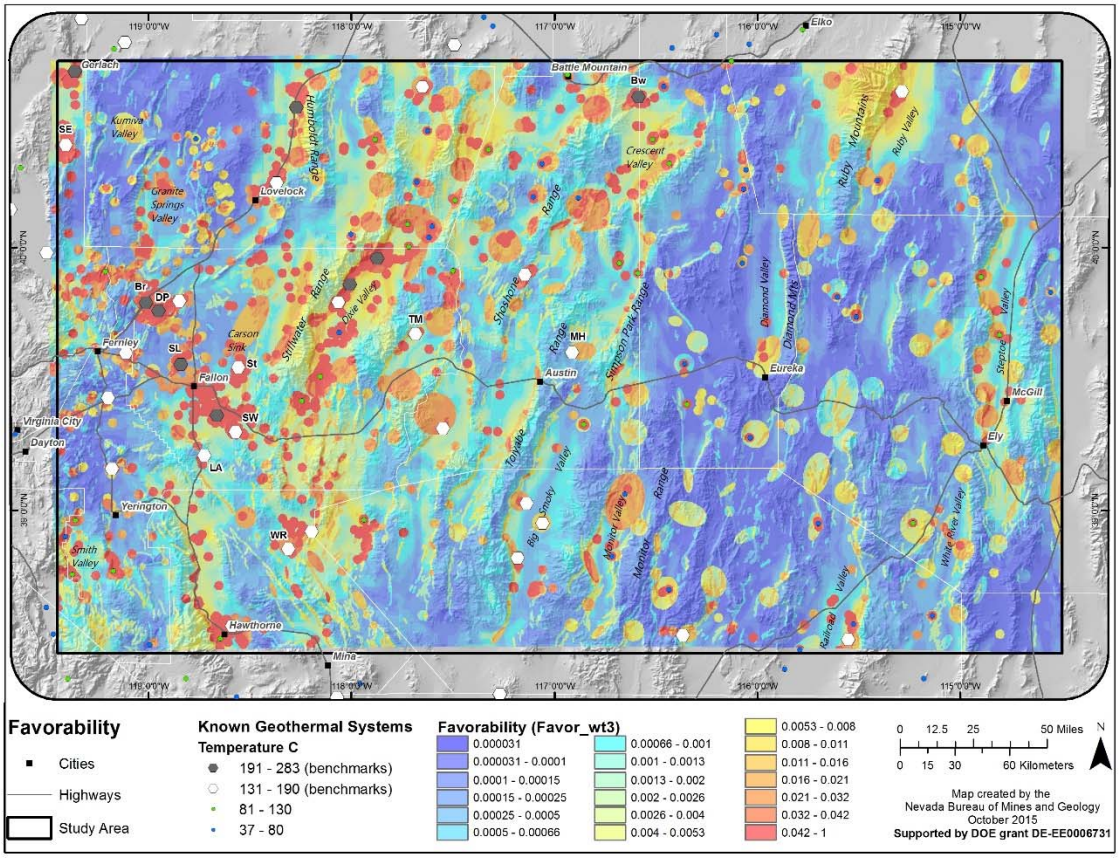

Figure 34. The favorability model generated by combination of the play fairway model (Fig. M-29) with the direct evidence model (Fig. M-32).

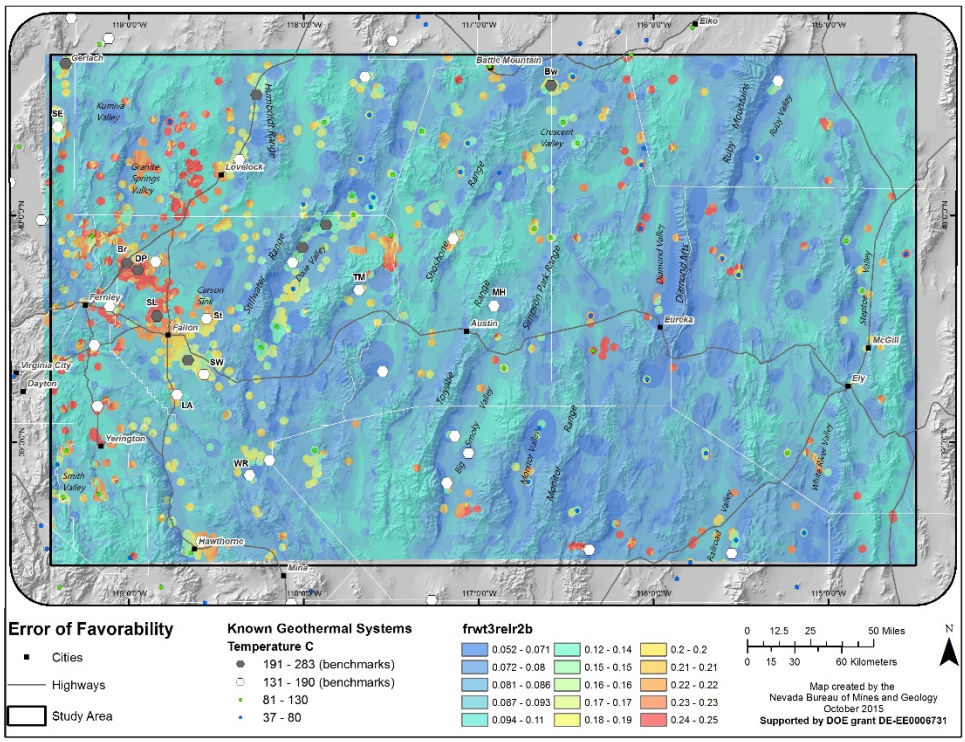

Figure M-35. Relative error analysis of the overall favorability model.

Degree-of-Exploration

The degree-of-exploration model incorporates two types of information. The first type of information assesses the ability of a geothermal system to remain blind without active surface thermal manifestations, and the second type of information considers the thoroughness of past geothermal exploration efforts.

Blindness factors incorporated into the model include depth to the water table, the distribution of Quaternary playa deposits and young alluvium, and the distribution of the carbonate aquifer. Hot springs are less likely to form where the water table is deep. A depth-to-water table map had earlier been prepared by the Desert Research Institute, Reno Nevada and used in earlier geothermal assessments (Coolbaugh et al., 2007). Hot springs are also less likely to form where impermeable near-surface sediments are present. Near-surface impermeable sediments include playa deposits and young alluvium; the distributions of these units were taken from the Nevada state geologic map (Crafford, 2007). Thermal springs are also less likely to form where shallow permeable aquifers are present, because these aquifers can capture and entrain thermal fluids rising from depth. The distribution of the carbonate aquifer in eastern Nevada used in this study was derived from Prudic et al. (1995).

Degree-of-exploration assignments were made in the following manner (Tables M-2, M-3). An initial degree-of-exploration assignment was based on water table depth, with the degree-of-exploration decreasing with increasing depth. This factor was then modified by multiplication by a "near-surface sediment" factor and a "carbonate aquifer" factor (Table M-2) to generate an overall degree-of-exploration estimate based on "blindness".

A drill-hole (well)-related degree-of-exploration was created using all known wells with temperature measurements. The compilation of this well database is documented in Task 3 above. Degree-of-exploration assignments were made to this well database depending on the depth of the hole and the depth of the water table (see Table M-3). Degree-of-exploration increases with well depth, but it significantly decreases if the well is shallower than the water table depth (Table M-3). A 2-km-radius of influence was

used for the well data, and the maximum "degree-of-exploration" from wells within that radius was assigned to each grid cell.

Table M-2. Water depth, surficial sediments, and carbonate aquifer factors for geothermal systems to be blind and affect degree of exploration.

	base operating factor		add-on		add-on
Water_Depth	Water_Depth_Factor	Playa_Seds	Playa_Seds_Factor	Carb_Aquifer	Carb_Factor
0-6 m	0.50	Playa	0.50	Yes	0.85
6-15 m	0.40	Quat alluv	0.75	No	1.00
15-30 m	0.30	Older alluv	0.80		
30-60 m	0.20	Other	1.00		
>60 m	0.10				

Table M-3. Drill-hole depth versus water table depth for calculating well-related degree of exploration.

Hole Depth	0-6 m	6-15 m	15-30 m	30-60 m	>60 m
0-6 m depth	**0.20**	0.20	0.10	0.05	0.05
6-15 m depth	0.30	**0.25**	0.20	0.10	0.05
15-30 m depth	0.35	0.35	**0.30**	0.15	0.05
30-60 m depth	0.40	0.40	0.40	**0.35**	0.15
60-200 m depth	0.50	0.50	0.50	0.50	**0.40**
200-500 m depth	0.65	0.65	0.65	0.65	0.65
500-1000 m depth	0.75	0.75	0.75	0.75	0.75
1-2 km depth	0.85	0.85	0.85	0.85	0.85
>2 km depth	0.90	0.90	0.90	0.90	0.90

The degree-of-blindness layer was then integrated with the "degree-of-blindness" layer using the following formula: DofE(total) = 1 – (1-p1)*(1-p2), where p1 and p2 represent the degrees of exploration associated with "blindness" and "wells", respectively. This form of equation was used because it is considered that an end result of "thermal evidence is observed" could occur either by the action of drilling a well, or by certain combinations of geology and water table that allow a thermal spring to form, and that drilling of wells and thermal springs are not related to each other.

The degree-of-exploration model is shown in Figure M-36. Degree-of-exploration is high where deep wells are present (with temperature data), low in valley bottoms with playa sediments, and very low in ranges where water tables are deep.

Errors: Errors associated with degree-of-exploration are particularly difficult to estimate because input into the degree-of-exploration is inherently qualitative in nature. Errors have been assigned at 25% of the degree-of-exploration value, but they could be higher.

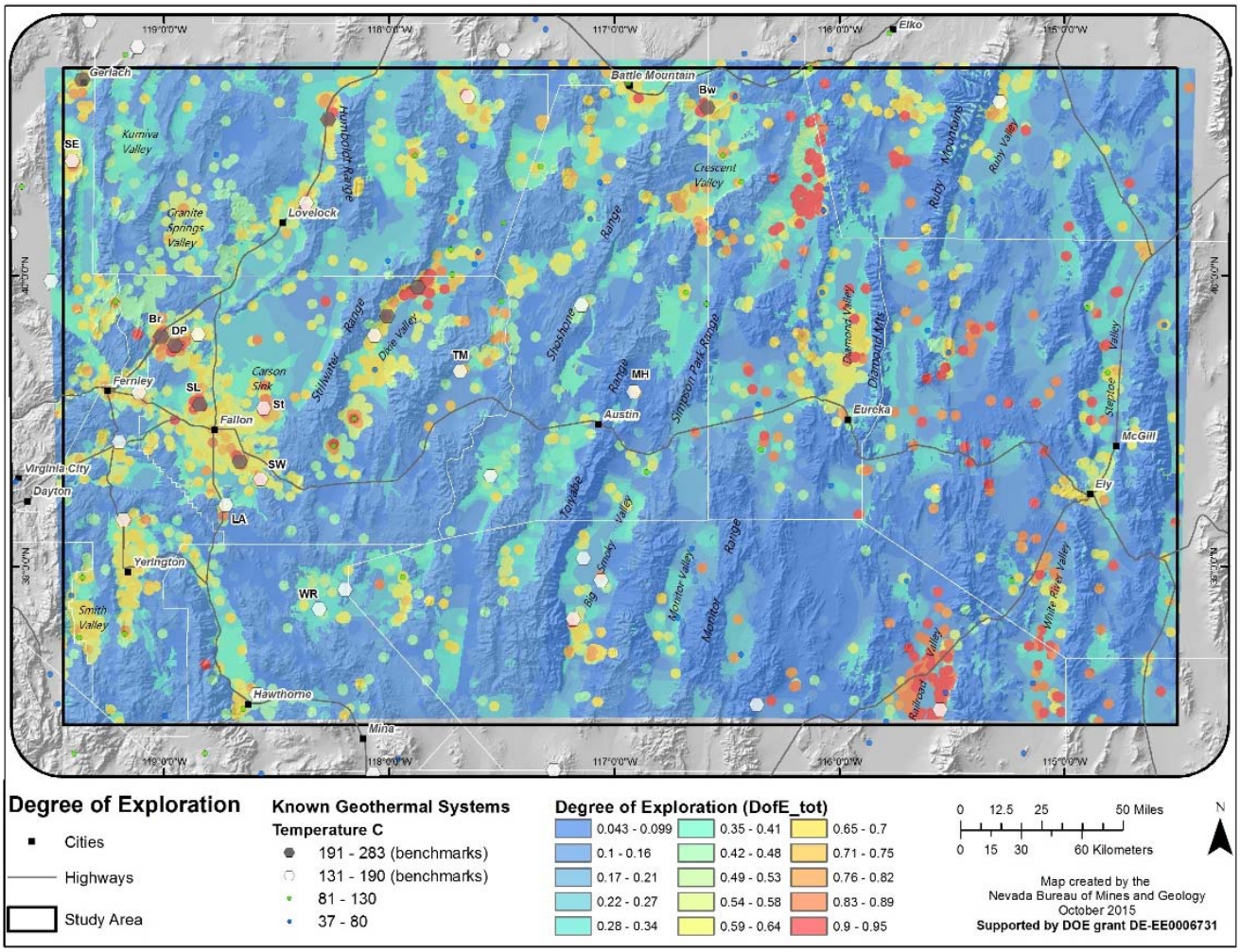

Figure M-36. Degree of exploration within the study area.

Exploration Opportunities Map

An overall "exploration opportunities" map was created by multiplying the favorability model by the inverse of the degree-of-exploration (1 – Degree of Exploration). Conceptually, a discovery is most likely to occur where the geothermal fairway is good and where direct evidence exists, and where the degree-of-blindness is high and/or where wells are not present.

Results: The exploration opportunities model (Fig M-37) reveals a complex interplay between high probabilities associated with direct evidence, high degrees of exploration related to well-drilling, and the regional fairway model.

Errors: Error-estimation of the exploration opportunities map is complicated by the subjective nature of degree-of-exploration. The error estimate can be potentially misleading because the error estimate itself is subject to a high degree of error. Errors were estimated by weighting the relative errors of the two input layers (the favorability model and [1 minus the degree of exploration]) in a variance formula. The weights of each error equal the squares of the magnitude of the respective grid cell values for the two corresponding probability grids. The output error model (Fig. M-38) contains values ranging from 11% to 25% relative error, but the results should be treated with caution because the uncertainty of the errors is high, and actual errors could be higher than shown. In any case, the results suggest that errors are generally higher in mountain ranges where exploration data are limited.

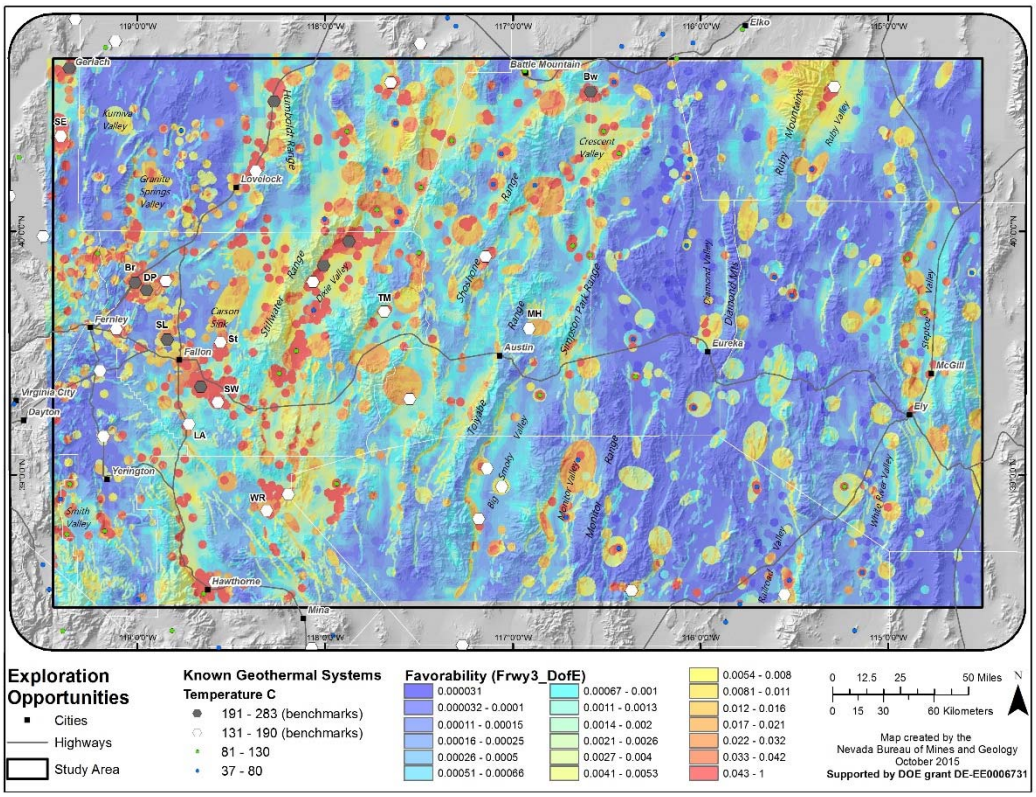

Figure M-37. Model of exploration opportunities after combining the degree-of-exploration (Fig. M-36) with the favorability model (Fig. M-34).

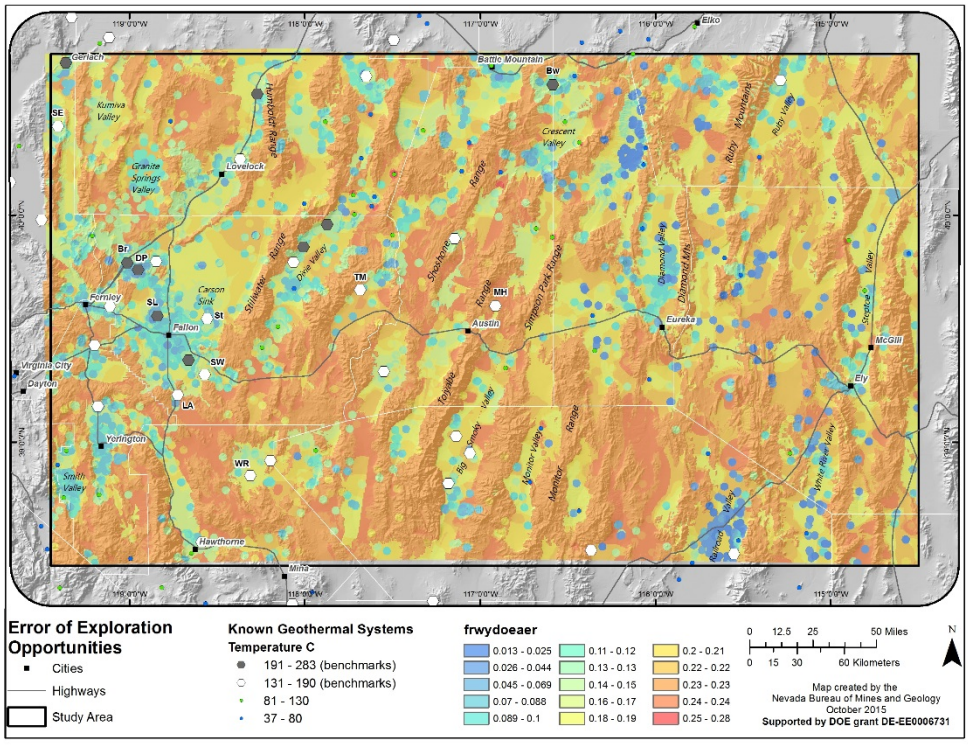

Figure M-38. Relative error estimated for the exploration opportunities model.

RESULTS AND DISCUSSION

All major goals and objectives of this project were accomplished (as shown in the milestone Table P-1) and generated results with significant implications for discovering new commercial-grade geothermal resources in the Great Basin region. As described below, our models predict abundant and diverse favorable locations for geothermal activity across the region. A primary outcome of this project is clearly a target-rich model. The results of each major component of the play fairway model are discussed below and synthesized in the "fairway" and "exploration opportunities" sections, which address the final favorability maps.

Local Permeability

The ~375 identified favorable structural settings within study area form the basis for estimating local permeability (Fig. M-5). The scores for each setting were based on the type of structure, certainty and quality of the structure, Quaternary slip rates, age of Quaternary faulting, and slip and dilation tendency (Table M-1). The age of faulting and type of structure carry the greatest weights. Local permeability scores ranged from 0.7 to 10.0. Most of the highest scores (6.1 to 10.0) reside in a NNE-trending belt from the Hawthorne area on the southwest to the Battle Mountain area on the northeast, which includes the Wild Rose, Dixie Valley, and Beowawe geothermal fields and roughly follows the central Nevada seismic belt, a region that has experienced several large historical earthquakes (Bell et al., 2004; Caskey et al., 2004). The largest cluster of favorable settings with relatively low values (0.7-4.0) occupies the southeastern part of the study area to the southwest of Ely. Elsewhere, most of the favorable settings have moderate values ranging from 4.1 to 6.0. The belts of higher and lower values for the favorable structural settings primarily reflect the regional differences in the ages and slip rates on Quaternary faults across the region (Figs. M-14B and M-16C).

The large number of favorable structural settings clearly indicates that the region contains abundant favorable locations for geothermal activity. In fact, the identified favorable structural settings cover ~12% of the region. Of the 375 identified settings, 34 or nearly 10% of the total are known to host high enthalpy systems (≥130^{o}C). Of these 34 systems, 14 (41%) have been developed into geothermal power plants. These relations suggest a huge untapped potential for additional geothermal development in the region.

Regional Permeability

As previously described, the regional permeability model incorporates six parameters, with earthquake distribution, age of Quaternary faults (recency), slip rates on Quaternary faults, geodetic strain rate, and horizontal gravity gradient having equally large weights in the overall weighted sum (Fig. M-1). Slip and dilation tendency has a much lower weight due to its poor correlation with the 34 benchmarks. Values of regional permeability range from 1.05 to 21.85. The largest area of highest values defines a NNE-trending belt stretching from the Hawthorne area through Dixie Valley, and ending northward between Lovelock and Battle Mountain (Fig. M-24). The high values in this region generally reflect high geodetic strain rates (includes post-seismic relaxation component of the strain field), recently active Quaternary faults, abundant historical earthquakes, and steep horizontal gravity gradients. Areas of high regional permeability also occur outside this belt, generally following many of the major range-front Quaternary faults in the region. These include: 1) Smith Valley along the southwest margin of the study area, 2) Gerlach, Granite Springs Valley (Shawave Range), and the Humboldt Range in the northwest; 3) Shoshone Range, Crescent Valley, Ruby Mountains, and Diamond Mountains in the north-central to northeastern areas; 4) Big Smoky and Monitor Valleys in the south-central part of the area; and 5) Railroad Valley, White River Valley, and parts of Steptoe Valley in the southeast. The high values in these areas generally reflect relatively active Quaternary faults and steep gravity gradients.

The regional permeability map provides a measure of geothermal potential at a broader scale than that given by the local permeability model, which is important because much of the region has not been mapped at a sufficient scale to define local permeability. Small step-overs, terminations of small to moderate size normal faults, many fault intersections, and even some accommodation zones may not be detectable with the available data. This is especially true for some of the larger basins in the region, such as the Carson Sink, where Quaternary basin-fill sediments may cover Quaternary faults. It is important to note that major pluvial lakes, such as Lake Lahontan in the western part of the study area, essentially reset the Quaternary fault clocks at ~13 ka by eroding and burying all Pleistocene fault scarps in the affected basins. Because many of the fault zones within this region have earthquake cycles on the order of tens of thousands of years, the extent of Quaternary faults is probably far greater than that reflected by surface ruptures. Thus, the regional permeability map provides a means of capturing some of the geothermal potential in these areas and may help to both facilitate and induce green-field exploration.

It is also noteworthy that several of the major parameters in this group essentially track crustal deformation through time, from the past ~20 years (geodetic strain), to ~150 years (earthquakes), and to ~2.6 Ma (Quaternary slip rates). The transient nature of strain is evident by comparing the distribution of earthquakes with the geodetic and earthquake data. For example, the Ruby Mountains and Diamond Valley areas in the northeastern part of the study area have experienced relatively high strain in the Quaternary, as shown on the maps of the age and slip rates of Quaternary faults, but have very low values with respect to earthquakes and geodetic strain. Similarly, the Toiyabe Range in central Nevada has relatively high slip rates but little recent faulting. (Figs. M-14B and M-16C). Further evidence that geothermal potential remains high in these areas even though historic strain and earthquake rates are low is provided by the presence of a high-temperature geothermal system along the eastern Ruby Mountains range-front (Sulphur Hot Springs), with an estimated subsurface temperature based on geothermometry of 182°C. Conversely, the Fallon and Carson Sink areas have experienced high rates of recent faulting but relatively low longer-term slip rates. The transient nature of strain across this region may be good for geothermal activity, as within the span of hundreds of thousands of years, the loci of deformation may migrate from one area to another, helping to keep fractures open on a regional scale and thus persevering the Great Basin region as a world-class geothermal province.

Combined Permeability

The combined permeability model merges the regional, intermediate, and local permeability maps with relative weights 1.0x, 0.5x, and 1.0 x, respectively (Fig. M-1). Values of combined permeability range from 13.9 to 49.75, with the benchmark values averaging 35.38. The region of highest values trends NNE from near Hawthorne to just west of Battle Mountain (Fig. M-26), following a similar trend to regional permeability. Outside of this area, curvilinear belts of high values along major Quaternary normal faults are punctuated by even higher values in individual favorable structural settings along discontinuities or at the ends of such faults, as well as within some broader accommodation zones. Loci for particularly high values in these areas include 1) the west flank of the northern Shoshone Range, 2) Crescent Valley, 3) central Monitor Valley (Diana Punchbowl area), 4) northern Ruby Mountains, and 5) southern Diamond Mountains (among several others). In general, the lowest values are found in the eastern third and northwestern part of the study area. Similar to the local and regional permeability maps, the combined permeability model indicates abundant widespread permeability and numerous geothermal targets in the region. The combined map may provide industry with a template for developing regional exploration programs peppered with more focused studies on individual prospects.

Heat

The temperature map at 3 km shows elevated values in the north-central and northeastern parts of the study area (Fig. P-4). The latter consists of a NNW-trending belt of elevated temperatures extending from near Ely to Elko, encompassing Steptoe Valley and the Ruby Mountains area. Notably, the trend of this belt is oblique to the predominant, more northerly structural grain in that region. In the north-central part of the area, several NNE-trending belts of elevated temperatures occur roughly between Lovelock and Austin and approximately parallel to the dominant structural grain in that area. Interestingly, the Hawthorne to Dixie Valley area, which stands out so prominently in the models of local and regional permeability, does not correspond to a particularly warm region at 3 km depth. Additionally, notable cool spots lie in the northwestern part of the study area, in a northwest-trending belt along the Walker Lane, and in a northerly trending zone centered on the town of Eureka. The Eureka cool spot may be associated with the eastern Nevada carbonate aquifer, whereas the cooler area along the Walker Lane may reflect the influence of strike-slip faulting and associated shear strain, which is less favorable to fluid flow than regional extension and dilation along normal faults, which dominate most of the region.

The "Fairway"

The fairway model merges combined permeability and heat into the primary predictive data product of this study (Fig. M-1). The ability of the fairway to correctly forecast areas of elevated geothermal potential is verified by examination of the scatter plot of Figure M-28, in which the slope of the magenta line provides the discrimination index used in the fairway model. The association of the benchmarks with high fairway scores is further documented with weights-of-evidence in Figure M-33, and is illustrated with comparative histograms of the distribution of benchmark scores vs fairway scores for the entire study area in Figure R-1. The statistical significance of the results is mapped with an error-normalized anomaly map in Figure M-31.

The fairway model provides a dynamic prediction over multiple scales, including local, intermediate, and regional. Fairway values range from a low of ~28 to near 65, with the 34 high-temperature (≥130°C) benchmarks yielding an average of 51.37. Several prominent fairway belts stand out in this model. Foremost among these is a NNE-trending, ~100 km wide belt extending from near the southwestern corner of the study area, through Dixie Valley, and to the Lovelock-Battle Mountain area. This area contains a plethora of highly ranked favorable structural settings set against a backdrop of relatively high regional permeability. It is not surprising that Dixie Valley resides in the heart of this belt, as it appears to occupy the eye of a perfect storm for geothermal favorability. This includes favorable values for recency of faulting, slip rates, geodetic strain rates, gravity gradients, earthquakes, and slip-dilation tendency. It is noteworthy, however, that this belt is at least 100 km wide, with many highly prospective areas present outside of Dixie Valley. We are curious if the crustal-scale low resistivity anomaly rooted beneath Dixie Valley (Wannamaker et al., 2007, 2013) may, in three dimensions, actually follow much of this belt. Notably, McGinness Hills lies near or possibly just beyond the eastern margin of this belt, implying that many additional systems comparable to McGinness Hills and Dixie Valley may lie hidden beneath this promising region.

Several other prominent fairways populate the study area outside of the conspicuous Dixie Valley area. In the west, these include the Gerlach area in the northwest corner of the region and a transtensional area along the right-lateral Pyramid Lake fault directly northwest of Fernley. In the east, apparent fairways occur in Monitor Valley, Ruby Mountains, and Steptoe Valley, as well as along scattered Quaternary faults with obvious step-overs, fault intersections, and fault terminations.

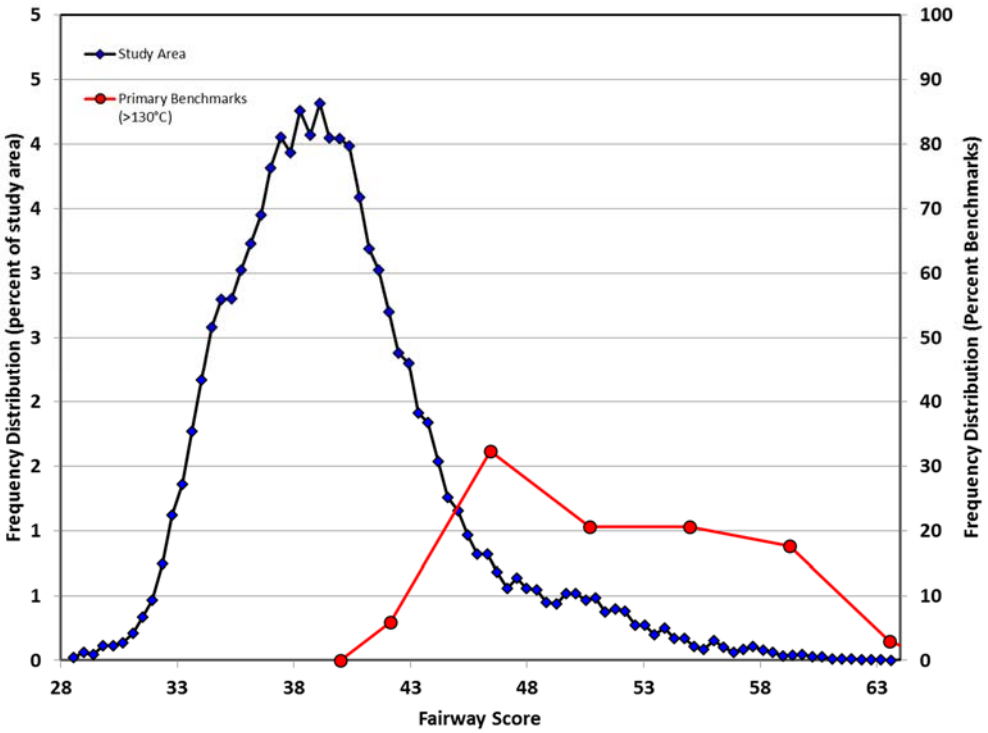

Figure R-1. Distribution of play fairway scores for the primary benchmark (>130°C) systems compared to scores for the study area as a whole.

Direct Evidence Model

The approach of using a fairway model to explore for undiscovered geothermal systems involves a process of field studies to search for specific evidence of geothermal activity. Many exploration tools can be used to help obtain this direct evidence (e.g., geologic mapping, fluid geochemical sampling, temperature surveys, and geophysical surveys). Importantly, much information of this nature has already been gathered in previous studies, and it should be used and leveraged in order to make the exploration process as efficient as possible. Some of this "direct evidence" includes temperature measurements of springs and wells, as well as geothermometry-based temperature estimates of fluids from springs and wells. This information was synthesized to produce the "direct evidence model", which estimates the probability of occurrence of a geothermal system based on temperature and geochemical evidence and nicely complements the fairway model.

The direct evidence model is characterized by a number of small, but relatively high probability locations that correspond to springs and wells. These locations can be compared to the locations of recognized geothermal systems (Fig. M-32). Areas where geothermal systems are not yet recognized, but where the direct evidence is elevated, can be good places to search for geothermal activity. If higher temperatures are present (e.g., ≥130°C) and the geothermal gradient is elevated, it is more likely that a convective systems is nearby. Examples visible on Figure 32 include two locations along the eastern margin of the northern the Carson Sink, two locations ~60 km southeast of Fallon, a location in northern Steptoe Valley, and several locations along the southern margin of the study area to the west of Railroad Valley. Geothermal activity is more likely in cases where the hot wells correspond to favorable structural settings and high values of local permeability (e.g., northern Carson Sink).

Overall Favorability Model

The evaluation of direct evidence can be potentially optimized by integrating it more completely with information used to build the fairway map. This has been done with the overall favorability model, which represents the intersection in probability space of the fairway model with the direct evidence model (Figs. M-1 and M-34).

The favorability map is challenging to interpret in some ways, because it contains point-localized probabilities of relatively high geothermal potential (e.g., thermal springs) combined with broad areas of lower probability (but still significantly elevated over background values) associated with the fairway. In some cases, the red and orange spots on Fig. M-34 correspond to areas currently being explored, or areas where past exploration has not encountered viable geothermal activity. But in other cases, these hot spots represent areas with minimal exploration work.

Caution should be used in interpreting the favorability map, because probability assignments for the direct evidence layer are qualitative in nature and estimation errors can be significant. It nevertheless provides a useful conceptual tool for evaluating the fairway model in the context of direct evidence, and also serves as a quick reference tool for where direct temperature or geochemical evidence of geothermal activity exists. But in some cases, it may be more practical and effective to use the fairway model and the direct evidence model side-by-side, to consider where to conduct additional exploration on a case-by-case basis based on the results of both models.

Degree of Exploration

In some locations, the fairway map (Fig. M-29) highlights areas for which geothermal potential is high, but where past exploration, including drilling, has been extensive. Conversely, some favorable areas are more likely to hide blind geothermal systems than others, based on the geological environments in which they occur. Deep water tables, near-surface clay-rich sediments, and shallow aquifers facilitate the concealment of geothermal activity by making it more difficult for thermal fluids to reach the surface. The degree-of-exploration (Fig. M-36) systematically models the potential for "concealment" and the degree to which past drilling has explored for geothermal activity.

On a stand-alone basis, the degree-of-exploration model is a useful tool for evaluating which portions of the play fairway have received the least exploration and where potential for concealment is high. The most extensive areas of "low" degree-of-exploration correspond to mountain ranges, where water tables (exclusive of local, perched water tables) are commonly deep and where little geothermal drilling has been conducted. Low degrees of exploration are also modeled in some valleys, including the region between the Carson Sink and Buena Vista Valley, several valleys to the east and southeast of Fallon, and a number of valleys in the southeastern part of the study area.

Exploration Opportunities

Similar to direct evidence, the degree-of-exploration model can be fused with the favorability model to predict more comprehensively which portions of the study area have the best potential to host undiscovered blind geothermal systems. This has been done with the *Exploration Opportunities Map* of Figure M-37, which integrates the play fairway model with both the degree-of-exploration and direct evidence models. This map predicts good opportunities in a diverse set of environments throughout the study area. A broad belt of opportunity extends from the Walker Lane northeastward through Dixie Valley and Battle Mountain, but good potential is also modeled in a number of other locations, including the Ruby Mountains area, Steptoe Valley, and Hawthorne. It is important to recognize that some areas are characterized by relatively high degrees of exploration, but with encouraging results in terms of temperature, such as Dixie Valley, whereas other areas, such as the Ruby Mountains, also have high modeled exploration opportunity, but have seen much less exploration work. Thus the character and nature of follow-up exploration would be

radically different from one place (e.g., deep geophysics and drilling in some parts of Dixie Valley) to another (e.g. initial surface mapping and reconnaissance around the Ruby Mountains) on the opportunities map.

The exploration opportunity map should be evaluated with caution, because errors of estimation are high due to the qualitative nature of input data from the degree-of-exploration and direct evidence models. For example, deep drilling information used in the model includes temperatures, but it has not been possible to include data on permeability. Consequently, in some situations, it may be more effective to compare the play fairway model side by side with the degree-of-exploration model and the direct evidence model to identify sites for additional exploration on a case-by-case basis. We further note that exploration opportunities are also dependent on the land status of prospective areas (e.g., public vs. private; wilderness vs. multi-use, etc.) and distance to and capacity on the nearest transmission corridors. Thus, multiple geologic and socio-economic factors actually affect the exploration opportunities in any given area. Our Phase II plan in which we propose to focus detailed studies on several of the most highly prospective areas identified herein takes these factors into account.

Outcomes

The models of the fairway and exploration opportunities produced in this study are a significant improvement over previous models because compared to previous efforts they 1) incorporate a greater dimensionality of input data (more diversity of input layers), 2) use more up-to-date and more accurate data (e.g., earthquakes and Quaternary fault slip and age data), and 3) mark the first comprehensive inclusion of structural data, which is critical given its key role in controlling systems in the Great Basin region and elsewhere. The modeled fairway clearly provides a dynamic prediction over multiple scales (local, intermediate, and regional scales), and it is a very target-rich model, with numerous favorable locations identified in a variety of settings throughout the study area. As evidenced by the scatter plot of structure versus temperature (Figs. M-3 and M-4), multiple weights on evidence on benchmarks (Fig. M-33), a relative error map (Fig. M-30), and frequency of distribution graphs (Fig. R-1), the model predicts geothermal potential well.

Thus, the models of the play fairway and exploration opportunities have significant potential for stimulating green-field exploration and new geothermal development in the Great Basin region. Subsequent phases of this project would help to ensure this effect, as detailed studies of representative highly prospective areas followed by drilling to confirm discovery of new resources are needed to ultimately prove out the methodology incorporated into the favorability and fairway models. In the following section, we provide a comprehensive description of Phase II recommendations.

We also plan to disseminate the results of this study promptly not only through the DOE-GDR and NGDS, but also through a series of peer reviewed publications. In these publications, we will provide alternative weighting factors for some of the key components as a means of showing the effects of certain interpretations. The data can clearly be combined in a plurality of ways, and a single map is only one possible realization of the data synthesis, as noted by the Technical Monitoring Team during the Q-3 review of this project. The beauty of having an ArcGIS platform for this project is that we can easily show different maps with different weighting factors. However, we limited discussion of such alternatives herein due to the length of this report. We are also considering development of a web application with an interactive interface that contains all the data sets to allow users to combine various factors in different ways depending on local conditions as well as interpretive biases. This will require, however, a significant investment of time and therefore awaits subsequent phases of this project.

We should also note that the favorability maps developed in this study for the extensional to transtensional Great Basin region will have broad applications, because most of the world's major geothermal regions occur in similar settings, such as the Taupo Volcanic Zone in New Zealand, western Turkey, East Africa, Iceland, and even some magmatic arcs (e.g., southern Cascades, parts of Japan, Trans-Mexican volcanic belt). Although some of the key geothermal parameters identified in this study may not directly apply to different tectonic settings (e.g., some magmatic arcs), the methodology in terms of

statistically combining multiple parameters and developing applicable statistical analyses to weight such factors will likely have applications to geothermal favorability maps for any tectonic setting.

PHASE II RECOMMENDATIONS

Introduction

The combination of high heat flow and active extensional to transtensional tectonism has generated one of the largest geothermal provinces on Earth within the Great Basin region of the western U.S. Estimates suggest that the geothermal potential in this region approaches 30,000 MW (Williams et al., 2007), but existing geothermal power plants currently generate less than 600 MW. Thus, this region appears to host a vast under-developed renewable energy resource that may be vital to the nation's future. Further, excellent exposures make this region a superb natural laboratory for analyses of geothermal systems, while easy accessibility, favorable land status, multiple transmission corridors, and supportive local and state governments provide an advantageous socio-economic environment for significant new development.

Our detailed geothermal potential maps (fairway and favorability maps) generated in Phase I of this project (Figs. M-29 and M-34) for the central part of the Great Basin and the relative rankings of ~375 favorable settings for geothermal activity, as provided by the map and associated databases, lay the groundwork for planned activities in Phase II. This map combines ~10 parameters into a comprehensive, statistically based assessment of regional-scale permeability, local permeability, and heat to gauge geothermal potential across the region. It therefore provides a roadmap for future exploration in this region, as it identifies many promising areas for geothermal development. This includes heretofore unrecognized favorable areas for blind geothermal resources, as well as relative rankings for known undeveloped geothermal systems (blind and non-blind). In addition, Phase I provided rankings for benchmarks in the region, including 34 systems with documented temperatures >130^{o}C. This allows for direct comparison of any prospective areas with the "benchmark" values for regional permeability, local permeability, heat, and as many as 10 individual parameters that define the fundamental components of a viable geothermal system.

Objectives

The main objective of Phase II will be to conduct detailed studies of several (3 to 5 total) promising areas for potential high-temperature (>130^{o}C), commercial-grade geothermal systems, as identified on the detailed geothermal potential map produced in Phase I. Selected systems will include a combination of known but little explored systems, as well as previously unrecognized, potential blind systems. Potential blind systems will comprise at least half of the selected areas for detailed study. All selected systems will have a favorable land status and lie proximal (within ~20 km) to existing or planned transmission corridors. Table Ph-1 provides a list of 24 of the most highly prospective, potential systems, from which we will select the final areas for detailed study after thorough review in the first quarter (Q1) of Phase II.

Approach

Targeted improvements to baseline technology in Phase II of this project include a systematic multi-disciplinary approach to both the selection of the most highly prospective areas and the subsequent detailed analysis of these areas, including incorporation of innovative technologies and statistical analyses for selection of drilling sites in a potential Phase III. An initial down-select process from ~24 excellent prospects (Table Ph-1) to a final set of 3 to 5 superior sites for detailed studies will dominate the first quarter activities. Figure Ph-1 shows the locations of these highly prospective areas overlain on the fairway model. All of these areas have high fairway and favorability values relative to the benchmarks (Fig. Ph-2).

Efforts in Q1 (weather permitting) will include acquisition of new data (e.g., reconnaissance geologic mapping geochemical sampling, and shallow temperature surveys), as well as additional statistical analyses

to refine the rankings of each site relative to established benchmarks in the region. Once the final sites are selected (latter part of Q1-early Q2), we will quickly deploy our team in a comprehensive coordinated effort involving integrated geologic, geochemical, and geophysical studies. Specific tasks are described in the Planned Activities below. Key steps in Phase II include: 1) assembling existing data into an ArcGIS data platform for each of the 3-5 detailed study areas; 2) acquisition of new geologic, geochemical, and geophysical field data and for incorporation into the data platform; 3) development of 3D conceptual models that will elucidate the subsurface structural and stratigraphic framework and provide a basis for detailed statistical analysis for selection of the best drilling sites; and 4) selection of drilling sites for Phase III based on quantitative statistical analysis and 3D modeling of the study areas and comparison with developed systems in the region.

Table Ph-1. Promising Areas Identified in Phase I

Site #	Location	Fairway Maximum	Favorability Maximum	Blind	Land Status	Transmission	Exploration	Seismic
	Western Nevada							
1	Fox Range-Granite Range	58.8309	0.9945	Yes	BLM	Yes	No	Yes
2	Kumiva Valley	50.9146	0.0205	Yes	BLM	Yes	No	No
3	Granite Springs Valley	56.3636	0.8823	Yes	BLM	Yes	Minor	Yes
4	North Carson Sink	55.6970	0.9608	Yes	BLM/Navy	Yes	No	Yes
5	Humboldt Range-W flank	59.5117	0.9808	Yes/No	BLM	Yes	Some areas	Yes
6	East Buena Vista Valley	60.1265	0.9902	Yes/No	BLM	Yes	Some areas	Yes
7	Grass Valley-Leach HS	58.4821	0.9937	Yes/No	BLM	Yes	Some areas	Yes
8	Sou Hills	59.5074	0.9724	No	BLM	Yes	No	Yes
9	South Gabbs Valley	59.3359	0.0704	Yes	BLM	Yes	Minor	No
10	Wellington Hills	56.7140	0.0483	Yes	BLM	*Yes?*	No	No
	Central Nevada							
11	South Buffalo Valley	59.6741	0.9877	Yes/No	BLM	Yes	No	No
12	N Shoshone Range -N Reese River	61.3773	0.8936	Yes/No	BLM	Yes	No	Yes
13	N. Carico Valley Red Mountain	58.0123	0.7975	Yes	BLM	Yes	No	No
14	Crescent Valley	64.8707	0.9970	Yes/No	BLM	Yes	Some areas	Yes
15	Peterson	57.8555	0.9936	No	BLM	Yes	No	No
16	Big Smoky Valley	56.0568	0.9849	No	BLM	Yes	Some areas	No
17	SE Simpson Park Range-NW Monitor Range	58.0255	0.7065	Yes	BLM	Yes	No	Minor
18	Hot Creek Ranch	51.7774	0.9831	No	BLM	No	Minor	Yes
	Eastern Nevada							
19	Starr Valley	64.8836	0.1504	Yes	BLM	Yes	Minor	Yes
20	Ruby Valley	63.6571	0.9970	No	BLM	No	No	Yes
21	South Diamond Valley	52.5292	0.4926	Yes	BLM	Yes	No	Minor
22	Butte Valley	55.8983	0.0429	Yes	BLM	Yes	No	Yes
23	Steptoe Valley	58.6060	0.9641	Yes/No	BLM	Yes	Minor	Yes
24	Williams	51.6833	0.9232	No	BLM	Yes	No	Minor

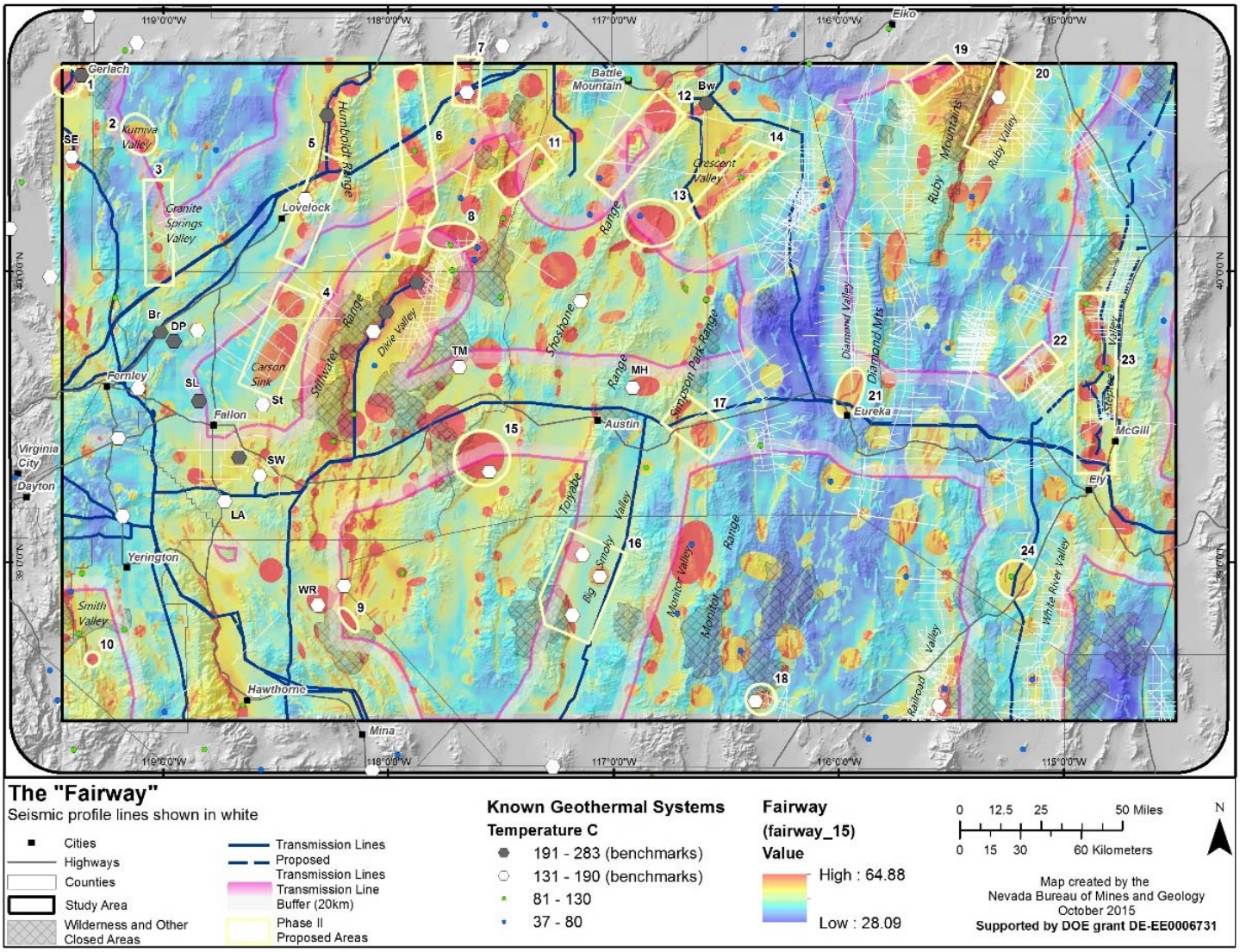

Figure Ph-1. Nominated highly prospective areas (yellow polygons) for initial analysis in Phase II shown relative to electrical transmission corridors. Note that maps for some of the smaller transmission corridors were not available and thus are not shown on this map. Numbers adjacent to the polygons refer to site descriptions in Table Ph-1. After an initial analysis and down-selection, 3 to 5 areas will be chosen for detailed studies in Phase II. Thin white lines show available seismic reflection profiles from SEI. Lines from the Carson Sink and Steptoe basin were purchased and analyzed in Phase 1. Available profiles within highly prospective areas include those from Granite Springs Valley, northern Dixie Valley, Grass Valley, Butte Valley, and Ruby Valley.

Outcomes

Our detailed analyses of several highly prospective areas is the second step in a systematic multi-phase effort to discover new, commercial-grade geothermal resources within the Great Basin region through integrated geologic, geochemical, and geophysical studies. If successful, this project will validate our methodology in developing the geothermal potential map, constrain the collective geologic-geochemical-geophysical signature of a viable geothermal system, and ultimately provide a means by which to carefully evaluate risk in geothermal exploration of this region. This will help to propel the geothermal industry toward a level on par with other major extractive industries, such as oil and gas. In addition, success would

likely stimulate green-field exploration within the Great Basin and elsewhere, especially since the methodology and techniques employed in this study can be directly applied to other extensional to transtensional settings, as well as other tectonic regimes. We envision developing a template that encompasses assessment of geothermal potential at both the regional scale (e.g., the Phase I geothermal potential map) and in much greater detail at the local scale (e.g., Phase II detailed studies). The regional scale map allows for identification of multiple potential fairways (i.e., promising prospects), whereas the detailed local studies provide 3D conceptualization of geothermal systems in those potential fairways and develops methodologies for selection of specific drilling targets into the permeable sweet spots of an individual system. Validation will occur with the Phase III drilling of these sites. Success will also provide a catalyst to produce a geothermal potential map for the entire Great Basin region, as well as other geothermal provinces within the U.S. and elsewhere. Additionally, once the risks in developing blind geothermal systems are significantly reduced, the vast geothermal potential of the Great Basin region can more easily be unleashed. A successful play fairway approach in this region, together with expected advances in EGS technologies in the coming years through projects such as FORGE, may ultimately propel geothermal energy into a sizeable contributor to our nation's energy budget.

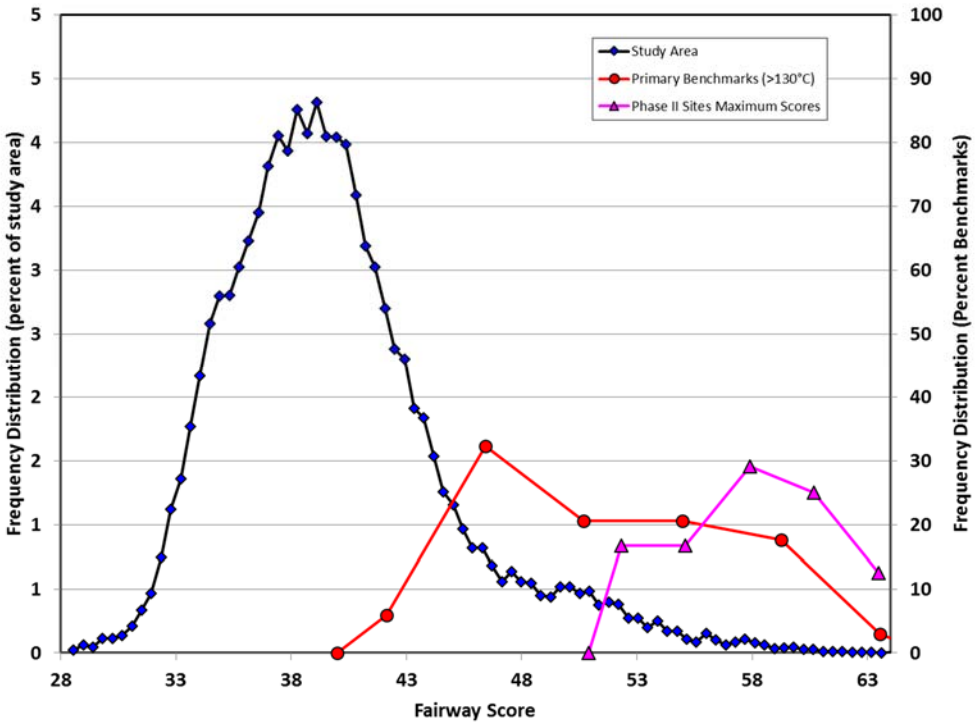

Figure Ph-2. Distribution of play fairway scores for the primary benchmark (>130°C) systems compared to scores for the study area as a whole (blue) and the maximum values within the 24 sites selected areas for analysis in Phase II (purple).

Planned Activities

The work plan for Phase II will involve systematic detailed analysis of several (3 to 5) of the highest ranking areas for geothermal potential within the study area (Fig. Ph-1), as defined on the geothermal potential maps (fairway and favorability maps) produced in Phase I. This 17-month project will progress through: 1) initial review of the most promising prospects (Table Ph-1), 2) down-selecting areas for detailed studies, 3) detailed geologic, geochemical, and geophysical investigations, 4) data synthesis, 5) selection of well targets for a potential Phase III, and 6) final report writing and publication. Our general work flow

is outlined in Figure Ph-3. The major goals and tasks for discrete quarterly performance periods are outlined below and shown in Table Ph-2.

- Quarter 1 – Assessment of ~24 of the most promising areas through review of available geologic, geochemical, and geophysical data, detailed land status, and field reconnaissance. If winter weather precludes access to some areas, this work may continue into the early part of Q2. This will be followed by down-selecting to 3 to 5 of the most highly prospective areas for comprehensive detailed investigations and new data acquisition.
- Quarters 2, 3, and 4 – Detailed studies and data acquisition for 3 to 5 areas, including geologic mapping, analysis of Quaternary faults, LiDAR acquisition, geochemical investigations, gravity surveys, purchase and analysis of available seismic reflection data, geodetic studies aimed at elucidating post-seismic effects on geothermal activity, shallow temperature surveys, and soil gas surveys. A data platform will be built to house the multiple data sets for each study area.
- Quarter 5 – Data synthesis, interpretations, and modeling, including slip and dilation tendency analysis, thermal modeling, and 3D modeling.
- Quarter 6 – Final interpretations, report writing, ranking of areas studied in detail, and selection of targets for drilling in a potential Phase III. Additionally, all data sets will be uploaded to the DOE-GDR.

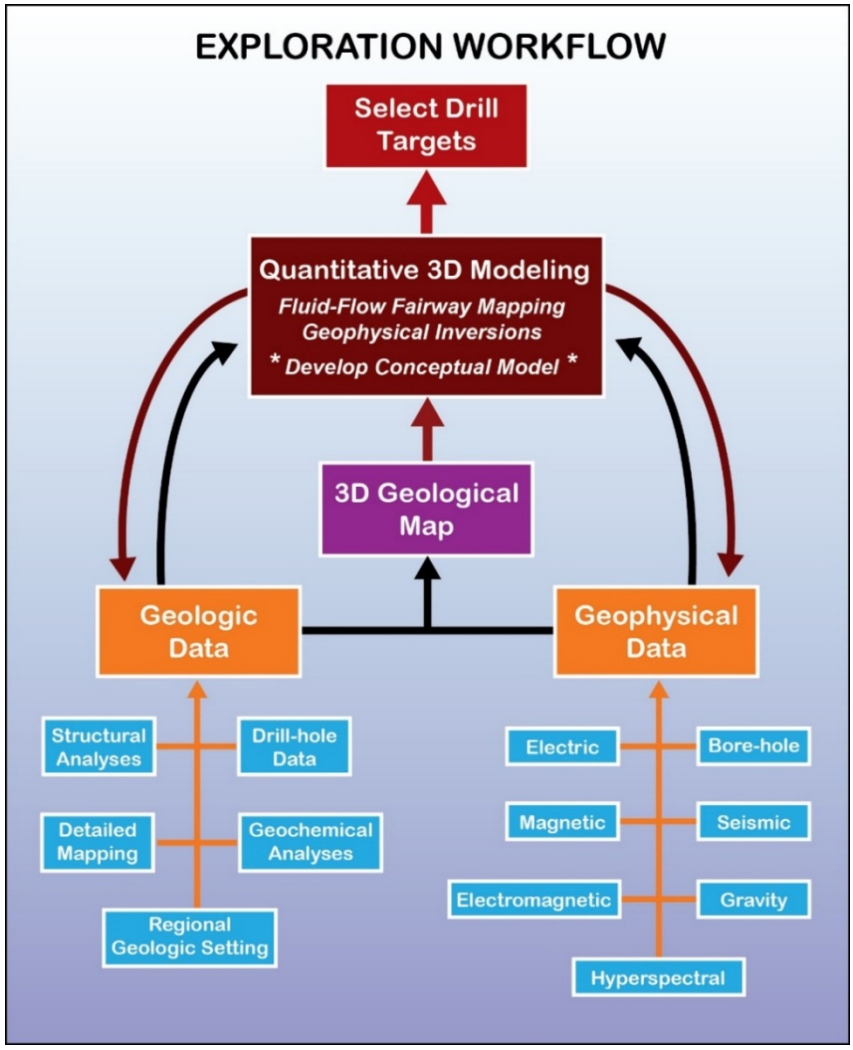

Figure Ph-3. General work flow for Phase II detailed studies (from Hinz et al., 2013). Note that all data types may not be available in some areas.

Table Ph-2. Project Timeline for Proposed Tasks

Task	Q1	Q2	Q3	Q4	Q5	Q6
1. Select Final Sites for Detailed Study						
2. Geologic Studies						
3. LiDAR acquisition						
4. Geochemical Studies						
5. Gravity Surveys						
6. Seismic Reflection Analysis						
7. MT Survey						
8. Geodetic Studies						
9. Shallow Temperature Surveys						
10. Soil Gas Surveys						
11. Slip and Dilation Tendency Analysis						
12. 3D Modeling						
13. Thermal Modeling						
14. Selection of Phase III Drilling Targets						
15. Final Report						

Anticipated timeframe for study extends from January 1, 2016 to June 1, 2017.

Task 1 – Down-Select to Final Sites for Detailed Study (UNR, Atlas, and others): Initially, ~24 of the most promising sites will be reviewed during Q1, and three to five sites will be down-selected for detailed studies. Extensive field reconnaissance, limited shallow temperature measurements in key areas, and review of existing data will be conducted of all 24 sites in the first quarter to define the best prospects for detailed analyses. Criteria employed to select these sites includes: 1) presence of a favorable structural setting; 2) type of structural setting with the more complex settings receiving priority; 3) proximal Quaternary faults with evidence for rupture in the past ~750 ka; 4) quality of exposure, 5) high potential for geothermal development based on overall favorability ranking, land status, and proximity to transmission corridors, and 6) relatively abundant, available geologic and geophysical data. At least half of the selected areas for detailed studies will be blind, with no documented surface manifestations of geothermal activity.

Task 2 – Geologic Studies (UNR and Atlas): The geologic investigations of the final 3 to 5 sites will involve 1) detailed and reconnaissance geologic mapping of bedrock, structure, and Quaternary deposits; 2) detailed mapping of any surface geothermal features, including siliceous sinter, silicified young sediments, carbonate tufa, travertine deposits, areas of warm ground with or without thermal springs, hydrothermal eruption craters, evaporite deposits including sulfate and borate crusts, hydrothermal alteration, and vegetation anomalies; 3) delineation of stratigraphy; 4) selective $^{40}Ar/^{39}Ar$ dating and tephrochronology; 5) analysis of the geometry and kinematics of fault systems; and 6) assessment of the regional stress field. The goals of this work are to a) delineate the structural framework and structural controls on potential geothermal activity in each area, b) elucidate possible relations between stratigraphic units and potential geothermal reservoirs, c) define the overall extent of potential geothermal reservoirs, and d) better constrain the local strain and stress fields. Approximately 20 to 80 km^2 will be mapped at each site, typically at 1:24,000 scale.

Task 3 – LiDAR Acquisition (outside contractor): Accurate, high-resolution elevation data are increasingly important to both applied and basic research in the geosciences. According to a recent study by the USGS, enhanced elevation data could generate as much as $13 billion in benefits each year. Current elevation data for much of the conterminous United States, including Nevada, has a spatial resolution of 10 m (~30 feet) and are on average 30+ years old. The proposed LiDAR data in this project has a resolution of 70 cm, with a cost of ~$335 per square mile.

For each study area, ~50 square miles of LiDAR coverage at Q2 quality (1-3 pulses/m) would be obtained, primarily to delineate the traces of Quaternary faults. This is particularly important for prospective geothermal areas, because the favorable structural settings associated with geothermal activity (e.g., fault terminations, step-overs, and accommodation zones) are characterized by multiple closely-spaced fault strands, each of which has minimal offset compared to the larger, more easily recognized offsets at mid segments. Thus, Quaternary faults in these favorable settings may have minor offsets and be difficult to detect without high-resolution topographic data. The fine-scale patterns of faulting in such areas, including the greatest density of faults or intersections between minor faults, appear to control the locations of geothermal upwellings, as evidenced by detailed studies at several known systems (Bell and Hinz, 2010; Faulds et al., 2010; Hinz et al., 2013; Dering and Faulds, 2012). LiDAR could also reveal obscure paleo-hydrothermal features, such as eroded explosion craters and fissures. Thus, LiDAR is an important tool to apply to the analysis of geothermal systems. The proposed LiDAR coverage will encompass about twice as much area as the proposed detailed geologic mapping in order to provide a broader assessment of Quaternary fault patterns in each area.

Task 4 – Geochemical Investigations (Atlas): Geothermometers will be calculated for all available cold waters in Phase I to provide a first approximation of the location of potentially blind geothermal systems. This data set includes high quality analyses from nearly 600 non-thermal to marginally thermal waters within the study area. Shevenell et al. (2012) noted several areas in Nevada with elevated geothermometer temperatures from cold springs associated with blind systems that were later discovered. The Phase I compiled data will therefore be used to focus our exploration efforts into areas with known anomalous geothermometer temperatures from cold waters. Appendix C includes a map of these point locations within the study area. Multicomponent chemical equilibria will be calculated with data from these cold and warm waters to better assess anomalous geothermometer estimates. Additionally, approximately 20 new water samples at $500/sample will be collected from the detailed study areas. It is anticipated that some of these samples will be collected from currently unknown and previously undocumented wells and springs found during reconnaissance field surveys. These new analyses will be used in conjunction with data collected in Phase I as direct evidence to support the findings from geologic and structural analyses conducted in Phase II.

In addition, if appropriate units are present (e.g., calcite veins and possibly travertine), clumped isotopes may be used to characterize paleofluid temperature and chemistry, possibly through a subcontract to Dr. Katharine Huntington at the University of Washington. This method is based on the preference for molecules with multiple heavy isotopes (e.g., carbonate groups containing both ^{13}C and ^{18}O) to be more abundant than would be expected if all isotopes were randomly distributed. The preference for molecules with ^{13}C-^{18}O "clumps" increases at low temperature, such that measurements of clumping give the temperature of carbonate mineral growth, free from assumptions about the isotopic composition of the fluid from which the mineral grew (Huntington and Lechler, 2015). Combined with concurrent measurements of the carbonate $\delta^{18}O$ value, the temperature information can be used to calculate the $\delta^{18}O$ value of the fluid from which the mineral grew. The modern waters and calcite, as well as any older calcite (e.g., veins), can be used to develop a thermal and chemical history of a hydrothermal system. Travertine mounds may also be utilized in this technique, as samples collected close to vents and from open pools minimize kinetic fractionation effects and can produce reliable temperature estimates (Kele et al., 2015). Sufficient exposures are needed, however, in order for this work to be fruitful, and thus we will utilize this technique only if good exposures of calcite veins and travertine, which can be related to recent geothermal activity, are present at the sites selected for detailed studies. Cost of these analyses ranges from ~$102-118/sample.

Task 5 – Gravity Surveys (Zonge, UGS, and UNR): Gravity surveys are useful in assessment of geothermal areas, because they can provide critical constraints on the locations, geometries, and offsets of subsurface faults. For this study, we will combine new detailed and available regional gravity analysis to support the geologic and structural analysis of our study areas. There is typically a fair amount of public domain regional data in this region. Fill-in and project data can be acquired for about $50 to $100 per

ground station. Older data can typically be integrated, after editing, with new data and re-reduced in a uniform treatment. Thus, it is possible to economically prepare new continuous suitable data coverages to address project scale exploration. Station locations and elevations will be determined using GPS survey equipment. The gravity data will be processed to simple Bouguer values using gravity processing programs. These Bouguer values will be calculated using multiple different densities ranging from 2.00 to 3.00 g/cm^3. Terrain corrections will be also be calculated. Final products will be GIS layers and surface grids of reduced data, regional and residual anomaly separations, total horizontal gradients, first vertical derivatives, and depth to basement maps. In addition to these products, we may generate, for some areas, a total bedrock relief surface that images major faults.

Task 6 – Seismic Reflection Analysis (Hi-Q Geophysical and UNR): Existing 2D seismic reflection profiles cover several areas under consideration for detailed studies in Phase II (Fig. Ph-1). These include some of the higher ranking areas for geothermal potential, such as Granite Springs Valley, Pleasant Valley, northern Dixie Valley, and Ruby Valley. Similar to Phase I, we will obtain ~400 miles of seismic reflection profiles for the areas selected for detailed study to help constrain fault geometries, the overall structural framework, and basin architecture. This will help to define obscure structural relationships along the margins and within the interiors of major basins and thus assist in targeting structural sweet spots for permeability. The profiles will be obtained from Seismic Exchange, Inc. (SEI), in Houston, Texas.

This work will proceed in several phases. The first will involve a review of all seismic reflection data in areas with relatively high geothermal potential to provide additional insight into the size and specific locations of favorable structural settings, particularly within some of the larger basins (e.g., Ruby Valley). This will be helpful in the down-selection process to the final 3 to 5 sites for detailed studies. This review will occur at SEI in Houston and will not involve purchase of any profiles. Once the final sites are selected for detailed study, specific profiles for those areas will then be purchased, taking into account lessons learned during Phase I of this project. For example, most of the profiles available for this region from SEI were acquired during the 1970s and 1980s and thus lack modern digital media. So long as the techniques and velocity models used in the original processing were reasonable, we can convert time to depth based on velocities inferred from gravity-constrained depths to visible lithological boundaries, especially in areas with well control. Profiles that lack such attributes will not be purchased. All profiles will be analyzed using standard techniques to identify faults and lithology. Plots of seismic cross sections will be combined with locations of faults and lithological boundaries known from surface mapping, well information, gravity, and other data sources. These data will provide the basis for the 3D geological models for at least some of the detailed study areas.

We anticipate that this work will progress much more quickly than in Phase I with no delays, because the license with SEI has already been established, the general limitations and potential benefits of these data are well understood. Also, John Queen and PI Faulds developed a good work flow during Phase I, involving interpretation of the profiles by Faulds and review of interpretations, integration with gravity, time to depth conversions, and digitizing of fault and lithologic picks by Queen. All profiles will be purchased in Q2 of Phase II, with interpretations and processing in Q2 and Q3.

Task 7 – MT survey (EGI, University of Utah): Previous experience with geothermal fields in the Great Basin region, such as Dixie Valley and McGinness Hills, has demonstrated that high-enthalpy systems commonly sit at the confluence of deep fluid sources well-imaged by MT, geochemical evidence such as elevated 3He, and geological structures that represent critical stresses and dilatancy (e.g., Wannamaker et al., 2013). For Phase II of this study, we propose to focus new MT acquisition on the most ideal, highly prospective site, which will be identified in Q1. Lateral sampling will be dense enough and of high enough frequencies in our survey to resolve resistivities at both shallow and deeper levels. The MT survey would be coupled with detailed studies of any clay alteration in the area. Sites will average ~$1500 each and will utilize standard techniques and established contractors. At least 50 sites are needed to achieve a well resolved model. Survey design and 3D inversion analysis will also be carried out by EGI. EGI's new, deformable edge finite element 3D algorithm, using a data-space parameter step concept that can handle

million-parameter problems parallelized on a single-box multicore workstation, will be utilized. This is expected to provide the most precise resistivity image possible for MT data. The new model will be compared with those of Dixie Valley, McGinness Hills, and Kumiva Valley. The proposed, detailed MT survey will provide important data with which to compare to other known systems and assess the overall geothermal potential of the selected study area.

Task 8 – Geodetic Studies (UNR): In Phase I of this study, significant progress was made in understanding the role of earthquake transient strain in the maintenance of geothermal systems. We concluded that the transient model had a strong correlation to geothermal activity. The elastic deformation model on which we based these comparisons was built circa 2007 (Hammond et al., 2009), when the data we had at our disposal to measure strain rate was inferior to that available now from new geodetic networks operated by UNR. Thus, in Phase II we would update this deformation model, and continue to take advantage of an ongoing natural experiment on the effect of the decades-long post-earthquake transient strains on geothermal resources in western Nevada. We will comparatively analyze corrected and non-corrected strain rate fields for geothermal favorability, and develop models that explain reasons for such differences. This is particularly relevant to the many highly prospective areas in the western half of the study area, where multiple large earthquakes have occurred in the past ~100 years. At least some of the sites likely to be selected for detailed studies reside in this area (e.g., Sou Hills at northern end of Dixie Valley). In addition to documenting that transient strains are important predictors of geothermal resources, this work will also elucidate the locations for which total strain (measured, i.e. long term plus transient) should be used versus corrected (measured minus transient).

Task 9 – Shallow Temperature Surveys (UNR and Atlas): Shallow temperature surveys have been used for decades to map thermal anomalies associated with geothermal activity. Recently, significant improvements have been made to 2-meter equipment and methodologies; these improvements include the use of all-terrain vehicles (ATVs), digital platinum resistance temperature devices (RTDs), electric hammers powered by portable generators, and tungsten-carbide-tipped hollow steel probes (Coolbaugh et al., 2014). These improvements in efficiency have enabled 2-meter temperature surveys to be moved from a project setting into an early stage green-field exploration setting, and this has resulted in the surveys playing key roles in the discovery of a number of previously unknown geothermal systems. These include Teels Marsh, Rhodes Marsh, and southwest Columbus Marsh in Mineral and Esmeralda Counties, NV, East Hawthorne, Mineral County, NV, Emerson Pass, Washoe County, NV, and at least two other areas identified by private companies whose data remain confidential.

Similar surveys will be conducted as part of Phase II to assess anomalous, shallow temperature regimes at selected sites considered prospective based on Phase I play fairway analysis modeling. Initial reconnaissance surveys will be applied to many sites to help in the down-selection to the final sites for detailed study. For the detailed studies (3 to 5 sites), an average of approximately 30 to 50 probed locations per geothermal area will be deployed to obtain the distribution of shallow temperatures from which assessment of possible upflow and outflow zones can be made. These data will allow calculation of heat loss from the system to provide a first approximation of MW heat loss from the studied sites.

Task 10 – Soil Gas Surveys (LBNL): Subsurface gas compositions can provide strong inferences on the presence, sources, and pathways of upwelling geothermal fluids (e.g., Jolie et al., 2015). The degree of extensional activity combined with structural setting appears to exert a major control on the abundance of mantle-derived ^{3}He carried near-surface in fluids in Basin and Range geothermal systems (Kennedy and van Soest, 2006, 2007). Diagnostic identification of ^{3}He typically requires analysis of samples from active springs, fumaroles, and/or wells. Thus, it may not be straightforward to apply this approach to some of the areas selected for detailed studies in Phase II, particularly for potential blind geothermal systems. We therefore propose utilizing soil CO_2 and the isotopic compositions of soil He and carbon gases as a means of evaluating the geothermal potential of the selected detailed study areas and determining whether such areas are characterized by a deep crustal or upper mantle fluid input along fault zones (e.g., Ballentine et

al., 2002; Pili et al., 2011). Elevated soil gas flux can be detected and mapped in rapid, easy to deploy, essentially non-invasive soil gas surveys. In zones of anomalous flux, soil gas samples will be collected for subsequent isotopic analysis for confirmation of deep fluid sources.

Task 11 – Slip and Dilation Tendency Analysis (LBNL): The purpose of this task is to assess available stress data in order to determine the tendency of faults in the detailed study areas to slip and dilate, which is directly related to the likelihood of such faults to transmit hydrothermal fluids. It is well established that critically stressed fault segments have a relatively high likelihood of acting as fluid flow conduits (Sibson, 1996; Barton et al., 1995, 1998; Morris et al., 1996; Ito and Zoback, 2000; Townsend and Zoback, 2000; Zoback and Townsend, 2001). Thus, the tendency of a fault segment to slip (slip tendency; T_s) (Morris et al., 1996) or to dilate (dilation tendency; T_d) (Ferrill et al., 1999) provides a quantitative indication of the likelihood of certain fault segments to be critically stressed and therefore conduct fluids. Slip and dilation tendency values will be calculated for each fault segment within the detailed study areas, initially based on the surface mapping but ultimately applied to the 3D models. The resulting along-fault and fault-to-fault variation in slip or dilation potential will be a proxy for variations in permeability or fluid flow potential and will be a critical factor in selecting well sites for Phase III.

Task 12 – 3D Modeling (LBNL): To investigate faults and fractures, their potential to channel fluids, and their relationship with the current stress field, it is necessary to quantify and image the surface and subsurface conditions. The proposed modeling will extrapolate the acquired knowledge from surface geology to subsurface structures with a focus on stress-strain conditions along faults and related preferential fluid pathways at depth. The modeling procedures will involve: 1) integration of available geologic and geophysical data into a preliminary 3D structural model; 2) slip and dilation tendency analysis incorporating different failure modes; and 3) adoption of slip/dilation tendency results to the 3D fault model including validation with field-based data. As a result of these modeling studies, potential fluid pathways will be delineated in 3D space by identifying dilational fault segments. Moreover, the spatial extent of potential geothermal reservoirs, as defined by field studies and geophysical data, will be visualized through the 3D model, which may permit estimation of reservoir volumes.

Task 13 – Thermal Modeling (UGS and UNR): The proposed thermal modeling will focus on highly prospective areas within Neogene basins, such as the Steptoe and Ruby basins of eastern Nevada. This work will integrate detailed gravity surveys and available geophysical wireline data from the wells to produce a density-porosity compaction profile with depth in the basins, as well as the vertical resistivity trend and sonic velocity trend in the basin fill (where available data permit). In addition, representative samples of basement lithologies and cuttings from all available wells will be analyzed in order to characterize thermal conductivities within both the basin and underlying basement (maximum 15- 20 measurements). A 3D thermal model would then be carried out utilizing COMSOL software.

Task 14 – Selection of Targets for Phase III Drilling (UNR and entire team): The geologic, geochemical, and geophysical data compiled and acquired in the Phase II detailed studies, together with the 3D modeling, will be synthesized to select specific drilling sites for temperature-gradient holes in Phase III. The most critical components in this selection will be the detailed geologic maps, any observed soil-gas anomalies, slip and dilation tendency analysis, thermal modeling, and the 3D models. Co-located dilational fault segments and fault intersections will be given priority in the targeting of well sites. This task will be completed at the end of Phase II after all data sets have been synthesized and thermal and 3D modeling has been completed.

Research Team and Respective Roles

We have assembled an expert team of geoscientists from academia, government labs, and industry that is well qualified to achieve the project objectives. Our team includes experts in structural geology and geologic mapping (Faulds, Siler, and Hinz), geochemistry (Shevenell and Coolbaugh), geophysics (Queen and Wannamaker), geodesy (Hammond and Kreemer), 3D modeling (Siler), geostatistics (Coolbaugh), geothermal play fairway analysis (Siler, Hinz, and Faulds), soil-gas surveys (Kennedy), shallow temperature surveys (Sladek and Coolbaugh), and thermal modeling (Allis).

Similar to Phase I of this project, the Nevada Bureau of Mines and Geology (NBMG) at the University of Nevada, Reno (UNR), is the lead on Phase II, with Dr. James Faulds serving as PI for Phase II. NBMG and UNR have a history of conducting cutting-edge geothermal research, primarily associated with the Great Basin Center for Geothermal Energy. Successes include major contributions to the National Geothermal Data System (Shevenell et al., 2012), a generalized geothermal potential map of the Great Basin (Coolbaugh et al., 2005), evaluating the influence of strain rates on geothermal activity (Blewitt et al., 2003), refining the technique of shallow-temperature surveys (Coolbaugh et al., 2014), and analyses of the structural controls of geothermal systems (Faulds et al., 2010, 2011, 2013; Hinz et al., 2011, 2014b). Faulds' project involving analysis of the structural setting of >400 geothermal systems in the Great Basin (EE0002748) received the 2012 DOE GTP peer-review award. The UNR team has also been instrumental in developing methodology for play-fairway geothermal analysis using integrated detailed mapping, slip and dilation tendency analysis, and 3D modeling (Siler et al., 2012; Siler and Faulds, 2013).

The team for this proposal also includes experts from other highly successful programs, including the Energy and Geoscience Institute (EGI) at the University of Utah (Wannamaker et al., 2013), Utah Geological Survey (Allis et al., 2013), and Lawrence Berkeley National Laboratory. Wannamaker's study of the magnetotelluric signature of geothermal systems received the 2013 DOE GTP peer-review award. We have recently applied our integrated geologic and geophysical approach to developing 3D models and identifying play fairways at producing systems, including Brady's, Tuscarora, Neal, and McGinness Hills. Thus, our team of experts has the expertise and capabilities to address and significantly advance the science of geothermal play fairway analysis. Further, most members of our team have previously collaborated in Phase I of this study, as well as on other major successful projects.

Prior experience and the skills and expertise of key team members are summarized below:

James Faulds, Ph.D., NBMG Director/State Geologist/Professor: Faulds is the lead on this project. With 30 years of experience, he has previously served as PI on several successful DOE projects and was awarded the 2012 DOE GTP best project for cataloging the structural setting of >400 geothermal systems in the Great Basin region. Much of his research has focused on how fault systems initiate and evolve. He has published ~100 papers and dozens of geologic maps. He has made significant contributions to refining geothermal exploration strategies.

Rick Allis, Ph.D., Utah Geological Survey (UGS): Allis has been evaluating geothermal resource potential for >30 years. Recent projects include screening high heat flow regions in the Great Basin region for stratigraphic reservoirs and the FORGE site in Milford, Utah. Allis has been Director of the UGS for 15 years. Previously, he worked for EGI at the University of Utah and in the first part of his career worked for GNS Science at Wairakei, New Zealand. He has evaluated geothermal prospects in many countries around the western margin of the Pacific.

Bridget Ayling, Ph.D., UNR-NBMG: Ayling has over seven years of professional experience in the geothermal sector with Geoscience Australia and EGI at the University of Utah. She has an extensive background in applied geochemistry. She has focused on geothermal resource mapping and reservoir characterisation in regional-scale studies to map geothermal potential in both Australia and the USA. She will join the UNR team in April 2016.

Mark Coolbaugh, Ph.D. ATLAS Geosciences, Inc.: Coolbaugh has 12 years of experience in geothermal research and geothermal exploration in the United States and abroad. Those efforts have led to discovery of several blind geothermal systems. He has published many papers on development and implementation

of quantitative techniques of estimating regional geothermal potential and blind geothermal resources, including statistical uncertainty analyses.

Mark Gwynn, M.S., UGS: Gwynn has been working for the UGS on the geothermal potential of the Great Basin for more than five years. He specializes in the interpretation of bottom hole temperatures from oil exploration wells, estimating the thermal regime from temperature gradients, thermal conductivity measurements, and well log interpretation. His thesis evaluated the tectonic and thermal origins of Medicine Lake volcano.

Bill Hammond, Ph.D., NBMG-UNR: Hammond is an expert in geodetic measurement and modeling of tectonic deformation, using InSAR and GPS. He has 20 years of experience in addressing geophysical problems relating to structure and dynamics of the Earth's lithosphere and is author or co-author on >30 peer-reviewed publications including geothermal resources associated with crustal deformation using geodetic methods. He currently manages field operations for the 370 station MAGNET GPS network (across 5 western states).

Christian Hardwick, M.S., UGS: Hardwick is a geophysicist and Project Geologist at the UGS. He is a part of the Energy and Minerals program and has also been providing geophysical support for the Groundwater, Hazards and Mapping programs at UGS since 2011. Prior to joining the UGS he worked at the Thermal Geophysics Research Lab, University of Utah, where he measured thermal conductivities and wrote computational code in several computer languages. He has participated in geothermal exploration projects in New Zealand, New Mexico and Utah.

Nicholas Hinz, M.S., NBMG-UNR: Hinz has 15 years of experience with regional geologic framework studies and >8 years of experience with geothermal systems. His research has focused on regional studies of Basin and Range tectonics and on dextral shear in the Walker Lane region using detailed geologic mapping, structural analyses of faults and folds, geochronology, and paleomagnetic analyses.

Katharine Huntington, Ph.D., University of Washington: Huntington has 15 years of experience in tectonics and geochemistry research, and pioneered the use of clumped isotopes for investigating fault-fluid interactions. Her publications include the main analytical methods paper for carbonate clumped isotope thermometry, as well as applied studies of paleofluid sources and pathways in exhumed fault systems and the Blue Mountain geothermal field.

B. Mack Kennedy, Ph.D., Lawrence Berkeley National Lab (LBNL): Kennedy is a Geological Staff Scientist at LBNL and is Group Leader for the Center for Isotope Geochemistry and Program Lead for LBNL's DOE Geothermal R&D Program. He has 35 years of experience and ~100 peer reviewed publications related to the application of isotope systematics to sources, geochemical evolution, transport processes, and flow rates of fluids in the crust, with particular emphasis on geothermal systems.

Ryan Libbey, Ph.D. possible post-doctoral position, UNR: Libbey is an experienced geothermal geochemist and geologist who has worked on academic and commercial geothermal projects in New Zealand, Iceland, Guatemala, and Canada. To date, much of his published research has focused on the study of hydrothermal alteration, fluid chemistry, lithogeochemistry, and vectoring upflow in active geothermal environments.

John Queen, Ph.D., President of Hi-Q Geophysical Inc.: Queen is a licensed Professional Geophysicist with >30 years of experience in the geophysical exploration industry. He is an expert in fracture/fault characterization through seismic methods and has published widely on this topic. He has planned, acquired, processed and interpreted seismic surveys for oil-gas, geothermal, and CO2 sequestration, as well as applying electrical methods, gravity, and magnetics.

Lisa Shevenell, Ph.D., President, ATLAS Geosciences, Inc.: Shevenell (Geochemistry, Hydrogeology) has 30 years of experience in various aspects of geothermal resource exploration and assessment, conceptual model development, and data analysis on regional and local scales in geothermal areas. Shevenell has published dozens of papers on geothermal systems and has extensive experience in the sampling and evaluation of fluid geochemical data and geothermometry.

Drew Siler, Ph.D., Lawrence Berkeley National Lab: Siler is a structural geologist with experience studying a variety of conventional and EGS geothermal systems in the western U.S. and Iceland. His specializations include the application of slip and dilation tendency as a proxy for permeability in

geothermal systems, as well as extending geothermal favorability studies into 3D through modeling and geothermal field-scale play-fairway analysis.

Chris Sladek, M.S., UNR: Sladek is a research associate at UNR with ~20 years of experience in geology, geochemistry and geothermal exploration, and >13 years of experience in electronics, electromechanical technology, and instrumentation in R&D environments. He provides technical support for analytical instruments and equipment. He conducts and assists various research projects and student training at the Great Basin Center for Geothermal Energy (GBCGE) at UNR, where he designed and built the equipment and instruments for the shallow 2-meter temperature measurement system pioneered by the GBCGE.

Phil Wannamaker, Ph.D., University of Utah/EGI: He has had a global impact on interpretation of multi-dimensional MT through field surveying, algorithm development, integrative interpretation and publications. He leads an international program of MT/CSAMT field surveying and interpretation with successes in several geothermal areas of the western U.S. Wannamaker has developed 3D inversion tools suited to this project.

Preliminary Budget Information

The preliminary Phase II budgets are shown in Table Ph-3 for both low and high end levels. Brief descriptions of individual budgets for each institution are provided below.

UNR (Faulds, Hinz, Hammond, Kreemer, Sladek, post-doctoral position, one part-time graduate student): Budget covers multiple critical components of the study, including spearheading down-selection of sites for detailed studies, geologic mapping, Quaternary fault studies, purchase of seismic reflection profiles, seismic reflection interpretation, geodetic studies, shallow temperature surveys, data compilation and synthesis into an ArcGIS platform, overall management of the project, uploading of data sets to the GDR, and final reporting. Funds are requested to hire a post-doctoral scholar (possibly Dr. Ryan Libbey) to assist in all aspects of the study, particularly the detailed studies of prospective geothermal fields.

ATLAS Geosciences (Shevenell and Coolbaugh): Budget includes geochemical studies and some aspects of the geologic investigations. Coolbaugh will provide a supporting role in several aspects of Phase II, including conducting field visits and reconnaissance to assist with the early exploration assessment. This will include mapping of any identified surface manifestations indicative of current or past geothermal activity. Coolbaugh will also assist in planning of any shallow temperature surveys. Funds are also allocated for geochemical analyses.

EGI, University of Utah (Wannamaker): Detailed MT survey of the highest priority site, including collection of ~50 MT stations, processing and 3D inversion of data, and synthesis with other data sets to assess geothermal potential.

Hi-Q Geophysical (Queen): Assist in interpretation of seismic reflection profiles and convert time to depth for all analyzed profiles, utilizing available well and gravity data. Digitize interpreted contacts and faults in the profiles to be used as the basis for developing the 3D models

Lawrence Berkeley National Lab (Siler and Kennedy): Slip and dilation tendency analysis, soil gas surveys, and 3D modeling of detailed study areas; may also include some reconnaissance soil gas surveys to facilitate final selection of areas for detailed studies.

LiDAR contractor: Acquire Q2 LiDAR data (~70 cm resolution) for the detailed study areas. Depending on the local geologic framework, ~30 to 50 square miles of data will be acquired for each study area at a cost of ~$335/square mile.

University of Washington (Huntington): Possible clumped isotope geochemistry if appropriate deposits are available for analysis.

Utah Geological Survey (Allis, Gwynn, and Hardwick): Gravity surveys, analysis of core and cuttings, analysis of available geophysical logs from wells, and thermal modeling of one or two highly prospective basins in eastern Nevada (e.g., Steptoe and Ruby basins).

Zonge International, Inc. (Lide, Kratt, and Oppliger): Detailed gravity surveys of 2-3 detailed study areas in the western and central parts of the region. Cost is ~$50 to $100/station depending on local conditions.

Table Ph-3. Proposed Phase II Budget

Team Member	Task	Low End	High End
UNR	Geologic	$270,000	$330,000
Contractor	LiDAR	$25,000	$75,000
Atlas	Geochemistry, geologic	$90,000	$92,000
Zonge, UNR	Gravity	$35,000	$85,000
UNR	Seismic Reflection	$50,000[1]	$50,000[1]
Hi-Q Geophysical	Seismic Reflection	$50,000	$50,000
EGI-University of Utah	MT	--	$125,000[2]
UNR	Geodetic Studies	--	$30,000
UNR	Shallow Temp Surveys	$40,000	$75,000
LBNL	Soil Gas Surveys	$30,000	$60,000
LBNL	Slip-Dilation Tendency Analysis	$5,000	$15,000
LBNL	3D Modeling	$50,000	$60,000
University of Washington	Clumped isotope geochemistry	$10,000[3]	$17,000[3]
Utah Geological Survey	Gravity, Thermal Modeling	$40,000	$80,000
Total	--	**$695,000**	**$1,144,000**

[1]Funds for purchasing of existing seismic reflection profiles from SEI in Houston, Texas. [2]Can delay to potential Phase III if necessary. [3]If good exposures of calcite veins and/or travertine are available.

Project Management and Reporting

Dr. James Faulds at the Nevada Bureau of Mines and Geology (NBMG), University of Nevada (Reno) is the PI and manager of this project. Subcontracts will be established directly after award approval. Immediately after the project begins, a kick-off meeting will be held to organize all team members toward accomplishing project goals. Each team member will have specific roles, some of which overlap. Monthly telecon meetings will be held to review progress, organize new tasks, and discuss results and interpretations. A team meeting is planned at the end of Q1 to review findings and select the 3 to 5 sites for detailed studies. A second team meeting will be held at the end of Q4 to review all data sets compiled and acquired for the detailed study areas, organize final interpretation and processing, and determine the best path forward in merging these data sets into development of the 3D and thermal models. Quarterly reports will be submitted by all team members to the PI-Faulds, who will compile and submit to DOE for the overall project. Decision making will follow the natural work flow of the project, with decisions on individual components made by the task leads. Decisions on overall project objectives will be made by PI-Faulds. Especially critical is the organization of multiple data sets into coherent geodatabases that allow for completion of all milestones and ultimately the 3D models for each site. These data will be organized into GIS databases for the project and DOE. QA-QC will be addressed throughout the project.

Anticipated Permitting Requirements: The MT survey will require permitting through the BLM. Dr. Wannamaker is very experienced in this arena and will follow normal protocol and procedures to secure the necessary permits. All other aspects of the Phase II study do not require permitting.

CATALOG OF SUPPORTING FILES

All supporting data files and model grids are currently being submitted to the National Geothermal Data System through the Geothermal Data Repository and this process will be complete by October 30th, 2015. These files include ArcGIS files, Excel files, CSV files, Adobe Illustrator files, graphics files, text files, and multiple types of grids with supporting metadata. All files that were submitted as part of this project are listed in Appendix D.

TECHNOLOGY TRANSFER ACTIVITIES

Publications

Faulds, J.E., Hinz, N.H., Coolbaugh, M.F., Shevenell, L.A., Siler, D.L., dePolo, C.M., Hammond, W.C., Kreemer, C., Oppliger, G., Wannamaker, P.E., Queen, J.H., and Visser, C.F., 2015, Integrated geologic and geophysical approach for establishing geothermal play fairways and discovering blind geothermal systems in the Great Basin region, western USA: A progress report: Geothermal Resources Council Transactions, v. 39, p. 691-700.

Faulds, J.E., and Hinz, N.H., 2015, Favorable tectonic and structural settings of geothermal systems in the Great Basin region, western USA: Proxies for discovering blind geothermal systems: Proceedings World Geothermal Congress, Melbourne, Australia, 19-25 April 2015, 6 p.

Hinz, N.H., Coolbaugh, M.F, Faulds, J.E., Siler, D.L., and Dering, G.M., 2015, Building the next generation of regional geothermal potential maps: Examples from the Great Basin region, western USA: Proceedings, World Geothermal Congress 2015, Melbourne, Australia.

Sadowski, A.J, and Faulds, J.E., 2015, Structural controls of the Black Warrior blind geothermal system, Washoe-Churchill Counties, Truckee Range, northwestern Nevada, USA: Geothermal Resources Council Transactions, v. 39, p. 573-580.

Siler, D.L., Faulds, J.E., and Hinz, N.H., 2015, Earthquake-related stress concentrations and permeability generation in geothermal systems: Geothermal Resources Council Transactions, v. 39, p. 437-444.

Presentations

Faulds, J.E., invited talk, Nevada is still in hot water: An optimistic view of developing vast geothermal resources in the Great Basin region: Presentation for opening plenary session at Geothermal Resources Council Meeting, Reno, Nevada, September 21, 2015.

Faulds, J.E., invited talk, Geothermal systems: Geologic origins of a vast energy resources: Presentation for congressional briefing sponsored by American Geoscience Institute in Energy from the Earth, Energy-Land-Water Connections Speaker Series, September 15, 2015.

Faulds, J.E., required talk, Discovering Blind Geothermal Systems in the Great Basin Region: An Integrated Geologic and Geophysical Approach for Establishing Geothermal Play Fairways: DOE peer review, Denver, Colorado, May 2015.

Faulds, J.E., invited talk, Why is Nevada in hot water? Tectonic and structural controls on geothermal activity in extensional settings: University of California, Davis, geoscience colloquium series, April 1, 2015.

Faulds, J.E., Why is Nevada in hot water? Geologic setting responsible for Nevada's vast geothermal resources, City of Fallon and Churchill County Breakfast Colloquium, Fallon, Nevada, March 18, 2015.

Faulds, J.E., Hinz, N.H., Coolbaugh, M.F., and Siler, D., Favorable structural settings of active geothermal systems in the Great Basin region: Implications for fluid flow, normal fault mechanics, and geothermal and epithermal mineral exploration: Geological Society of America Annual Meeting, Vancouver, B.C., Canada, October 21, 2014.

Faulds, J.E., talk, Why is Nevada in Hot Water? Understanding and Harnessing Nevada's Vast Geothermal Resources: Project was described in a presentation to the general public at an open house for the Nevada Bureau of Mines and Geology at the Great Basin Science Sample and Records Library, October 15, 2014.

Field Trips

Hinz, N.H., Siler, D.L., and Delwiche, B., 2015, Great Basin geothermal geology: The 72MW McGinness Hills Power Plant, and the blind McGinness Hills geothermal resource: Geothermal Resources Council post-meeting field trip—The field trip visited the relatively new production geothermal fields at Salt Wells, NV (14.3 MWe capacity, producing since 2009) and McGinness Hills, NV (72 MWe net in 2015). The trip focused on the structural and geologic controls of geothermal circulation, from the crustal-scale to the geothermal field-scale in these fields and in geothermal fields throughout the Great Basin.

Licensing Agreements

- Earth-Vision 3D Software: A one-year license to use Earth-Vision 3D software was obtained Dynamic Graphics, Inc., in Alameda, California.
- Use of Seismic Reflection Profiles: License to use ~400 miles of seismic reflection profiles from Seismic Exchange, Inc., in Houston, Texas. The license restricts use of the profiles to interpretations. Images of the interpretations will be allowed for publication (per SEI review), but original digital and shot-point data cannot be submitted to the GDR at DOE or published.

REFERENCES

Allis, R., and 6 others, 2013, Characterizing the power potential of hot stratigraphic reservoirs in the western US: Proceedings. *38th Workshop on Geothermal Reservoir Engineering.* Stanford: Stanford University.

Allison, M., Chickering, C., Patten, K., Anderson, A., 2013, Sustaining the National Geothermal Data System: Considerations for a system-wide approach and node maintenance: GRC Transactions, v. 37, p. 531-538.

Ballentine, C. J., Burgess, R., and Marty, B., 2002, Tracing fluid origin, transport, and interaction in the crust *in* Porcelli, D., C. J. Ballentine, and R. Weller, eds., Noble gases in geochemistry and cosmochemistry: Reviews of Mineralogy and Geochemistry, Mineralogical Society America, v. 47, p. 539-614.

Barton, C.A., Hickman, S.H., Morin, R., Zoback, M.D., Benoit, D., 1998, Reservoir-scale fracture permeability in the Dixie Valley, Nevada, geothermal field: Proceedings, Soc. Pet. Eng. Annu. Meet., p. 315–322. doi:10.2523/47371-MS.

Barton, C.A., Zoback, M.D., Moos, D., 1995, Fluid flow along potentially active faults in crystalline rock: Geology v. 23, p. 23–27. doi:10.1130/0091-7613(1995)023<0683.

Bell, J.W., Caskey, S.J., Ramelli, A.R., and Guerrieri, L., 2004, Pattern and rates of faulting in the central Nevada seismic belt, and paleoseismic evidence for prior belt like behavior: Bulletin of the Seismological Society of America, v. 94, p. 1229-1254.

Bell, J.W., and Ramelli, A.R., 2007, Active faults and neotectonics at geothermal sites in the western Basin and Range: Preliminary results: GRC Transactions, v. 31, p. 375-378.

Bell, J.W., and Ramelli, A.R., 2009, Active fault controls at high-temperature geothermal sites: Prospecting for new faults: Geothermal Resources Council Transactions, v. 33, p. 425–429.

Bell, J., and Hinz, N., 2010, Young Walker basin faults provide new insights into structural relations controlling geothermal potential at the Hawthorne Army Weapons Depot, central Nevada: Geothermal Resources Council Transactions, v. 34, p. 751-754.

Benoit, W.R., Hiner, J.E., and Forest, R.T., 1982, Discovery and geology of the Desert Peak geothermal field: A case history: Nevada Bureau of Mines and Geology Bulletin 97, 82 p.

Blackwell, D.D., and D.S., Chapman, 1977, Interpretation of geothermal gradients and heat flow data for Basin and Range geothermal systems: Geothermal Resources Council Transactions, v. 1, p. 19-20.

Blackwell, D., and others, 1999, Structure of the Dixie Valley Geothermal System, a "Typical" Basin and Range Geothermal system, From Thermal and Gravity Data: GRC Transactions, v. 23, p. 525-531.

Blackwell, D., Stepp, P., and Richards, M., 2010, Comparison and discussion of the 6 km temperature maps of the western US prepared by the SMU Geothermal Lab and the USGS: GRC Transactions, v. 34, p. 515-519.

Blake, K., Davatzes, N.C., 2011, Crustal stress heterogeneity in the vicinity of Coso geothermal field, CA, in Proceedings, Thirty-Fifth Workshop on Geothermal Reservoir Engineering, Stanford University, p. 914–924.

Blake, K., Davatzes, N.C., 2012, Borehole image log and statistical analysis of FOH-3D, Fallon Naval Air Station, NV, in Proceedings, Thirty-Seventh Workshop on Geothermal Reservoir Engineering, Stanford University, p. 1054–1067.

Blewitt, G., M. Coolbaugh, W. Holt, C. Kreemer, J. Davis, and R. Bennett, 2003, Targeting of potential geothermal resources in the Great Basin from regional- to basin-scale relationships between geodetic strain and geological structures, GRC Transactions, v. 27, p. 3-7.

Blewitt, G., Hammond, W.C., and Kreemer, C., 2009, Geodetic constraints on contemporary deformation in the Northern Walker Lane: 1, Semi-permanent GPS strategy, *in* Oldow, J.S., and Cashman, P.H., eds., Late Cenozoic Structure and Evolution of the Great Basin – Sierra Nevada Transition: Geological Society of America Special Paper 447, p.1-16, doi: 10.1130/2009.2447(01).

Bonham-Carter, G.F., 1996, Geographic Information Systems for Geoscientists, Modelling with GIS: Elsevier Science Inc., Tarrytown, NY, 398 p.

Carranza, E.J.M., Wibowo, H., Barritt, S.D., and Sumintadireja, P., 2008, Spatial data analysis and integration for regional-scale geothermal potential mapping, West Java, Indonesia: Geothermics, v. 37, p. 267-299.

Caskey, S.J., Bell, J.W., Ramelli, A.R., and Wesnousky, S.G., 2004, Historic surface faulting and paleoseismicity in the area of the 1954 Rainbow Mountain-Stillwater earthquake sequence, central Nevada: Bulletin of the Seismological Society of America, v. 94, p. 1255-1275.

Chabora, et al., 2012. Hydraulic Stimulation of Well 27-15, Desert Peak Geothermal Field, Nevada, USA. 37th Stanford Geoth. Workshop, 12 p.

Cohen, J. K. and Stockwell, J. W., 2008, CWP/SU: Seismic Un*x Release No. 41: An open source software package for seismic research and processing: Center for Wave Phenomena, Colorado School of Mines.

Coolbaugh, M.F. and Bedell, R., 2006, A simplification of weights of evidence using a density function and fuzzy distributions; geothermal systems, *in* Harris, J.R., ed., GIS for the Earth Sciences: Geological Association of Canada Special Paper 44, p. 115-130.

Coolbaugh, M., and 14 others, 2005, Geothermal potential map of the Great Basin, western United States: Nevada Bureau of Mines and Geology Map 151.

Coolbaugh, M.F., Raines, G.L., and Zehner, R.E., 2007, Assessment of exploration bias in data-driven predictive models and the estimation of undiscovered resources: Natural Resources Research, v. 16, no. 2, p. 199-207.

Coolbaugh, M., Sladek, C., Zehner, R., and Kratt, C., 2014. Shallow temperature surveys for geothermal exploration in the Great Basin, USA, and estimation of shallow aquifer heat loss: Geothermal Resources Council Transactions, v. 38, p. 115-122.

Crafford, A.E.J., 2007, Geologic Map of Nevada: U.S. Geological Survey Data Series 249, 1 CD-ROM, 46 p., 1 plate.

Curewitz, D. and Karson, J.A., 1997, Structural settings of hydrothermal outflow: fracture permeability maintained by fault propagation and interaction: Journal of Volcanology and Geothermal Research, v. 79, p. 149-168

Davatzes, N.C., Hickman, S.H., 2006, Stress and faulting in the Coso geothermal field: Update and recent results from the East Flank and Coso Wash, in Proceedings, Thirty-First Workshop on Geothermal Reservoir Engineering, Stanford University, p. 24–35.

dePolo, C.M., and Anderson, J.G., 2000, Estimating the slip rates of normal faults in the Great Basin, USA: Basin Research, v. 12., p. 227-240.

Dering, G. and Faulds, J., 2012, Structural controls of the Tuscarora geothermal field, Elko County, Nevada: Geothermal Resources Council Transactions, v. 36, p. 41-46.

Dix, C. H., 1955, Seismic velocities from surface measurements: Geophysics, v. 20, p. 68–86.

Doust, H., 2010, The exploration play: what do we mean by it?: AAPG Bulletin, v. 94, n. 11, p. 1657-1672.

Faulds, J.E., Coolbaugh, M.F., Vice G.S., and Edwards, M.L., 2006, Characterizing structural controls of geothermal fields in the northwestern Great Basin: A progress report: Geothermal Resources Council Transactions, v. 30, p. 69-76.

Faulds, J.E., and 6 others, 2010, Structural controls of geothermal activity in the northern Hot Springs Mountains, western Nevada: The tale of three geothermal systems: Geothermal Resources Council Transactions, v. 34, p. 675-683.

Faulds, J.E., and others, 2011, Assessment of favorable structural settings of geothermal systems in the Great Basin, Western USA: Geothermal Resources Council Transactions, v. 35, p. 777-784.

Faulds, J.E., Hinz, N., Kreemer, C., Coolbaugh, M.F., 2012, Regional patterns of geothermal activity in the Great Basin region, western USA: Correlation with strain rates: Geothermal Resources Council Transactions, v. 36, p. 897–902.

Faulds, J.E., Hinz, N.H., Dering, G.M., Drew, D.L., 2013, The hybrid model – the most accommodating structural setting for geothermal power generation in the Great Basin, western USA: Geothermal Resources Council Transactions, v. 37, p. 3-10.

Faulds, J.E., and Hinz, N.H., 2014, Characterizing Structural Controls of EGS-Candidate and Conventional Geothermal Reservoirs in the Great Basin: Developing Successful Exploration Strategies in Extended Terranes: Final report submitted to the Department of Energy, 54 p.

Faulds, J.E., Hinz, N.H., Coolbaugh, M.F., and Siler, D.L., 2014, Favorable structural settings of active geothermal systems in the Great Basin region, western USA: Implications for fluid flow, normal faulting mechanics, and geothermal and epithermal mineral exploration: Geological Society of America Abstracts with Programs, v. 46, no. 6, p. 461.

Faulds, J.E., and Hinz, N.H., 2015, Favorable tectonic and structural settings of geothermal systems in the Great Basin region, western USA: Proxies for discovering blind geothermal systems: Proceedings World Geothermal Congress, Melbourne, Australia, 19-25 April 2015, 6 p.

Faulds, J.E., Hinz, N.H., Coolbaugh, M.F., Shevenell, L.A., Siler, D.L., dePolo, C.M., Hammond, W.C., Kreemer, C., Oppliger, G., Wannamaker, P.E., Queen, J.H., and Visser, C.F., 2015, Integrated geologic and geophysical approach for establishing geothermal play fairways and discovering blind geothermal systems in the Great Basin region, western USA: A progress report: Geothermal Resources Council Transactions, v. 39, p. 691-700.

Ferrill, D.A., Winterle, J., Wittmeyer, G., Sims, D., Colton, S., Armstrong, A., Horowitz, A.S., Meyers, W.B., and Simons, F.F., 1999, Stressed rock strains groundwater at Yucca Mountain, Nevada: GSA Today, v. 9, p. 2–9.

Fournier, R.O., Truesdell, A.H., 1973, An Empirical Na-K-Ca Geothermometer for Natural Waters: Geochimica et Cosmochimica Acta, v. 37: p. 1255-1275.

Fournier, R.O., and Potter, II, R.W., 1979, Magnesium correction to the Na-K-Ca chemical geothermometer. Geochim. Cosmochim. Acta, v. 43, p. 1543-1550.

Fournier, R.O., 1981, Application of water geochemistry to geothermal exploration and reservoir engineering, In Rybach, L. and Muffler, L.J.P., Geothermal systems: Principals and case histories: Wiley, Chichester, p. 109-143.

Giggenbach, W.F., 1988, Geothermal Solute Equilibria: Derivation of Na-K-Mg-Ca Geoindicators: Geochimica et Cosmochimica Acta. v. 52, p. 2749-2765.

Giggenbach, W.F., 1992, Chemical techniques in geothermal exploration: Chapter 5, in, Franco D'Amore, coordinator, Application of geochemistry in geothermal reservoir development: Series of Technical Guides on the use of Geothermal Energy, UNITAR/UNDP Centre on Small Energy Resources, Rome-Italy, 1991, p. 119-144.

Hammond, W.C., Kreemer, C., Blewitt, G., 2009, Geodetic constraints on contemporary deformation in the Northern Walker Lane: 3, Central Nevada seismic belt postseismic relaxation, *in* Oldow, J.S., and Cashman, P.H., eds., Late Cenozoic Structure and Evolution of the Great Basin – Sierra Nevada Transition: Geological Society of America Special Paper 447, p.33-54, doi: 10.1130/2009.2447(03).

Hastings, D. D., 1979, Results of exploratory drilling northern Fallon basin, western Nevada: RMAG-UGA – Basin and Range Symposium, p. 515-522.

Heidbach, O., Tingay, M., Barth, A., Reinecker, J., and Müller, B., 2008, The World Stress database release, 2008. doi:doi:10.1594/GFZ.WSM.Rel2008.

Hickman, S., Zoback, M.D., Benoit, W.R., 1998, Tectonic controls on reservoir permeability in the Dixie Valley, Nevada, geothermal field, in Proceedings, Twenty-Third Workshop on Geothermal Reservoir Engineering, Stanford University, p. 291–298.

Hickman, S.H., Davatzes, N.C., 2010, In-situ stress and fracture characterization for planning of an EGS stimulation in the Desert Peak Geothermal Field, Nevada, in Proceedings, Thirty-Fifth Workshop on Geothermal Reservoir Engineering, Stanford University, p. 13.

Hickman, S.H., Zoback, M.D., Barton, C.A., Benoit, W.R., Svitek, J., Summers, R., 2000, Stress and permeability heterogeneity within the Dixie Valley geothermal reservoir: Recent results from well 82-5, in Proceedings, Twenty-Fifth Workshop on Geothermal Reservoir Engineering, Stanford University, p. 256–265.

Hinz, N.H., Faulds, J.E., Oppliger, G.L., 2008, Structural controls of Lee-Allen Hot Springs, southern Churchill County, western Nevada: A small pull-apart in the dextral shear zone of the Walker Lane: Geothermal Resources Council Transactions, v. 32, p. 285-290.

Hinz, N.H., Faulds, J.E. and Stroup, C., 2011, Stratigraphic and structural framework of the Reese River geothermal area, Lander County, Nevada: A new conceptual structural model: GRC Transactions, v. 35, p. 827-832.

Hinz, N., Faulds, J., Siler, D., 2013, Developing systematic workflow from field work to quantitative 3D modeling for successful exploration of structurally controlled geothermal systems: GRC Transactions, v. 37, p. 275-280.

Hinz, N., Coolbaugh, M., and Faulds, J., 2014a, White Pine County renewable energy feasibility study and resources assessment: Geothermal Component: Nevada Bureau of Mines and Geology Open-File Report, in press.

Hinz, N.H., Faulds, J.E., Coolbaugh, M.F., 2014b, Association of fault terminations with fluid flow in the Salt Wells geothermal field, Nevada, USA: Geothermal Resources Council Transactions, v. 38, p. 3–10.

Huntington, K.W., and Lechler, A.R., 2015, Carbonate clumped isotope thermometry in continental tectonics: Tectonophysics, v. 647-648, p. 1-20.

Iovenitti, J., and 12 others, 2012, Towards developing a calibrated EGS exploration methodology using the Dixie Valley geothermal system, Nevada: Proceedings, 37th Workshop on Geothermal Reservoir Engineering, Stanford, CA, Jan. 30-Feb. 1, 2012, SGP-TR-194.

Ito, T., Zoback, M.D., 2000, Fracture permeability and in situ stress to 7 km depth in the KTB Scientific Drillhole: Geophysical Research Letters, v. 27, p. 1045–1048.

Jolie, E., Klinkmueller, M., and Moeck, I., 2015, Diffuse surface emanations as indicator of structural permeability in fault-controlled geothermal systems: Journal of Volcanology and Geothermal Research, v. 290, p. 97-113; http://dx.doi.org/10.1016/j.jvolgeores.2014.11.003.

Jolie, E., Faulds, J.E., and Moeck, I., 2012, The Development of a 3D structural-geological model as part of the geothermal exploration strategy - A case study from the Brady's geothermal system, Nevada, USA, *in* Proceedings, 37th Workshop on Geothermal Reservoir Engineering, Stanford University, p. 421–425.

Kele, S., and 12 others, 2015, Temperature dependence of oxygen- and clumped isotope fractionation in carbonates: A study of travertines and tufas in the 6-95oC temperature range: Geochimica et Cosmochimica Acta, in press, http://dx.doi.org/10.1016/j.gca.2015.06.032.

Kennedy, B.M., and van Soest, M.C., 2006, A helium isotope perspective on the Dixie Valley, Nevada, hydrothermal system: Geothermics, v. 35, p. 26-43.

Kennedy, B.M., and van Soest, M.C., 2007, Flow of mantle fluids through the ductile lower crust: Helium isotope trends: Science, v. 318, p. 1433-1436.

Kordy, M. A., Wannamaker, , Maris, V., Cherkaev, E., and Hill, G. J., 2015a, Three-dimensional magnetotelluric inversion using deformed hexahedral edge finite elements and direct solvers parallelized on SMP computers, Part I: forward problem and parameter jacobians: Geophysical Journal International, in press, 2015a.

Kordy, M. A., Wannamaker, P. E., Maris, V., Cherkaev, E., and Hill, G. J., 2015b, Three-dimensional magnetotelluric inversion using deformed hexahedral edge finite elements and direct solvers parallelized on SMP computers, Part II: direct data-space inverse solution: Geophysical Journal International, in press, 2015b.

Kreemer, C., Haines, J., Holt, W., Blewitt, G., and Lavallee, D., 2000, On the determination of a global strain rate model: Earth and Planetary Space Letters, v. 52, no. 10, p. 765–770.

Kreemer, C., Hammond, W.C., Blewitt, G., Holland, A.A., and Bennett, R.A., 2012, A geodetic strain rate model for the Pacific-North American plate boundary, western USA: NBMG Map 178, scale 1:1.500,000, 1 sheet.

Kreemer, C., G. Blewitt, and E. C. Klein, 2014, A geodetic plate motion and Global Strain Rate Model, Geochem. Geophys. Geosyst., v. 15, p. 3849–3889, doi:10.1002/2014GC005407.

Mariner, R.H., Presser, T.S., and Evans, W.C., 1983, Geochemistry of active geothermal systems in the northern Basin and Range Province: Geothermal Resources Council Special Report No. 13.

McLachlan, H., and Benoit, W.R., and Faulds, J.E., 2011, Structural framework of the Soda Lake geothermal area, Churchill County, Nevada: Geothermal Resources Council Transactions, v. 35, p. 925-930.

Moeck, I., Schandelmeier, Æ.H., and Holl, H., 2009, The stress regime in a Rotliegend reservoir of the northeast German basin: International Journal of Earth Sciences, v. 98, p. 1643–1654, doi: 10.1007/s00531-008-0316-1.

Moeck, I., Hinz, N., Faulds, J.E., Bell, J.W., Kell-hills, A., Louie, J., 2010, 3D geological mapping as a new method in geothermal exploration: A case study from central Nevada: Geothermal Resources Council Transactions, v. 34, p. 807–812.

Moos, D., and Ronne, J., 2010, Selecting the optimal logging suite for geothermal reservoir evaluation: Results from the Alum 25-29 Well, Nevada: Geothermal Resources Council Transactions, v. 34, p. 605–614.

Morris, A., Ferrill, D.A., and Henderson, D.B., 1996, Slip-tendency analysis and fault reactivation: Geology, v. 24, p. 275–278.

Nordquist, J., and Delwiche, B., 2013, The McGinness Hills geothermal project: Geothermal Resources Council Transactions, v. 37, p. 57-63.

Pili, E., Kennedy, B.M., Conrad, M.E., and Gratier, J.-P., 2011, Isotopic evidence for the infiltration of mantle and metamorphic CO_2-H_2O fluids from below in faulted rocks from the San Andreas fault system: Chemical Geology, v. 281, p. 242-252.

Poux, B. and Suemnicht, G., 2012, Use of GIS geoprocessing to select the most favorable sites for geothermal exploration in Oregon: GRC Transactions, v. 36, p. 745-750.

Prudic, D.E., Harrill, J.R., and Burbey, T.J., 1995, Conceptual evaluation of regional groundwater flow in the carbonate-rock province of the Great Basin, Nevada, Utah, and adjacent states: U.S. Geological Survey Professional Paper 1409-D, 102 p.

Richards, M., and Blackwell, D., 2002, A difficult search: Why Basin and Range systems are hard to find: Geothermal Resources Council Bulletin, v. 31, p. 143-146.

Robertson-Tait, A., Lutz, S.J., Sheridan, J., Morris, C.L., 2004, Selection of an interval for massive hydraulic stimulation in well DP 23-1 Desert Peak East EGS Project, Nevada, in Proceedings, Twenty-Ninth Workshop on Geothermal Reservoir Engineering, Stanford University, p. 216–221.

Robertson, E.C., 1988, Thermal properties of rocks: U.S. Geological Survey Open-File Report 88-441, 110 p.

Shevenell, L., and Coolbaugh, M., 2011, A new method of evaluation of chemical geothermometers for calculating reservoir temperatures from thermal springs in Nevada: GRC Transactions, v. 35, p. 657-661.

Shevenell, L., Penfield, R., Zehner, R., Johnson, G., and Coolbaugh, M., 2012, National Geothermal Data System Geochemical Data for Exploration: GRC Transactions, v. 36: 773-782.

Sibson, H., 1996, Structural permeability of fluid-driven fault-fracture: J. Structural Geology, v. 18, p. 1031–1042.

Siler, D.L., Mayhew, B., and Faulds, J.E., 2012, Three-dimensional geologic characterization of geothermal systems : Astor Pass, Nevada, USA: GRC Transactions, v. 36, p. 783–786.

Siler, D.L. and Faulds, J.E., 2013, Three-dimensional geothermal fairway mapping: examples from the western Great Basin, USA: GRC Transactions, v. 37, p. 327-332.

Siler, D. L., Kennedy, B. M., and Wannamaker, P. E., 2014, Regional lithospheric discontinuities as guides for geothermal exploration: Geothermal Resources Council Transactions, v. 38, p. 39-47.

Singer, D.A., 1993, Basic concepts in three-part quantitative assessments of undiscovered mineral resources: Nonrenewable Resources, v. 2, no. 2, p. 69–81.

Slemmons, D.B., Jines, A.E., and Gimlett, J.I., 1965, Catalog of Nevada earthquakes, 1852-1900: Bulletin of the Seismological Society of America, v. 55, p. 537-583.

Townsend, J., Zoback, M.D., 2000, How faulting keeps the crust strong: Geology, v. 28, p. 399–402. doi:10.1130/0091-7613(2000)28<399:HFKTCS>2.0.CO.

USGS, 2010, United States Geological Survey Quaternary Fault and Fold Database of the United States: http://earthquake.usgs.gov/hazards/qfaults/, retrieved 2013.

Wannamaker, P. E., and Doerner, W. M., 2002, Crustal structure of the Ruby Mountains and southern Carlin trend region, northeastern Nevada, from magnetotelluric data: Ore Geology Reviews, v. 21, p. 185-210.

Wannamaker, P.E., Doerner, W.M., and Hasterok, D.P., 2007, Integrated dense array and transect MT surveying at Dixie Valley geothermal area, Nevada; structural controls, hydrothermal alteration and deep fluid sources: Proceedings of 32nd Workshop on Geothermal Reservoir Engineering, Stanford, CA, SGP-TR-183, 6 p.

Wannamaker, P., Maris, V., Doerner, W., 2011, Crustal Scale Resistivity Structure, Magmatic-Hydrothermal Connections, and Thermal Regionalization of the Great Basin: GRC Transactions, v. 35, p. 1787-1790.

Wannamaker, P. E., V. Maris, J. Sainsbury, and J. Iovenitti, 2013, Intersecting fault trends and crustal-scale fluid pathways below the Dixie Valley geothermal area, Nevada, inferred from 3D magnetotelluric surveying, *Proc. 38th Workshop on Geothermal Reservoir Engineering*, Stanford, CA, SGP-TR-198, 9 p.

Williams, C., Reed, M., Galanis, S.P., and DeAngelo, J., 2007, The USGS National Geothermal Resource Assessment: An Update: GRC Transactions, v. 31, p. 99-104.

Williams, C.F., Reed, M.J., DeAngelo, J., and Galanis, S.P. Jr., 2009, Quantifying the undiscovered geothermal resources of the United States: GRC Transactions, v. 33, p. 995-1002.

Zoback, M.D., Townsend, J., 2001, Implications of hydrostatic pore pressures and high crustal strength for the deformation of intraplate lithosphere: Tectonophysics, v. 336, p. 19–30. doi:10.1016/S0040-1951(01)00091-9.